

**TNO report****2022 R11421 | 2.0****Detailed Engineering Assessment PSR &  
MSSR Florennes and Simple Engineering  
Assessment PSR Bertem, Saint-Hubert, Liège  
and Zaventem due to windfarm Chastrès-  
Walcourt****Defence, Safety & Security**Oude Waalsdorperweg 63  
2597 AK Den Haag  
P.O. Box 96864  
2509 JG The Hague  
The Netherlands[www.tno.nl](http://www.tno.nl)T +31 88 866 10 00  
F +31 70 328 09 61

Date	6 September 2022
Author(s)	Onno van Gent Stijn Dellevoet Saul Rindt
Copy no	
No. of copies	
Number of pages	102 (incl. appendices)
Number of appendices	
Sponsor	Windvision
Project name	DEA Florennes Chastres
Project number	060.51414/01.18.01

All rights reserved.

No part of this publication may be reproduced and/or published by print, photoprint, microfilm or any other means without the previous written consent of TNO.

In case this report was drafted on instructions, the rights and obligations of contracting parties are subject to either the General Terms and Conditions for commissions to TNO, or the relevant agreement concluded between the contracting parties. Submitting the report for inspection to parties who have a direct interest is permitted.

© 2022 TNO

# Contents

<b>1</b>	<b>Introduction</b> .....	<b>4</b>
<b>2</b>	<b>General information</b> .....	<b>5</b>
2.1	Introduction to PERSEUS.....	5
2.2	Pulse compression time sidelobes .....	7
2.3	Shadow effect .....	8
2.4	Typical CFAR processing .....	9
2.5	STAR 2000 Wind Farm Filter .....	10
2.6	Effects of Wind Turbines on Monopulse Secondary Surveillance Radar.....	11
<b>3</b>	<b>Specific Input Parameters</b> .....	<b>17</b>
3.1	Wind turbines.....	17
3.2	Radar Systems .....	23
<b>4</b>	<b>Detailed Engineering Assessment Primary Surveillance Radar Florennes</b> ....	<b>30</b>
4.1	PERSEUS results .....	30
4.2	Observations and remarks .....	46
4.3	STAR 2000 Wind Farm Filter .....	48
4.4	Parallel beam processing .....	52
4.5	Track continuity.....	53
4.6	Wind turbine plots, wind turbine tracks, track seduction .....	56
4.7	False target reports and processing overload .....	56
<b>5</b>	<b>Detailed Engineering Assessment of the MSSR at Florennes</b> .....	<b>57</b>
5.1	Digital Elevation Model .....	57
5.2	Radar Horizon Florennes .....	58
5.3	Line-of-sight to Individual Wind Turbines .....	61
5.4	Line-of-sight Coverage .....	63
5.5	Results of the OBE calculations .....	67
<b>6</b>	<b>Simple Engineering Analysis</b> .....	<b>72</b>
6.1	Line of Sight Analysis PSR Bertem .....	73
6.2	Line of Sight Analysis PSR Saint-Hubert.....	75
6.3	Line of Sight Analysis PSR Liège .....	77
6.4	Line of Sight Analysis PSR Zaventem.....	80
6.5	Eurocontrol Guidelines .....	81
6.6	Region 1: Shadow region .....	82
6.7	Region 2: Raised threshold regions .....	89
6.8	Remark .....	96
6.9	False target reports and processing overload .....	96
<b>7</b>	<b>Conclusions</b> .....	<b>98</b>
7.1	DEA primary surveillance radar Florennes.....	98
7.2	DEA Secondary surveillance radar Florennes .....	99
7.3	SEA primary surveillance radars Bertem, Saint Hubert, Liège and Zaventem .....	99
7.4	Changes to the wind turbine configuration .....	100
<b>8</b>	<b>List of abbreviations</b> .....	<b>101</b>

<b>9</b>	<b>References .....</b>	<b>102</b>
----------	-------------------------	------------

# 1 Introduction

The performance of radar systems can be negatively influenced by wind turbines in their vicinity. EUROCONTROL has issued guidelines, on how to assess the potential impact of wind turbines [1]. Within these guidelines different zones around the radar are defined. A Detailed Engineering Assessment (DEA) for the primary radar is required at distances of the wind turbines ranging from 500 m to 15 km (zone 1). In the zone ranging from 15 km to the instrumented range of the primary radar (zone 2), a so-called Simple Engineering Assessment is required. For the secondary radars, a DEA needs to be performed in case the wind turbines are located closer than 16 km from the radar.

In this study the impact of wind turbines on performance of the primary radar Airport Surveillance Radar (ASR) at Florennes Military Airbase is assessed, following the EUROCONTROL guidelines for Primary Surveillance Radars (PSRs). Windvision has plans to build four wind turbines at Chastrès-Walcourt. The closest wind turbine is located at a distance of approximately 14.5 km from the radar, so within 15 km from the radar. Therefore Skeyes requires a DEA to be performed for the PSR as well as for the MSSR. In addition to the PSR at Florennes there are four other PSRs at Bertem, Saint Hubert, Liège and Zaventem that are located outside the 15 km for the newly planned wind turbines. For these radars Skeyes and the Ministry of Defence requires a SEA.

Thales, the manufacturer of the STAR 2000 at Florennes, offers an enhanced processing feature, called the Wind Farm Filter (WFF), to mitigate the effects of wind turbines on the radar performance if required. The WFF enhancement has been built into the STAR 2000 at Florennes. In addition to the DEA, the improvements have been investigated for the STAR 2000 including this WFF enhancement.

In Section 2 the general information is given and in Section 3 the specific input parameters of the relevant wind turbines and radars for this study. In Section 4 we perform the detailed engineering assessment for the PSR at Florennes and in Section 5 for the MSSR at Florennes. In Section 6 we perform the simple engineering assessments for the PSR at Bertem, Saint Hubert, Liège and Zaventem. Finally in Section 7 conclusions are drawn.

## 2 General information

### 2.1 Introduction to PERSEUS

Details of the physical modelling in PERSEUS are described in [3] and [4], the most important aspects are repeated here:

- The resulting detection probability is obtained from a so-called Blake chart analysis, i.e., the signal-to-clutter-plus-noise ratio (SCNR) is determined first, and subsequently the single scan detection probability.
- The backscatter of a wind turbine is determined by modelling the tower as a series of slanted cylinders and the nacelle and wind turbine blades by ellipsoids. Furthermore, the blade flash probability is constant. Spectrally, wind turbine backscatter extends up to the blade tip speed with a distinct peak at zero Doppler frequency shift, due to the non-moving parts of the wind turbine (mast and nacelle). Results obtained with this approach have been compared with live measurements (most notably reports issued by the U.S. Air Force and by QinetiQ, [5] and [6] and are judged to be sufficiently representative.
- TNO uses the electromagnetic (EM) propagation module TERPEM to model the propagation, see [7]. The required terrain altitude data is derived from NASA's 1 arc-second SRTM database, corresponding to a range resolution of approximately 30 m.

#### 2.1.1 Areas of low detection probability

The target detection diagrams calculated by PERSEUS show large area of reduced detection probability. This can be explained by the combination of high landclutter return due to the presence of steep hills, and target speed and course averaging within PERSEUS.

The two aspects are explained on more detail in the following sections.

#### 2.1.2 Clutter return calculation

As already indicated, PERSEUS uses TERPEM to determine the propagation factor on transmit and on receive. TERPEM requires a characterization of the earth's surface, which determines its reflective properties. TERPEM offers several built-in terrain types: perfect conductor, wet ground, medium dry ground, very dry ground, sea water and freshwater. Besides, 'numerical' can be chosen in which case electrical features of the terrain (relative permittivity and conductivity) have to be specified explicitly.

PERSEUS considers backscatter from landclutter and backscatter from wind turbines. Landclutter reflections are calculated according to the constant  $\gamma$  model in which  $\gamma$  represents the ground reflectivity. The surface clutter peak power,  $P_{cs}$ , received in the radar from a patch defined by the intersection of the earth's surface of the azimuth beamwidth with a range gate at a range  $R_c$  is given by:

$$P_{cs} = \frac{P_{peak} G_T G_R \lambda^2 G_{proc} F^4 \sigma}{(4\pi)^3 R_c^4 L_{sys}}$$

where  $\sigma_{cs}$  represents the surface clutter cross section ( $m^2$ ),  $g(\theta)$  is the voltage gain of the antenna at the elevation angle of the clutter patch,  $R_c$  is the clutter range (m). The clutter cross section is calculated from the mean clutter reflectivity,  $\sigma^0$ , according to

$$\sigma_{cs} = \sigma^0 A_c$$

in which  $A_c$  represents the area of the clutter patch ( $m^2$ ), being the product of its width (i.e. in the cross range dimension) and its depth (in the range dimension), see Figure 2.1.

$$A_c = R_c \frac{\theta_{az}}{L_{bs}} \cdot \frac{c \tau_c}{2 \cos \psi}$$

$c$  is the velocity of light,  $\psi$  is the gazing angle, see Figure 2.2,  $\tau_c$  is the duration of the compressed pulse (if pulse compression is applied; otherwise the pulse duration is taken).

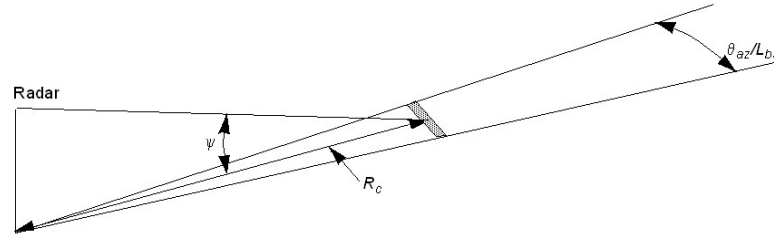


Figure 2.1 The shaded area denotes a clutter patch at ground range  $R_c$ .

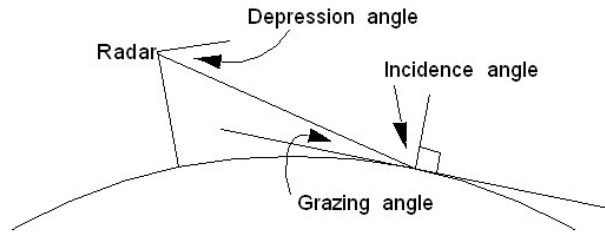


Figure 2.2 Notion of angles.

The SRTM terrain altitude database is used in the calculation of the grazing angle and the clutter range. The mean landclutter reflectivity is calculated according to the constant  $\gamma$  model:

$$\sigma^0 = \gamma \sin \psi$$

if  $R_c < R_{horizon}$ , otherwise

$$\sigma^0 = 0$$

A straightforward relationship between terrain type for TERPEM and  $\gamma$  is not easy to formulate as put forward by, for instance, Fred E. Nathanson [9], Section 7.9, and by Christopher C. Lin and J. Patrick Reilly [10]. Values for  $\gamma$  have been determined experimentally and equations that describe  $\gamma$  as a function of frequency have been proposed, such as:

$$\gamma = \gamma_r \left( \frac{f}{f_r} \right)^k$$

in which  $f_r$  and  $\gamma_r$  are a frequency and a  $\gamma$ -value that has been measured at the frequency, and  $k$  is 'a frequency scaling factor', see [9]. The TERPEM propagation that TNO uses derives the reflective properties of the terrain from the conductivity and the relative permittivity according to ITU-R P.527, [10]. For the simulation we

have applied 'medium dry ground'. Note that the at S-band, the precise terrain type does not significant influence the outcome of the simulations.

As already indicated, the clutter return within PERSEUS is calculated taking into account the grazing angle extracted from the terrain altitude database, the illuminated surface, or patch derived from the azimuth beam width and transmitted pulse width, and the surface reflectivity.

### 2.1.3 Target speed and course averaging

Within PERSEUS the detection probability is averaged for a target having different speeds, and different courses referenced to the radar position, including a tangential course during which no Doppler frequency shift is created. This provides a representative overall detection probability. However, due to the inclusion of axial moving targets within the averaging, the clutter rejection by the Doppler filters is less than what can be realised theoretically.

## 2.2 Pulse compression time sidelobes

In case a wind turbine response is received through a time-sidelobe of the compressed pulse, it can mask the radar's detection capability. The effect is illustrated in Figure 2.3 and occurs, for strong echoes, which can be the case for wind turbines. The effect will manifest itself over a depth of approximately 15 km.

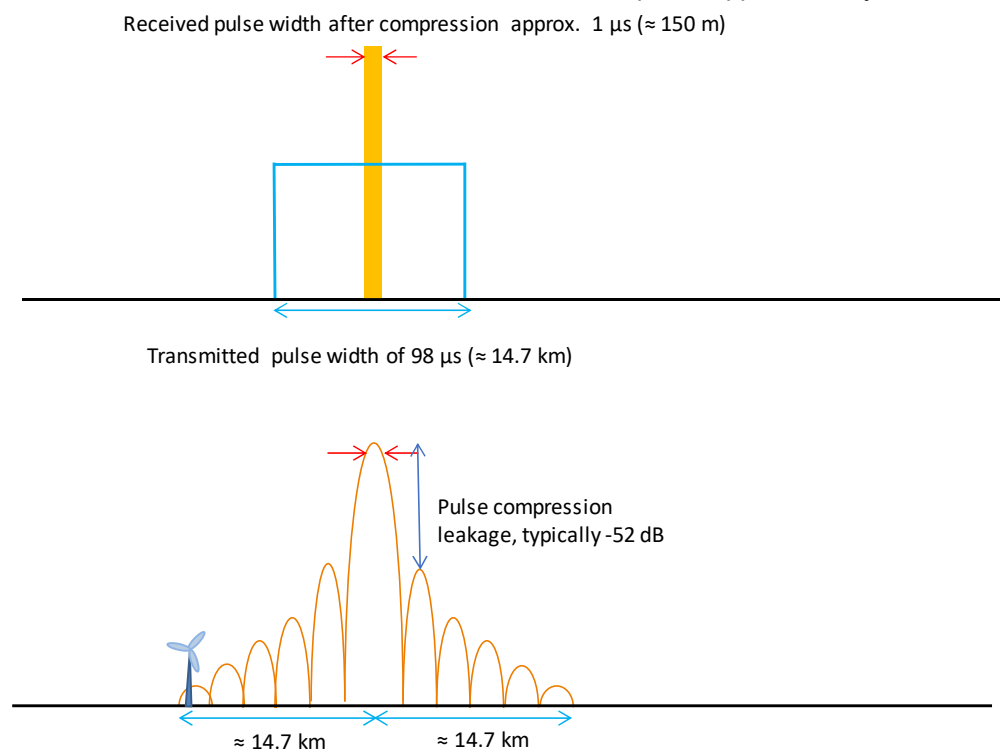


Figure 2.3 Pulse compression of the long pulse. The transmitted and received pulse measures  $98 \mu\text{s}$ . To increase range resolution the pulse is compressed to a narrow pulse of approximately  $1 \mu\text{s}$ . On top the ideal compressed pulse and below the actual compressed pulse with sidelobes. Leakage of the pulse compression is simulated at a level of  $-52 \text{ dB}$ , a typical value for such a radar.

The typical behaviour the detection probability behind the wind turbines due to time sidelobes is shown in Figure 2.4.

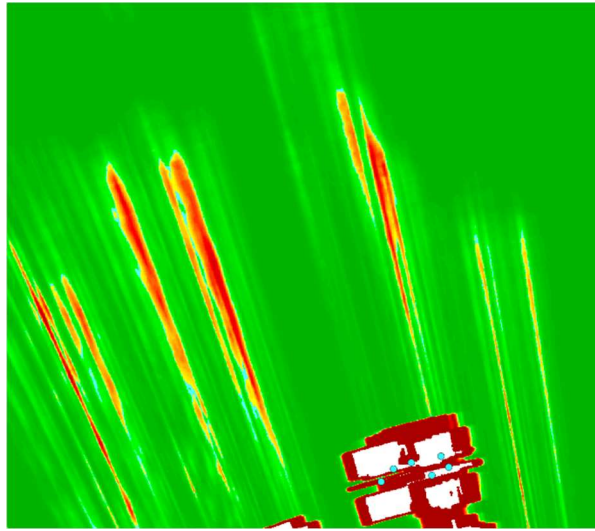


Figure 2.4 The typical behaviour of the detection probability behind the wind turbines due to time sidelobes

### 2.3 Shadow effect

In contradiction to an optical shadow, a wind turbine in the line of sight path will affect visibility, but not in all cases will cause the target to be invisible. This principle is illustrated in Figure 2.5. Radio waves diffract around an obstacle, limiting the shadow zone directly behind an obstacle. Due to the fact that energy is reflected back from the wind turbine the presence of a wind turbine will cause a loss in maximum detection range, see Figure 2.6.

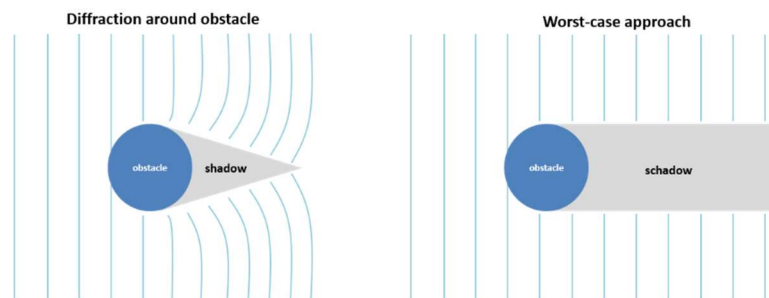


Figure 2.5 Graphical illustration of diffraction effects.

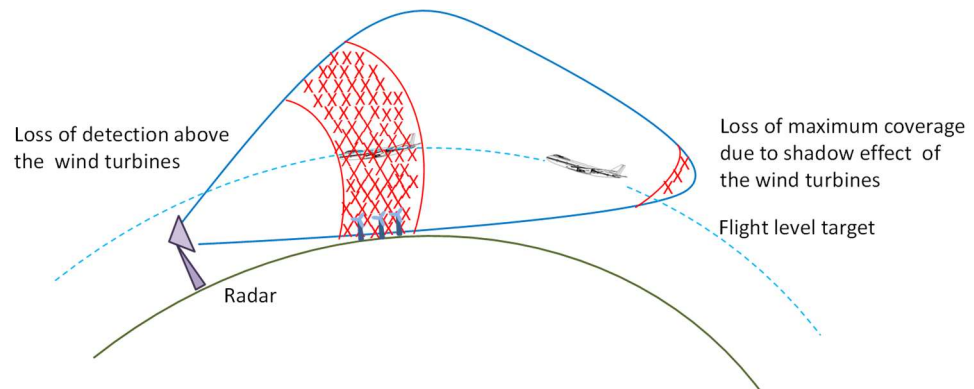


Figure 2.6 Loss of detection of the radar over the full elevation coverage of the antenna.

## 2.4 Typical CFAR processing

Target detection within the radar is performed at discrete steps in range, a so-called range cell or quant. The depth of a range cell is proportional to the transmitted pulse width after pulse compression, converted to meters. In the case of the STAR 2000 this is 1/16 (0.0625) NM (115.75 m). To avoid false detections, a separate threshold is calculated for each cell. This type of detection algorithm is known as constant false alarm rate detection (CFAR). The detection threshold for the cell under test (CUT) is determined by averaging the power levels over a number of range cells in front of the CUT (leading or early window) and a number of range cells behind the CUT (trailing or late window) and take the highest of the two. This technique is known as Cell Averaging Greatest Of or CAGO. These two windows are separated from the CUT by guard cells. The layout of a CFAR window is shown in Figure 2.7. The leading and trailing window of the STAR 2000 receiver consist both of eight range cells (926 m). On either side of the CUT there are two guard cells (231.5 m). Thus, the total width of the CFAR window including the CUT measures 21 cells or 2430.75 m in range, or approximately 1.3 NM. In the figure the target echo in the CUT is higher than the threshold and is therefore detected.

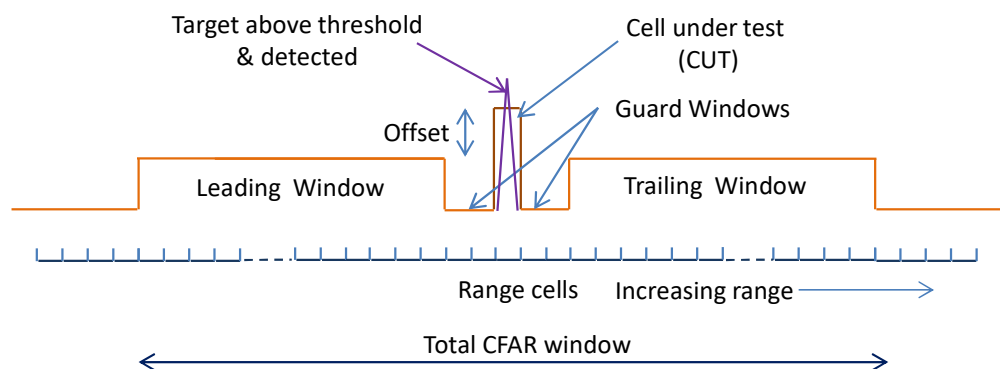


Figure 2.7 The layout of a CFAR window around the cell under test. It consists of a leading or early and a trailing or late window of 8 cells each and two guard windows of two cells each. The total width measures 21 range cells or 2430.75 m). The target echo in the CUT is higher than the threshold and is therefore detected.

The window with the largest average power determines the threshold of the CUT. If a wind turbine is present in the leading or trailing window, the radar returns from the

wind turbine blades will raise the average power level of the window, thus increasing the threshold. As a consequence, the detection capability of the radar is reduced. This effect is illustrated in Figure 2.8.

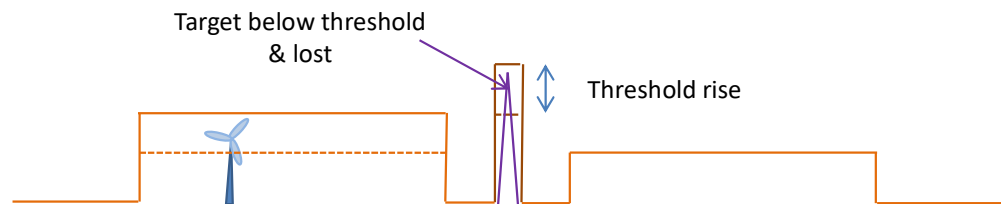


Figure 2.8: The effect of a wind turbine within the leading or trailing window. The blade flashes of the wind turbine will cause the average power level in the window to rise, thus increasing the threshold and decreasing the sensitivity of the radar. The target echo now stays below threshold and is not detected and becomes lost.

Therefore a wind turbine can potentially reduce the detection capability of a radar over an area in range from  $-\frac{1}{2}$  to  $+\frac{1}{2}$  the CFAR depth. In azimuth the affected sector is roughly the antenna azimuth 3 dB beam width. These effects are known under the term 'Desensitisation Overhead.'

In case of the STAR 2000, the detection probability is influenced from approximately 1.2 km in front to 1.2 km behind the wind turbine position and over the 3 dB azimuth beamwidth: an azimuth sector of approximately  $1.4^\circ$ . In case of large reflections the effects may extend even beyond the 3 dB azimuth beamwidth. The typical behaviour of the detection probability in the presence of two wind turbines is shown in Figure 2.9.

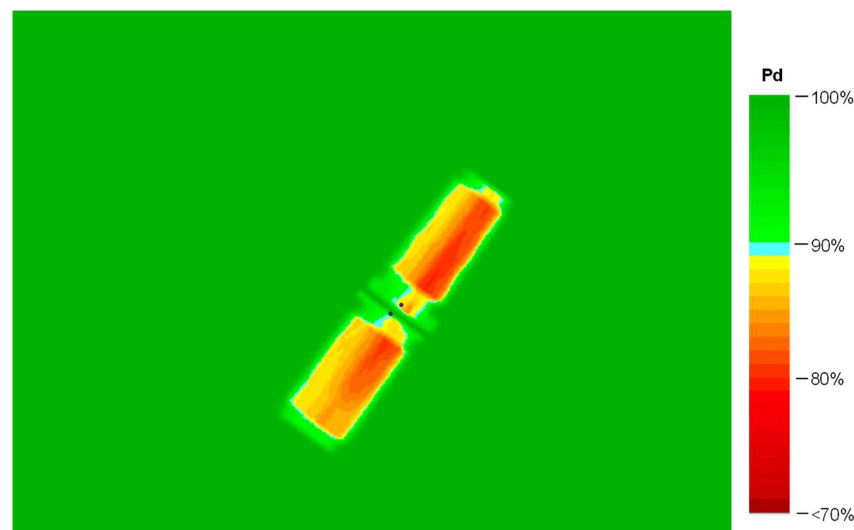


Figure 2.9 The typical behaviour of the detection probability in the presence of in this case two wind turbines, shown as two dots. The radar illuminated the wind turbines from the top right corner. The detection capability is reduced if one of the turbines is within the leading or trailing CFAR window.

## 2.5 STAR 2000 Wind Farm Filter

Thales, the manufacturer of the STAR 2000, offers an enhanced processing feature, called the Wind Farm Filter (WFF), to mitigate the effects of wind turbines on the radar performance if required. One remedy is that special CFAR processing

is applied around the wind turbine positions, which demands that the radar 'knows' where wind turbines are. The radar model within PERSEUS of the STAR 2000 has been based on detailed information, such as system parameters from a Blake chart, antenna diagrams and CFAR operation, provided by Thales France under the NDA [2]. For the WFF enhanced processing, Thales appeared to be reluctant to provide detailed information. The assessment therefore has been based on verbal information and should therefore be considered as the best simulation we can provide with limited given assumptions. TNO however was able to compare the results from the PERSEUS simulations with the results from Thales simulations for a known off-shore wind farm and it was found that the TNO and the Thales results match. Due to proprietary reasons laid down by Thales, TNO is not able to elaborate on the details of the processing. The results in case WFF processing would be applied on the wind turbines around the radar, however, are not restricted.

## 2.6 Effects of Wind Turbines on Monopulse Secondary Surveillance Radar

The presence of wind turbines can influence the performance of MSSRs. In order to correctly interpret the results of the line-of-sight analysis, we address the most important issue that can arise whenever a wind farm is near a secondary radar system: bearing errors.

SSRs differ from PSRs in a number of ways. PSRs do not depend on cooperation of aircraft, they merely measure range, bearing and sometimes also elevation angle and radial velocity. SSRs demand that aircraft cooperate, *i.e.*, the aircraft actively participates in its detection. The SSR sends out an interrogation signal at 1030 MHz. The target, carrying a radar transponder, subsequently replies by transmitting a response signal at 1090 MHz. This response contains additional information regarding the target, *e.g.*, barometric altitude (mode C) and an identity code (mode A). In the case of monopulse SSR (MSSR), the system is capable of making a precise bearing estimate of the target from a single reply signal (hence, monopulse). The bearing estimate is generally accurate within a fraction of a degree ( $\sim 0.05^\circ$ ). The presence however of an obstacle (like a mountain, building or wind turbine) between the MSSR antenna and the target can cause an error in the estimation of the bearing to the target.

In Figure 2.10 an MSSR antenna is shown, typically comprising 35 antenna elements. Below we first give a short description on how the bearing measurement is carried out and how the wind turbine influences this measurement.



Figure 2.10 The secondary radar antenna, comprising of 35 antenna elements, on top of a STAR 2000 antenna.

The bearing to a target is determined using the so-called monopulse technique. By applying different weight factors for each antenna element, two radar beams are created with the same antenna, the so-called *sum beam* and *difference beam*, see Figure 2.11. A reply is received by both beams. By comparing the signal strength in the sum beam to the signal strength in the difference beam an accurate bearing angle can be estimated. Left-right ambiguity is solved by looking at the phase of the signal. For example, when the sum and difference beam record a pulse with the same signal strength, looking at Figure 2.11 we see that the bearing to the target must be, depending on the phase, either  $+1^\circ$  or  $-1^\circ$ .

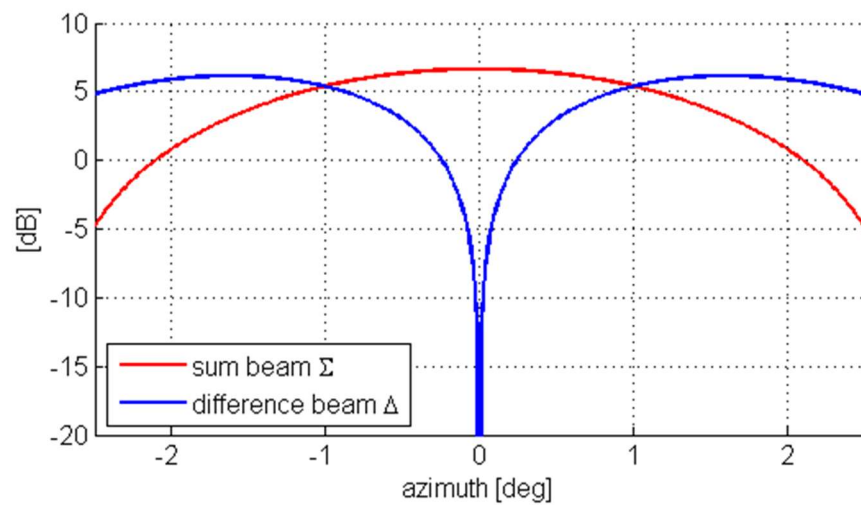


Figure 2.11 The sum beam (red) and difference beam (blue) used within the TNO model. The bearing of the target is estimated by comparing the signal strength of a single reply signal in both beams.

If a wind turbine is positioned between the target and the radar, the electric field is distorted both in phase and amplitude. This is illustrated in Figure 2.12. The distorted field effectively changes the weight factor at each antenna element, thus, changing the shape of the sum beam and difference beam. As the two beams are influenced differently by the wind turbine, so is the signal strength measured in both beams. Therefore, when the signal strength is compared to estimate the bearing, an error is introduced.

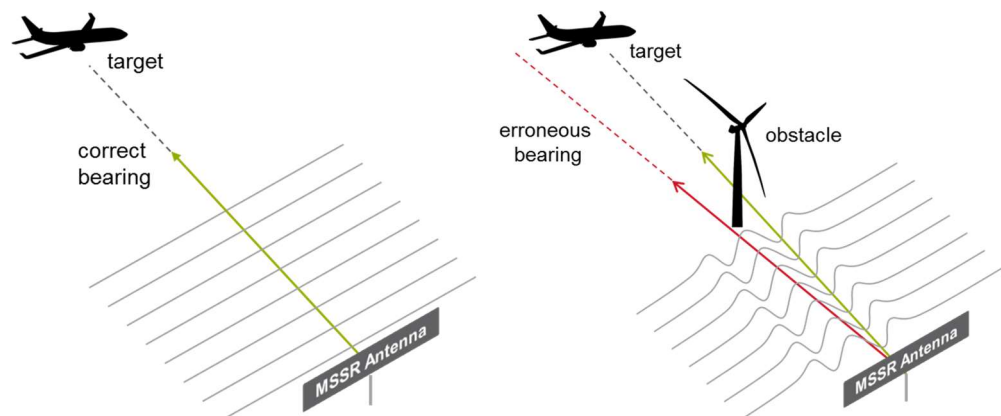


Figure 2.12 A wind turbines, positioned between target and MSSR antenna can disturb the transponder signal, introducing an error in the bearing estimate.

The bearing error as a function of azimuth has been calculated. This will give us insight in the width of the zone in which the MSSR is influenced by the wind turbine. To estimate the bearing error we use an analytical solution for an incident plane wave on a cylinder with fixed radius and infinite length. The method calculates the phase and amplitude of the perturbed wave front on each antenna element. From this the bearing error is determined. The method is described in full in [11]. In this reference the method has been validated using real data of an MSSR partially obstructed by a metal mast of width  $\sim 2$  m at a range of approximately 600 m.

TNO has conducted its own validation of the method as well using real MSSR data. In this validation the MSSR is partly obstructed by an ATC tower with a maximum width of 20 m at a range of approximately 2 km. In both cases, the calculated bearing error as a function of azimuth matched relatively well with the measured data. Figure 2.13 shows the close match between real recorded MSSR track of an aircraft at a distance around 175 km from the MSSR and the simulated data. Secondary effects at coordinates [4, 178] and [-4, 174] km appear accurately modelled as well (indicated by red arrows).

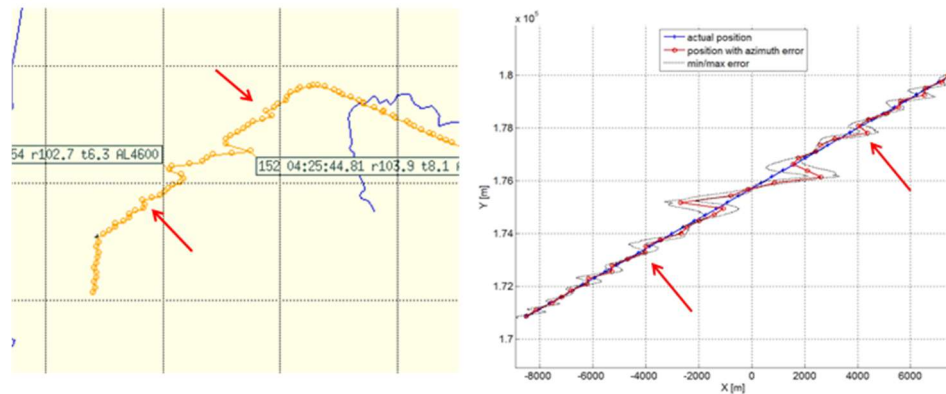


Figure 2.13: Comparison of a MSSR track recording of a real aircraft and the simulated results. Secondary effects at coordinates [4, 178] and [-4, 174] km appear accurately modelled as well (indicated by red arrows).

As mentioned, the method uses a cylinder of infinite length to model the obstacle. An infinite cylinder can be described by just a single parameter, the width. In our simulations we have chosen the width of the cylinder to be dependent on whether or not the nacelle or blades can be seen by the radar. (1) In the orange areas, the width of the cylinder is equal to the average of the width and length of the nacelle. (2) In the red areas, the width of the cylinder for all visible wind turbines is set to the width of the blade. See Figure 2.14.

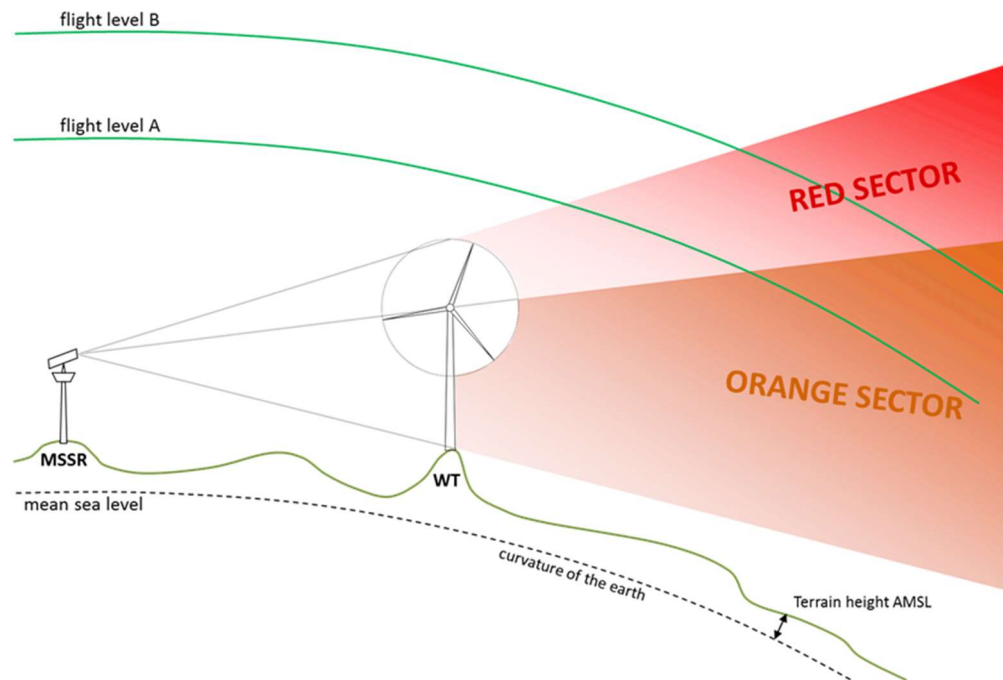


Figure 2.14 The orange and red areas, shown in the LoS coverage diagrams are in fact cuts through a volume behind the wind turbines. The calculated OBE is thus valid at all flight levels shown in the LoS coverage diagrams.

It is assumed that there is always a wind turbine blade with a vertical orientation. The full tip height of the turbine is used in the analysis. As there is not always a wind blade directed vertically, this is a worst case assumption.

Furthermore, the applied method describes the incoming signal as a plane wave (as depicted in the left image of Figure 2.12). The approximation of the incoming radiation as a plane wave is valid in case the distance between the target and the obstacle is sufficiently large. To see if the plane wave approximation is valid, we calculate at which distance the phase difference between the two ends of the wind turbine blade is equal to half a wavelength. The path difference  $\Delta r$  from one end of the blade to the other can be approximated by  $\Delta r = L^2/2R$ , where  $L$  is the length of the blade and  $R$  is the range. Setting  $\Delta r$  equal to half a wavelength,  $\lambda/2$ , and filling in  $L=60.7$  m, we find  $R = 13$  km at 1090 MHz. We see that the incoming wave for a target at 13 km behind the obstacle already resembles a plane wave quite closely. For targets at larger distance the resemblance will be even better. For targets closer than 13 km to behind the wind turbine, the estimated bearing error is a first order approximation.

Regarding the geometry of the situation, we take into account two parameters: (1) the azimuth angle to the target, relative to the obstacle and (2) the orientation of the radar antenna at the moment the reply is received. Given a wind turbine at a certain azimuth,  $\alpha$ , we let the target move from  $\alpha - 4^\circ$  to  $\alpha + 4^\circ$  in 501 steps. At more than  $4^\circ$  azimuth from the wind turbine the error reduces rapidly to values much smaller than the accuracy of the MSSR (typically  $0.05^\circ$ ). For each position of the target, the radar antenna is rotated over  $3^\circ$ , from  $-1.5^\circ$  to  $1.5^\circ$ , where  $0^\circ$  corresponds to the antenna looking directly at the target. For each geometry the disturbed electric field

is calculated. This is done for each (visible) wind turbine in the wind farm separately. Subsequently, all disturbed fields are summed and the bearing error for the total field is calculated.

A typical example of the off-boresight error for a single obstacle (cylinder width 25 m) at a range of 3 km is shown in Figure 2.15. The obstacle is located at an azimuth angle of  $218.5^\circ$ . The red, orange and grey lines represent the 50<sup>th</sup>, 90<sup>th</sup> and 100<sup>th</sup> percentiles, respectively. This means that at a given azimuth angle, the error is in 100% of the cases contained within the two grey lines, in 90% of the cases between the two orange lines. The error at a given azimuth angle is thus not a single number, but lies in the range defined by the two grey lines. The reason this happens, is that, as mentioned above, the geometry between the rotating antenna, target and obstacle can differ for a target at a given azimuth. The grey line thus gives the upper limit of the bearing error to be expected at a given azimuth angle. This is the case when the radar antenna is in the least favourable orientation when receiving the reply signal.

As can be seen in the figure below the off-boresight error caused by a single obstacle is point symmetrical around the azimuth to the obstacle. Directly behind the obstacle, the error is zero. In this case the sum and difference beams are equally disturbed, resulting in no error. Note that in the case of multiple obstacles at different ranges, the symmetry is broken.

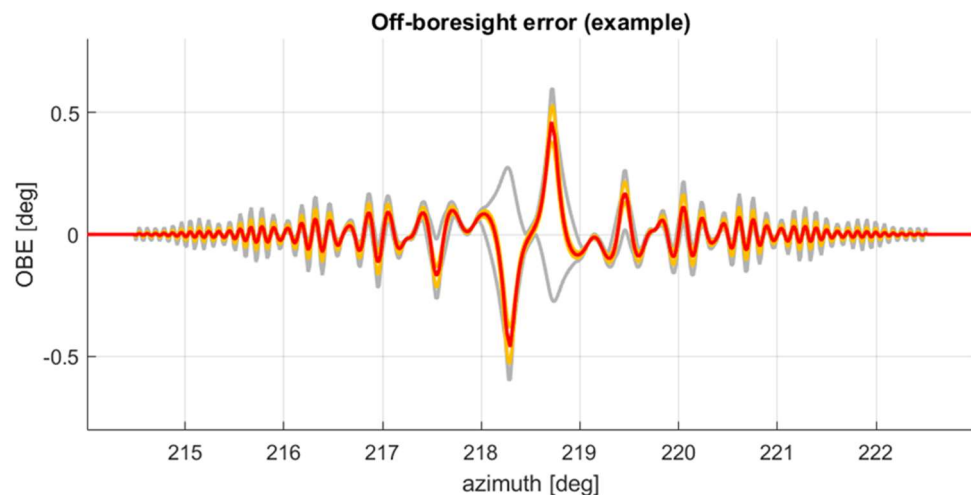


Figure 2.15 The off-boresight error for an infinite cylinder with a width of 25 m at a range of 3 km from the radar antenna. The error is point symmetrical around the azimuth angle to the obstacle.

## 3 Specific Input Parameters

### 3.1 Wind turbines

A detailed engineering assessment is carried out for the newly planned wind turbines of windfarm near Chastrès-Walcourt comprising four wind turbines. All existing or already authorised wind turbines within a 20 km radius from the planned wind turbines are also taken into account. An overview of the situation is provided in Figure 2.1. The yellow dots indicate the four wind turbines under investigation and the cyan dots are the existing and authorised wind turbines within the 20 km red circle around the newly planned windfarm. The distance between the radar at Florennes and the closest wind turbines WT4 of the newly planned windfarm measures approximately 14.5 km.

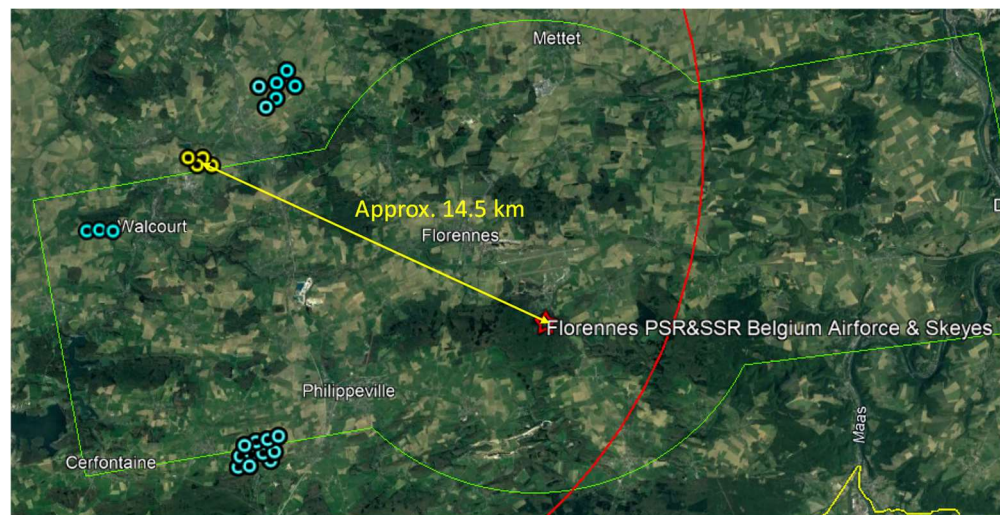


Figure 3.1 The locations of the newly planned windfarm Chastrès-Walcourt (yellow dots). The cyan dots correspond to the existing and authorised wind turbines within a radius of 20 km (red circle) around the newly planned wind turbines that are considered in this study. The primary radar at Florennes Airbase is indicated by the red star. The green zone corresponds to the Controlled Traffic Region (CTR) of Florennes Airbase. Image taken from Google Earth.

In addition to the radar at Florennes, there are four other radar involved as well, the radar at Bertem and the military airbase Saint-Hubert and the airports at Liège and Zaventem, see Figure 3.2. The distance to the windfarm measures approximately 67 km for Bertem, 75 km for Saint-Hubert, 79 km for Liège and 68 km for Zaventem.



Figure 3.2 The distance between the PSR at Bertem, Saint-Hubert, Liège and Zaventem and the newly planned windfarm measures approximately 67, 75, 79 and 68 km, respectively. Image taken from Google Earth.

In Table 3.1 an overview is presented of the positions, types, hub and tip heights of the existing and authorised wind turbines within a distance of 20 km from the newly planned wind turbines. The positions, type of the wind turbines and tip height have been received from Windvision. The selected wind turbine type has been based on the defined rotor diameter, tip height and output power. The height of the ground level at the locations is given with respect to the EGM96 geoid and has been derived from the 1 arcsecond SRTM terrain height database.

Table 3.1 Overview of the positions, type and tip heights of the existing wind turbines within a 20 km distance from the newly planned wind turbines which have been provided by Windvision. The longitude, latitude have been derived from the Lambert72 coordinates and terrain heights are provided by Windvision. The longitude, latitude have been derived from these.

Nr.	Location	Lam72 X [m]	Lam72 Y [m]	Lat [°]	Long [°]	Terrain [m]	Type	Hub [m]	Tip [m]
1	Walcourt	160049	110940	50.30937	4.50982	229	MD77	85	123.5
2	Walcourt	158955	110308	50.30371	4.49444	239	MD77	85	123.5
3	Walcourt	159652	110455	50.30502	4.50423	241	MD77	85	123.5
4	Walcourt	159234	109503	50.29647	4.49834	231	MD77	85	123.5
5	Walcourt	159629	109850	50.29958	4.50389	237	MD77	85	123.5
6	Walcourt	160379	110335	50.30393	4.51443	238	MD77	85	123.5
7	Fosses-la-ville Mettet	170779	118567	50.37766	4.66088	242	E82	98	139
8	Fosses-la-ville Mettet	171282	118706	50.37889	4.66796	238	E82	98	139
9	Fosses-la-ville Mettet	168536	117843	50.37123	4.62931	232	E82	98	139
10	Fosses-la-ville Mettet	168857	117602	50.36905	4.63381	235	E82	98	139

Nr.	Location	Lam72 X [m]	Lam72 Y [m]	Lat [°]	Long [°]	Terrain [m]	Type	Hub [m]	Tip [m]
11	Fosses-la-ville Mettet	169523	118202	50.37442	4.64320	234	E82	98	139
12	Fosses-la-ville Mettet	170145	118431	50.37646	4.65196	241	E82	98	139
13	Fosses-la-ville Mettet	170920	118223	50.37456	4.66284	248	E82	98	139
14	Fosses-la-ville Mettet	170454	118018	50.37274	4.65628	248	E82	98	139
15	Fosses-la-ville Mettet	169203	117372	50.36697	4.63866	240	E82	98	139
16	Fosses-la-ville Mettet	169629	117173	50.36517	4.64464	247	E82	98	139
17	Fosses-la-ville Mettet	170143	117307	50.36635	4.65187	253	E82	98	139
18	Fosses-la-ville Mettet	170795	117655	50.36946	4.66105	256	E82	98	139
19	Fosses-la-ville Mettet	170120	116856	50.36230	4.65152	259	E82	98	139
20	Fosses-la-ville Mettet	170797	117206	50.36542	4.66105	263	E82	98	139
21	Fosses-la-ville Mettet	170561	116740	50.36124	4.65771	263	E82	98	139
22	Cerfontaine	159751	96609	50.18053	4.50526	265	V90	78	123
23	Cerfontaine	159323	96473	50.17932	4.49926	258	V90	78	123
24	Cerfontaine	158873	96387	50.17855	4.49296	253	V90	78	123
25	Cerfontaine	158421	96243	50.17726	4.48663	247	V90	78	123
26	Cerfontaine	159594	95995	50.17502	4.50305	264	V90	78	123
27	Cerfontaine	159141	95939	50.17452	4.49670	265	V90	78	123
28	Cerfontaine	158696	95877	50.17397	4.49047	262	V90	78	123
29	Cerfontaine	158249	95814	50.17341	4.48421	261	V90	78	123
30	Cerfontaine	159449	95646	50.17188	4.50101	263	V90	78	123
31	Cerfontaine	158616	95435	50.17000	4.48934	262	V90	78	123
32	Cerfontaine	158169	95384	50.16955	4.48308	264	V90	78	123
33	Beaumont (Froidchapelle)	145493	100738	50.21772	4.30559	235	GE 2.5 100	100	150
34	Beaumont (Froidchapelle)	145587	100205	50.21293	4.30691	247	GE 2.5 100	100	150
35	Beaumont (Froidchapelle)	145606	99830	50.20956	4.30718	256	GE 2.5 100	100	150
36	Beaumont (Froidchapelle)	145828	99475	50.20637	4.31029	256	GE 2.5 100	100	150
37	Beaumont (Froidchapelle)	146275	99935	50.21051	4.31655	250	GE 2.5 100	100	150
38	Beaumont (Froidchapelle)	146817	99123	50.20321	4.32415	252	GE 2.5 100	100	150
39	Beaumont (Froidchapelle)	146598	101490	50.22449	4.32106	227	GE 2.5 100	100	150
40	Beaumont (Froidchapelle)	147252	101341	50.22315	4.33023	229	GE 2.5 100	100	150

Nr.	Location	Lam72 X [m]	Lam72 Y [m]	Lat [°]	Long [°]	Terrain [m]	Type	Hub [m]	Tip [m]
41	Beaumont (Froidchapelle)	147850	101278	50.22259	4.33861	236	GE 2.5 100	100	150
42	Beaumont (Froidchapelle)	146767	101004	50.22012	4.32343	233	GE 2.5 100	100	150
43	Beaumont (Froidchapelle)	147198	100842	50.21867	4.32948	243	GE 2.5 100	100	150
44	Beaumont (Froidchapelle)	146552	100605	50.21653	4.32043	240	GE 2.5 100	100	150
45	Beaumont (Froidchapelle)	147262	100356	50.21430	4.33038	244	GE 2.5 100	100	150
46	Beaumont (Froidchapelle)	147781	100053	50.21158	4.33765	254	GE 2.5 100	100	150
47	Beaumont (Froidchapelle)	147231	99874	50.20996	4.32994	248	GE 2.5 100	100	150
48	Beaumont (Froidchapelle)	146534	99573	50.20726	4.32018	256	GE 2.5 100	100	150
49	Beaumont (Froidchapelle)	146236	99252	50.20437	4.31601	256	GE 2.5 100	100	150
50	Fontenelle	152697	104680	50.253172	4.40656	233	V136*	112	180
51	Fontenelle	152203	104637	50.252788	4.39963	226	V136*	112	180
52	Fontenelle	153232	104633	50.252747	4.41406	220	V136*	112	180

\* This windfarm has been granted for a 5 MW maximum wind turbine with a maximum rotor diameter of 140 m and a maximum tip height of 180 m. Final selection of a wind turbine has not yet been made. Therefore a V136 with a output power of 4.5 MW, a hub height of 112 m and a rotor diameter of 136 m has been taken as a representative type.

The position and dimensions of the four newly planned wind turbines are presented in Figure 3.3 and Table 3.2. The coordinates of the wind turbines are given in Lambert72 coordinates and have been received from Windvision. The WGS84 coordinates have been derived from the Lambert72 coordinates. The height of the ground level at the locations is given with respect to the EGM96 geoid and has been derived from the SRTM1 terrain height database.



Figure 3.3 The four wind turbines under investigation at Chastrès-Walcourt. The green line corresponds to the northern border of the CTR of Florennes Airbase [Google Earth].

Table 3.2 Overview of the positions of the newly planned wind turbines. The X, Y coordinates have been provided by Windvision. The longitude and latitude have been derived from the Lambert72 coordinates. The terrain height has been derived from the SRTM altitude database. The tip height of the planned turbines are provided by Windvision.

Nr.	ID	Lambert72 Coordinates		Terrain height	Lat. WGS84	Lon. WGS84	Tip Height AGL
		X [m]	Y [m]	Z [m]	[°]	[°]	[m]
53	New WT1	156179	107514	203	50.27863	4.45543	180
54	New WT2	156754	107520	210	50.27867	4.46350	180
55	New WT3	156535	107226	204	50.27603	4.46042	180
56	New WT4	157116	107215	205	50.27593	4.46857	180

No final selection of the wind turbine type have been performed yet. There are three potential candidates to select from. The N131 Delta from Nordex, the V126 from Vestas both with a tip height of 180 m, and the GE-3.8-130 from General Electric with a tip height of 175 m. The main dimensions of these three candidates are listed in Table 3.3.

Table 3.3 Three potential wind turbine candidates and the derived worst-case and their dimensions

Manufacturer	Model	Output Power [MW]	Hub height [m]	Rotor diameter [m]	Tip height [m]
Nordex	N131 Delta	3.6	114	131	180
Vestas	V126	3.45	117	126	180
GE	GE-3.8-130 LNTEs	3.8	110	130	175

This worst-case approach with a maximum hub height of 117 m and maximum rotor diameter of 131 m results in a theoretical tip height of 182.5 m AGL. However when the final selection is performed, the final tip height will never exceed 180 m AGL, according to Windvision. This worst-case approach also covers other representative wind turbines within the same power range and maximum tip height.

For the detailed engineering assessment of the primary radar the dimensions of the mast, nacelle and turbine blades need to be known. The dimensions used within the PERSEUS simulations of the newly planned turbines have been derived from 3D CAD drawings of the turbines that are available in the TNO wind turbine dimension database. The length of the nacelle is defined as the distance from the 'hub' to the back of the nacelle. The width of the nacelle has been derived from the effective surface area of the front of the nacelle and could deviate slightly from the actual dimensions. The widths of the blades have been derived from the frontal area of the blade. The worst case dimensions of the wind turbine used within the simulations, listed in Table 3.4, have been derived by taking the maximum or worst-case values from the actual dimensions of the four candidates.

Table 3.4 The worst case dimension of the wind turbine used within the simulations, derived from the actual dimensions of the Nordex N131 Delta, the Vestas V126 and the General Electric GE-3.8-130.

Wind Turbine Type	Mast length [m]	Mast $\varnothing$ top [m]	Mast $\varnothing$ base [m]	Nacelle Height [m]	Nacelle Width [m]	Nacelle Length [m]	Blade Length [m]	Blade Width [m]
N131 Delta	111.6	3.3	4.3	4.9	6.8	16.3	65.5	3.0
V126	114.3	3.3	4.1	4.8	4.8	17.5	63.1	2.9
GE-3.8-130	108.0	3.1	4.3	4.3	4.1	12.3	64.3	3.4
WC@182.5	114.3	3.3	4.3	4.9	6.8	17.5	65.5	3.4

The dimensions of the newly planned, existing and authorised wind turbines are presented in Table 3.5.

Table 3.5 The dimensions of the new wind turbines used in the calculations of the newly planned windfarm and the existing and authorised wind turbines in the 20 km neighbourhood.

Wind Turbine Type	Manufacturer	Mast length [m]	Mast $\varnothing$ top [m]	Mast $\varnothing$ base [m]	Nacelle Height [m]	Nacelle Width [m]	Nacelle Length [m]	Blade Length [m]	Blade Width [m]
WC@182.5	TNO	114.3	3.3	4.3	4.9	6.8	17.5	65.5	3.4
E92@150	Enercon	105.2	2.3	6.8	4.9	5.2	11.7	46.2	2.4
LTW80@105	Leitwind	62.7	1.9	3.8	4.1	4.6	7.4	40.2	1.7
MM92@122	Senvion	73.7	2.5	4.0	4.3	4.2	12.9	46.1	2.7
N117Gamma@150	Nordex	88.9	3.0	4.3	4.0	4.1	13.6	58.4	2.6
N117Delta@150	Nordex	89.8	3.3	4.0	4.9	4.6	16.0	58.4	2.6
SG-2.6-114@141	Siemens-Gamesa	82.0	3.0	4.1	4.0	4.1	13.6	57.0	3.0
SG-2.6-114@142	Siemens-Gamesa	83.0	3.0	4.1	4.0	4.1	13.6	57.0	3.0
SG-2.6-114@150	Siemens-Gamesa	91.0	3.0	4.1	4.0	4.1	13.6	57.0	3.0
V110@150	Vestas	92.8	2.3	3.7	4.0	4.3	14.6	55.0	2.6
V110@180	Vestas	122.8	2.3	3.7	4.0	4.3	14.6	55.0	2.6
V117@150	Vestas	89.0	3.3	3.8	4.8	4.8	17.5	58.7	2.7
V117@180	Vestas	119.0	3.3	4.1	4.8	4.8	17.5	58.7	2.7
V117@200	Vestas	139.0	3.3	4.1	4.8	4.8	17.5	58.7	2.7

Wind Turbine Type	Manufacturer	Mast length [m]	Mast $\varnothing$ top [m]	Mast $\varnothing$ base [m]	Nacelle Height [m]	Nacelle Width [m]	Nacelle Length [m]	Blade Length [m]	Blade Width [m]
V126@175	Vestas	109.8	3.1	4.1	4.8	4.8	17.5	63.1	2.9
V136@180	Vestas	109.8	3.3	4.1	4.8	4.8	17.6	67.7	2.6

*Note: After finishing the assessment study it became clear that the wind turbines at Fontenelle will not be build. As can be observed in Chapter 4 for the PSR at Florennes, Chapter 5 for the MSSR at Florennes and Chapter 6 for the SEAs, the effects of these wind turbines do not overlap with the effects that the newly planned wind turbines may cause.*

*In addition to this, two more wind turbines at Walcourt Florennes Gerpennes have been granted. These two will have the Lambert '72 coordinates X:160731 Y:110787 and X:161100 Y:111231 and are situated north east from the current wind farms at Walcourt, so at an even larger distance from the newly planned wind turbines than the current wind turbines at Walcourt.*

## 3.2 Radar Systems

### 3.2.1 Primary and secondary Radar System STAR 2000 Florennes

Figure 2.2 shows pictures of the radar installation of Florennes Military Airbase. The coordinates and antenna height have been provided by Skeyes [12]. The system consists of two components: a PSR (STAR 2000 from Thales France) and an MSSR. The DEA will be performed for the primary and secondary radar. The radar parameters that are relevant for this study are presented in Table 3.6 and have been received from Skeyes and from Thales France [2]. Apart from these parameters, a set of detailed parameters that are necessary for the modelling, have been provided under a Non-Disclosure Agreement (NDA) between Skeyes, Thales France and TNO. These cannot be shared with other parties [2]. The detailed operation of the Constant False Alarm Radar (CFAR) detection algorithm was, however, not shared by Thales. Therefore the operation of the CFAR processing is based on the STAR 2000 at Schiphol Airport in The Netherlands, which information was provided by The Netherlands Civil Air Service Provider, LVNL. The radar parameters of the MSSR that are relevant for this study are presented in Table 3.7.



Figure 3.4 The Airport Surveillance Radar at Florennes Airbase from Google Earth. The insert is taken from the internet.

Table 3.6 Relevant radar parameters of the PSR STAR 2000 at Florennes Airbase [2] & [12]

Parameter	Value
Antenna position	
X (Lambert '72)	170205
Y (Lambert '72)	101055
Latitude (WGS84)	50° 13' 12.85" (50.22024°) N
Longitude (WGS84)	4° 39' 6.72" (4.651867°) E
Height (EGM96)	33 m AGL 346 m AMSL
Antenna rotation speed	15 rpm
Instrumented range	60 NM (111 km)
Frequency	2700- 2900 MHz
Horizontal beamwidth (-3 dB)	1.4°
Range cell depth	116 m
CFAR	
Type	CAGO (Cell Averaging Greatest of)
Number of range cells within the early and late window	8 (Per window)
Number of guard cells on each sides of the CUT	2

Table 3.7 Relevant radar parameters of the MSSRs at Florennes Airbase [12].

Parameter	Value
Antenna position	Co-mounted on PSR
X (Lambert '72)	170205
Y (Lambert '72)	101055
Latitude (WGS84)	50° 13' 12.85" (50.22024°) N

Longitude (WGS84)	4° 39' 6.72" (4.651867°) E
Height (EGM96)	38 m AGL
	351 m AMSL
Number of elements	35

### 3.2.2 Primary Radar System Bertem

The AEG SRE-M5 L-band long range radar at Bertem and consists of both a PSR and an MSSR, see Figure 3.5. The assessment will be performed for the primary radar only. The coordinates and antenna height have been received from Skeyes formally known as Belgocontrol [2] and the Belgium Ministry of Defence [3]. The radar parameters that are relevant for this study are presented in Table 3.8.



Figure 3.5 The long range surveillance primary radar (CMB-S) at Bertem. (image: Google Earth).

Table 3.8 Relevant radar parameters of the AEG SRE-M5 PSR at Bertem [2] and [3].

Parameter	Value
Antenna position	
X (Lambert '72)	167446
Y (Lambert '72)	173746
Latitude (WGS84)	50° 52' 25.77" (50.873825) N
Longitude (WGS84)	4° 36' 59.85" (4.616625) E
Height (EGM96)	26 m AGL
	92 m AMSL
Antenna rotation speed	5 rpm
Instrumented range	110 NM (204 km)
Frequency	1215-1400 MHz
Horizontal beamwidth (-3 dB)	1.1°
Range cell depth	30 m
CFAR	
Type	CAGO (Cell Averaging Greatest of)

Parameter	Value
Number of range cells within the early and late window	32 (Per window)
Number of guard cells on each sides of the CUT	4

### 3.2.3 Primary Radar System Saint-Hubert

This Saint-Hubert airbase is equipped with a AEG SRE-M5 L-band long range radar and consists of both a PSR and an MSSR, see Figure 3.6. The PSR has recently been upgraded by the Belgium firm Intersoft-Electronics. The assessment will be performed for the primary radar only. The coordinates and antenna height have been received from Skeyes formally known as Belgocontrol [2] and the Belgium Ministry of Defence [3]. The radar parameters that are relevant for this study are presented in Table 3.9.



Figure 3.6 The long range primary surveillance radar (CMB-S) at Saint-Hubert Military Airbase. (image: Google Earth).

Table 3.9 Relevant radar parameters of the AEG SRE-M5 PSR at Saint-Hubert [2] and [3].

Parameter	Value
Antenna position	
X (Lambert '72)	225894
Y (Lambert '72)	80910
Latitude (WGS84)	50° 02' 04.52" (50.03459) N
Longitude (WGS84)	5° 25' 41.18" (5.42811) E
Height (EGM96)	41 m AGL 621 m AMSL
Antenna rotation speed	5 rpm
Instrumented range	110 NM (204 km)
Frequency	1215-1400 MHz
Horizontal beamwidth (-3 dB)	1.1°
Range cell depth	30 m
CFAR	
Type	CAGO (Cell Averaging Greatest of)

Parameter	Value
Number of range cells within the early and late window	32 (Per window)
Number of guard cells on each sides of the CUT	4

### 3.2.4 Primary Radar System Liège

Figure 2.2 shows pictures of the radar installation of Liège Airport. The coordinates and antenna height have been provided by Skeyes. The system consists of two components: a PSR (STAR 2000 from Thales France) and an MSSR. The assessment will be performed for the primary radar only. The radar parameters that are relevant for this study are presented in Table 3.6 and have been received from Skeyes and from Thales France [2]. Apart from these parameters, a set of detailed parameters that are necessary for the modelling, have been provided under a Non-Disclosure Agreement (NDA) between Skeyes, Thales France and TNO. These cannot be shared with other parties [2]. The STAR 2000 at Liege is from an older generation as the STAR 2000 radar at Florennes, Zaventem and Oostende and is slated for renewal in the near future. It will therefore not being equipped with the WFF enhancement. The potential improvement of such an enhancement will however be demonstrated in this study. The performance of the STAR 2000, including WFF, may be considered as representative for a typical modern ATC radar. The detailed operation of the Constant False Alarm Radar (CFAR) detection algorithm, especially in combination with the so-called Wind Farm Filter (WFF), was however not shared by Thales. Therefore the operation of the CFAR processing is based on the STAR 2000 at Schiphol Airport in The Netherlands, which information was provided by The Netherlands Civil Air Service Provider, LVNL.



Figure 3.7 The Airport Surveillance Radar at Liège Airport from Google Earth. The insert is from Skeyes.

Table 3.10 Relevant radar parameters of the PSR STAR 2000 at Liège Airport [2]

Parameter	Value
Antenna position	
X (Lambert '72)	223732
Y (Lambert '72)	149264
Latitude (WGS84)	50° 38' 57.64" (50.64934°) N
Longitude (WGS84)	5° 24' 40.85" (5.411347°) E
Height (EGM96)	22 m AGL 192 m AMSL
Antenna rotation speed	15 rpm
Instrumented range	60 NM (111 km)
Frequency	2700- 2900 MHz
Horizontal beamwidth (-3 dB)	1.4°
Range cell depth	116 m
CFAR	
Type	CAGO (Cell Averaging Greatest of)
Number of range cells within the early and late window	8 (Per window)
Number of guard cells on each sides of the CUT	2

### 3.2.5 Primary Radar System Zaventem

Figure 2.2 shows pictures of the radar installation at Zaventem Airport. The coordinates and antenna height have been provide by Skeyes. The system consists of two components: a PSR (STAR 2000 from Thales France) and an MSSR. The assessment will be performed for the primary radar of Zaventem only. The radar parameters that are relevant for this study are presented in Table 3.6 and have been received from Skeyes and from Thales France [2]. Apart from these parameters a high number of detailed parameters have been used to model the radar within TNO's radar performance assessment program PERSEUS. These parameters have been provided under a Non-Disclosure Agreement (NDA) between Skeyes, Thales France and TNO and cannot be shared with other parties [2]. The detailed operation of the Constant False Alarm Radar (CFAR) detection algorithm, especially the operation of the Wind Farm Filter (WFF) was however not shared by Thales. Therefore the operation of the CFAR processing is based on the STAR 2000 at Schiphol Airport in The Netherlands, which information was provided by The Netherlands Civil Air Service Provider, LVNL.



Figure 3.8 The Airport Surveillance Radar at Zaventem Airport from Google Earth. The insert is from Skeyes.

Table 3.11 Relevant radar parameters of the PSR at Zaventem Airport.

Parameter	Value
Antenna position	
X (Lambert '72)	159600
Y (Lambert '72)	175626
Latitude (WGS84)	50° 53' 26.91" (50.89091°) N
Longitude (WGS84)	4°309' 18.72" (4.50520) E
Height (EGM96)	17 m AGL 81 m AMSL
Antenna rotation speed	15 rpm
Instrumented range	60 NM (111 km)
Frequency	2700- 2900 MHz
Horizontal beamwidth (-3 dB)	1.4°
Range cell depth	116 m
CFAR	
Type	CAGO (Cell Averaging Greatest of)
Number of range cells within the early and late window	8 (Per window)
Number of guard cells on each sides of the CUT	2

## 4 Detailed Engineering Assessment Primary Surveillance Radar Florennes

### 4.1 PERSEUS results

The diagrams that are presented in the next sections present the single scan detection probability for a target with a radar cross section (RCS) of 2 m<sup>2</sup>. RCS fluctuation has been taken into account using the Swerling case 1 target fluctuation model. These parameters are commonly used when calculating the performance of Primary Air Traffic Control radars. Precipitation is not present.

The resolution with which the PERSEUS calculation was executed is 0.1° in azimuth and 25 m in range. The resolution of the final coverage diagrams, i.e., the pixel size, is approximately 25 m by 25 m.

The detection probability has been determined at four target altitudes: 1000, 2000, 4000 and 10000 ft above ground level (AGL). For each altitude we have calculated the detection diagram without wind turbines and with the newly planned wind turbines (yellow dots) installed as well. Of each coverage diagram six versions are shown:

- (1) The total coverage of the radar without any wind turbines.
- (2) The total coverage of the radar including the existing and authorised wind turbines within a 20 km circle around the newly planned wind turbines.
- (3) The total coverage of the radar including the existing, authorised and newly planned wind turbines.
- (4) The loss of coverage due to the shadow of the turbines, without the newly planned wind turbines.
- (5) The loss of coverage due to the shadow of the turbines with the newly planned wind turbines.
- (6) The loss of detection zoomed in above position of the newly planned wind turbines.

In all coverage diagrams, shadow effects behind the wind turbines are visible. In the other images, potential effects of desensitization overhead can be observed. For the existing, authorised and newly planned turbines at short distance to the radar, loss of detection is visible at some distance down range, caused by time sidelobes of the compressed pulse. At low target heights large areas of low detection are shown, which is caused by large landclutter returns. At 2000 ft and higher, these areas only appear at ranges larger than 8 NM or 14.8 km, i.e., the distance at which the radar system switches from high to low receive beam.

For the diagrams showing the full coverage, the blue colors show the terrain profile, which is used as background. The color indicator for all radar detection probability diagrams is given in each diagram. A detection probability ( $P_d$ ) of 90% or higher is green, 89% is light blue and from 88% downwards the colour changes from yellow to red. A detection probability of 70% or less is dark red. At 0% the diagram is transparent which means that the background becomes visible. The Controlled Traffic Region (CTR) of the Military Airbase Florennes and its neighbouring airports or airbases are projected as an overlay.

4.1.1 Coverage diagrams STAR 2000 for a target at 1000 ft AGL

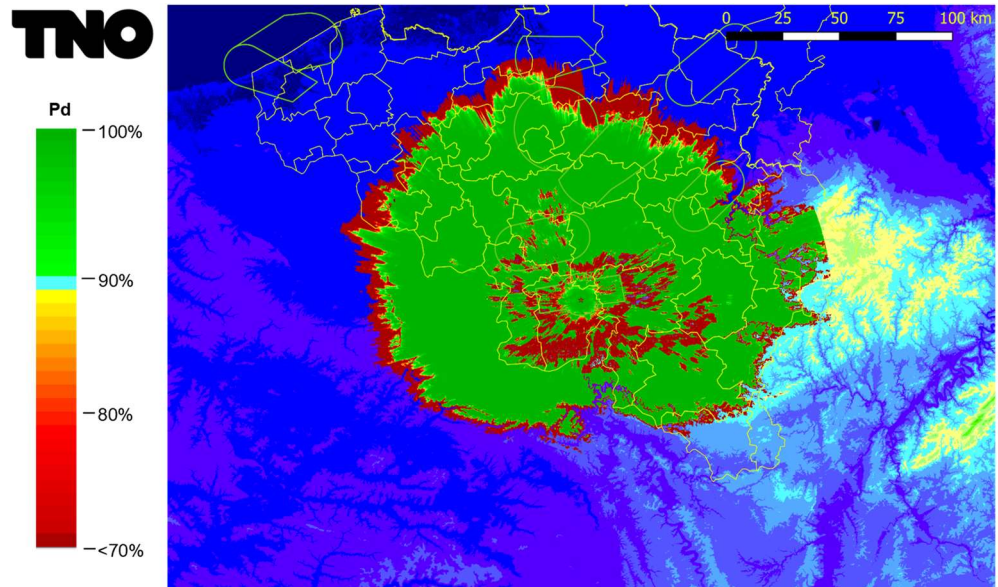


Figure 4.1 Coverage diagram of the STAR 2000 without any wind turbines (baseline) for a target at 1000 ft AGL. The large areas of low detection probability are caused by land clutter return.

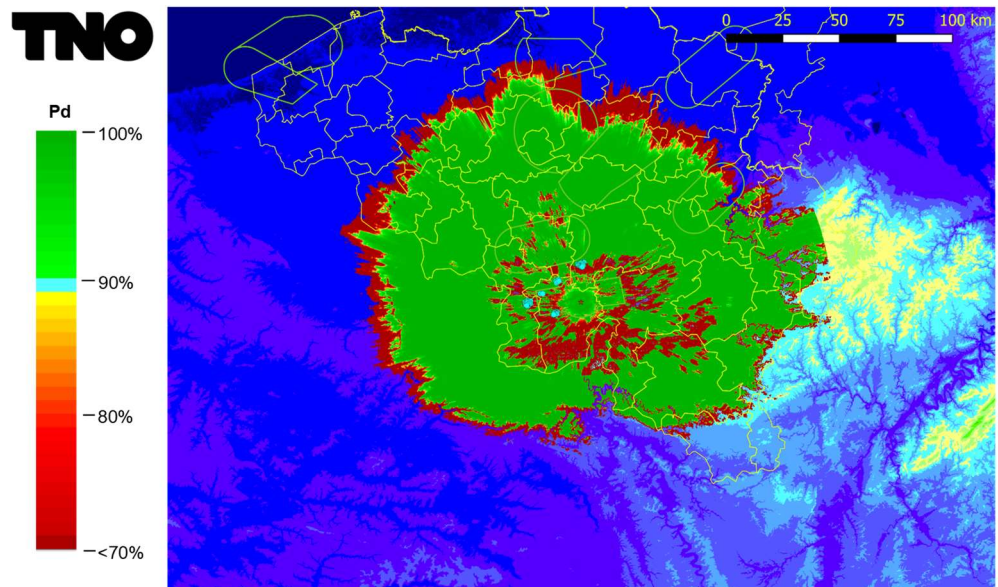


Figure 4.2 Coverage diagram of the STAR 2000 with the existing and authorised wind turbines (blue dots) within a circle with a radius of 20 km around the newly planned wind turbines at Chastres-Walcourt for a target at 1000 ft AGL.

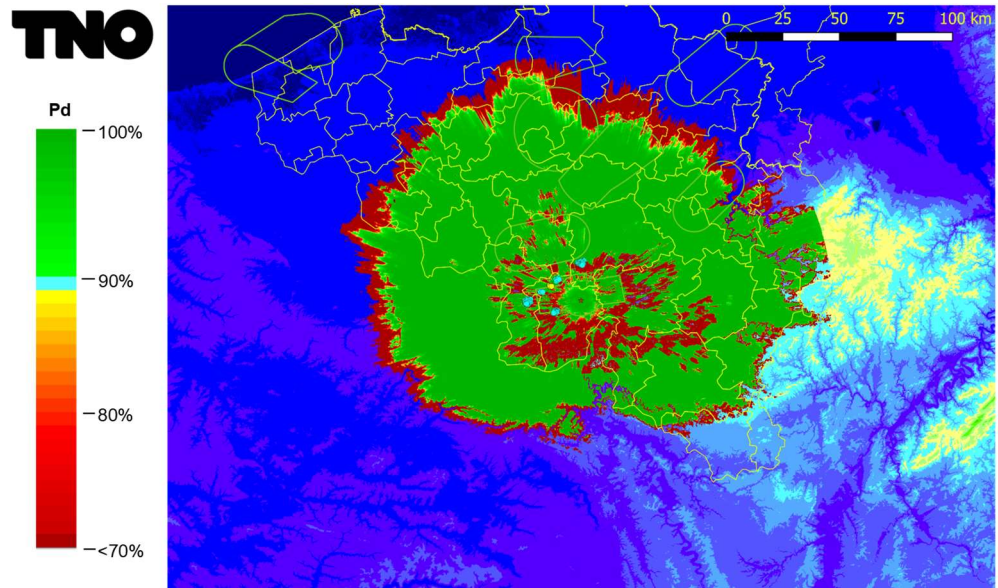


Figure 4.3 Coverage diagram of the STAR 2000 with the existing and authorised wind turbines (blue dots) including the newly planned wind turbines at Chastrès-Walcourt (yellow dots) for a target at 1000 ft AGL.

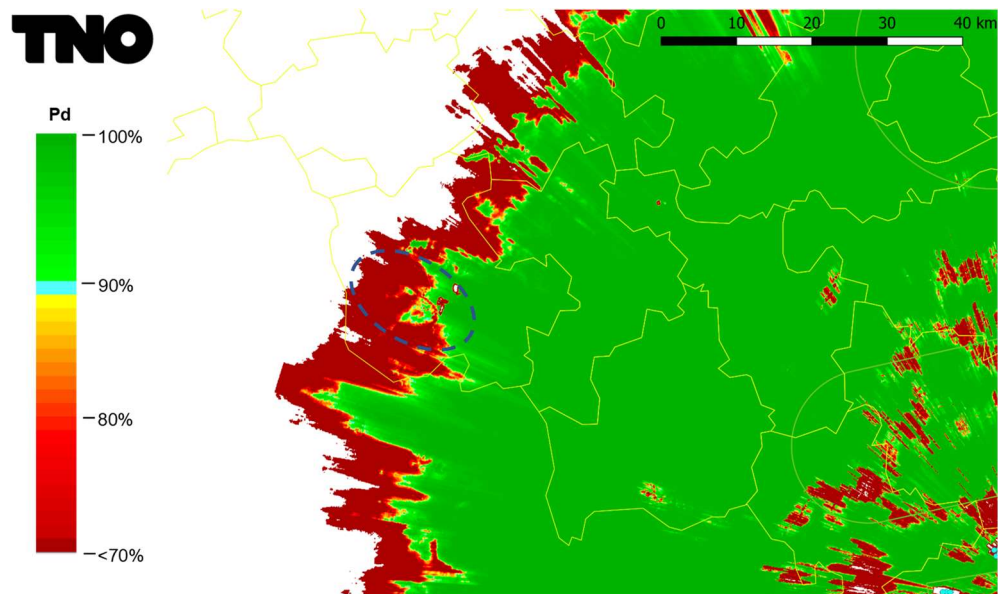


Figure 4.4 The maximum detection range with all existing and authorised wind turbines at 1000 ft AGL. The loss of detection some km down range from the nearby wind turbines is caused by time sidelobes of the compressed pulse. The area where the loss of detection range may occur, is indicated within the dotted ellipse.

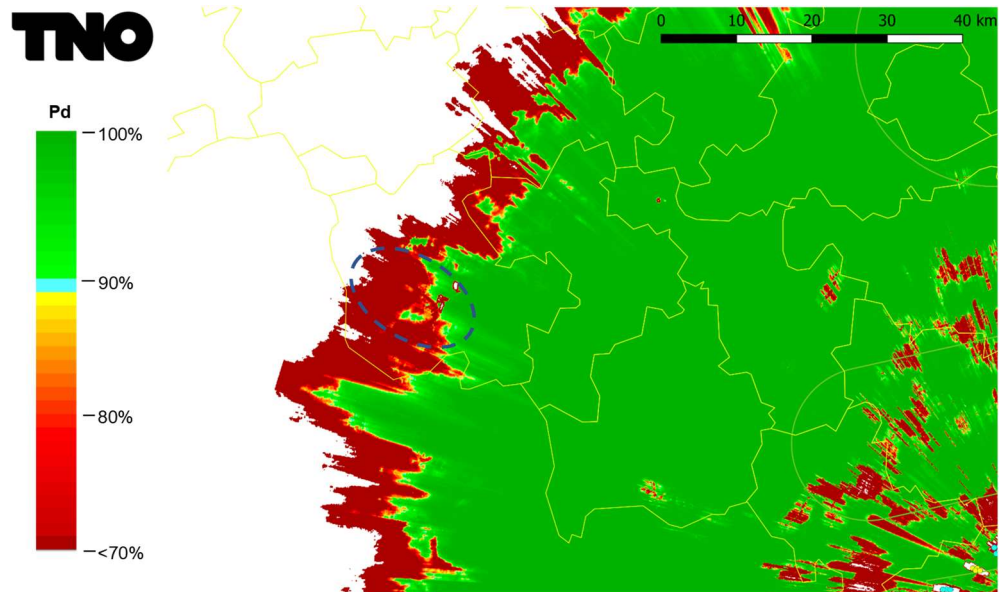


Figure 4.5 The maximum detection range with all existing and authorised wind turbines, including the newly planned wind turbines at 1000 ft AGL. The area where the loss of detection range occurs, is indicated within the dotted ellipse. The loss of detection some km down range from the nearby wind turbines is caused by time sidelobes of the compressed pulse.

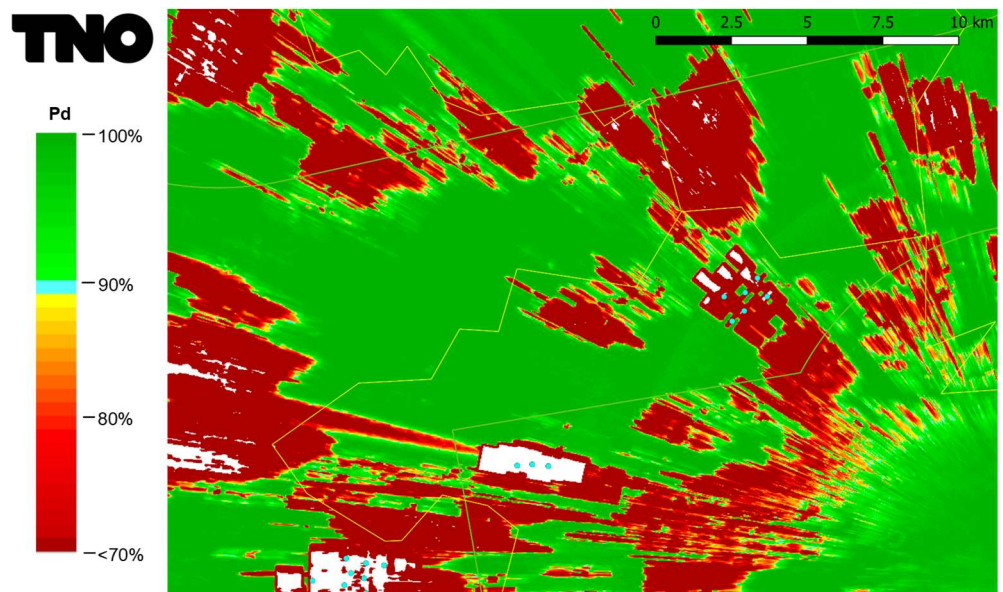


Figure 4.6 Coverage diagram of the STAR 2000 above the positions of all existing and authorised wind turbine for a target at 1000 ft AGL.

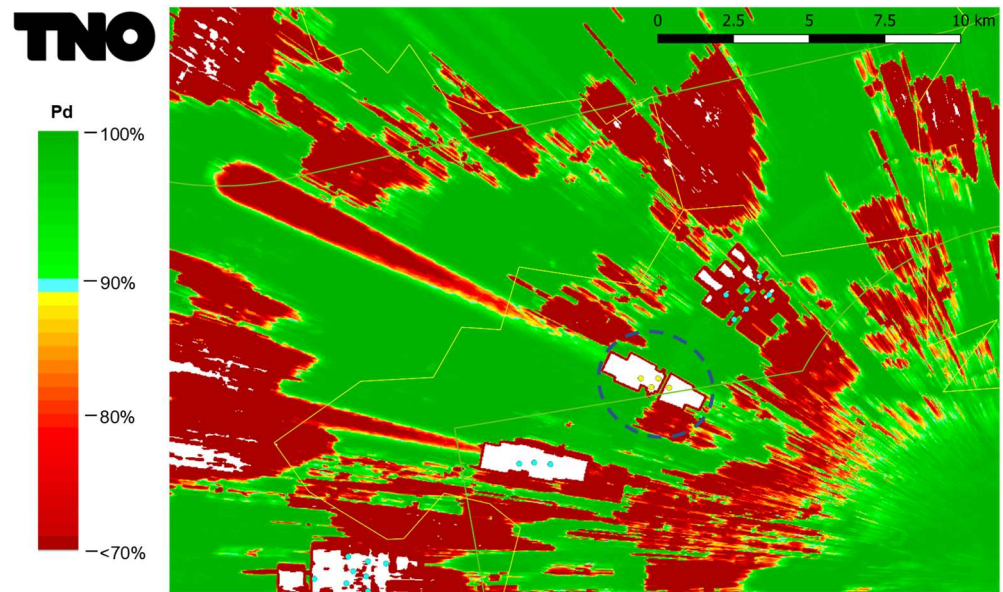


Figure 4.7 Coverage diagram of the STAR 2000 as shown in Figure 4.6 but including the newly planned wind turbines at Chastrès-Walcourt (yellow dot). The desensitisation overhead caused by the CFAR is visible within the dotted ellipse. The loss of detection some km down range from the wind turbines is caused by time sidelobes of the compressed pulse.

4.1.2 Coverage diagrams STAR 2000 for a target at 2000 ft AGL

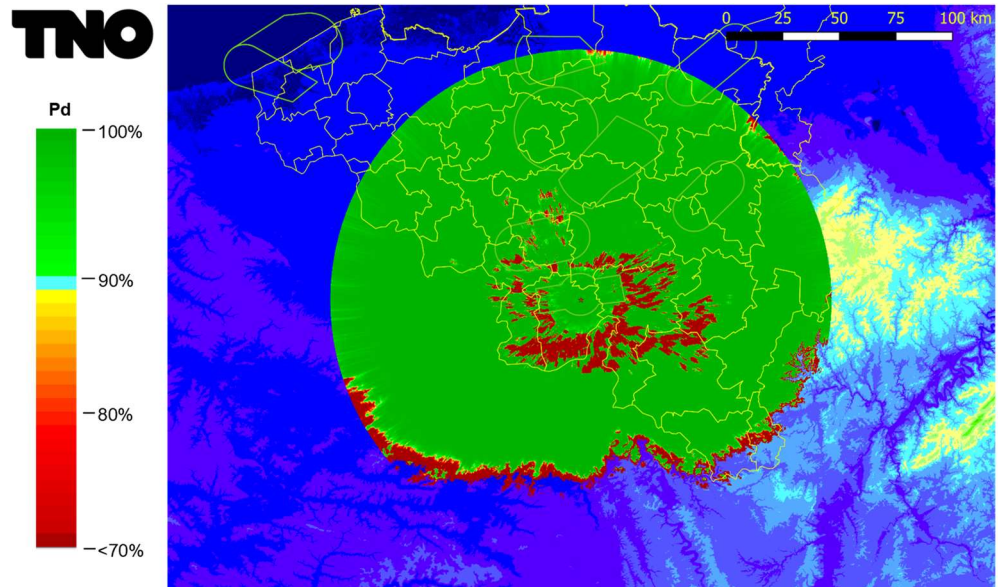


Figure 4.8 Coverage diagram of the STAR 2000 without any wind turbines (baseline) for a target at 2000 ft AGL. The land clutter return is now only visible from a range of 8 NM or 14.8 km, *i.e.*, the switching distance between high and low receive beam.

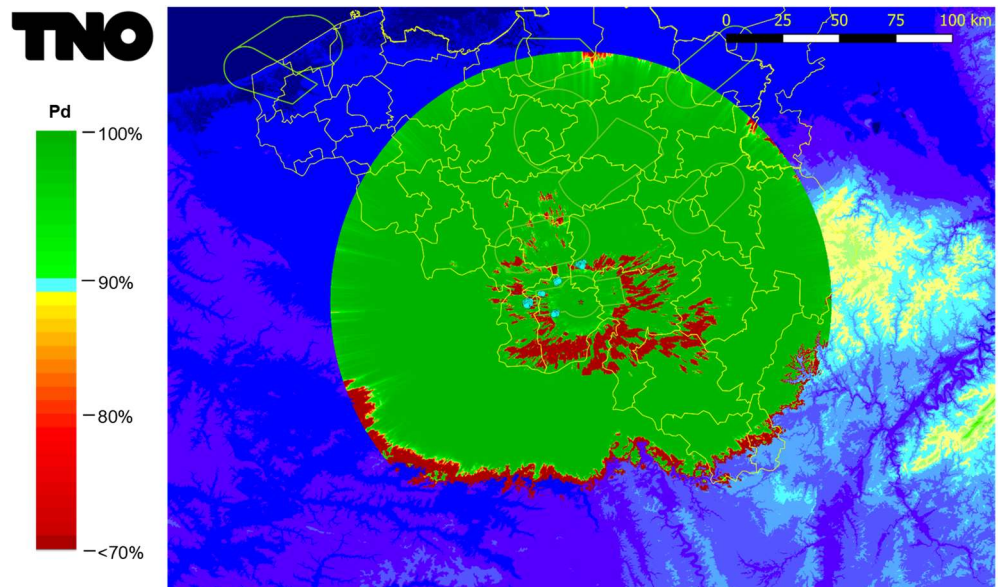


Figure 4.9 Coverage diagram of the STAR 2000 with the existing and authorised wind turbines (blue dots) within a circle with a radius of 20 km around the newly planned wind turbines at Chastres-Walcourt for a target at 2000 ft AGL.

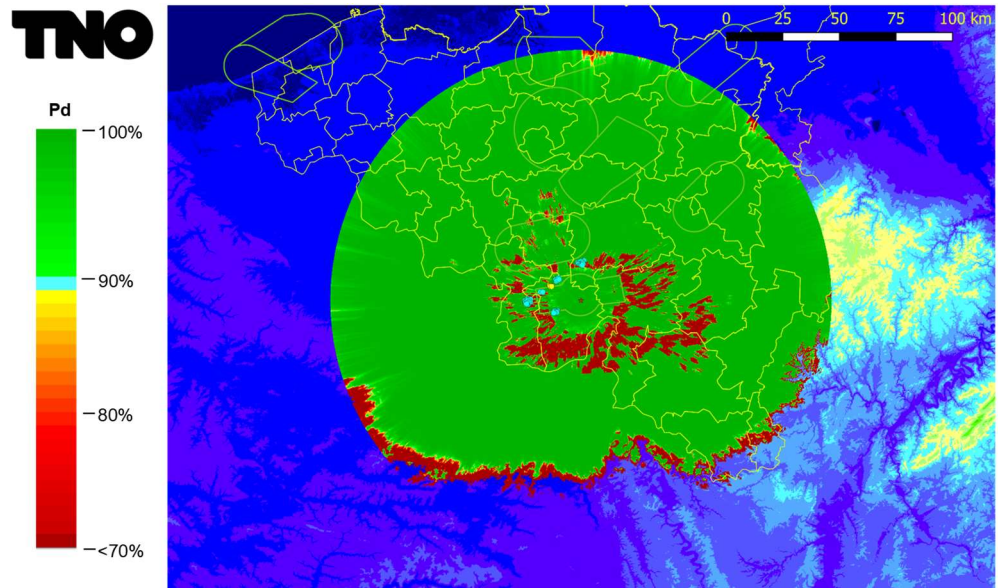


Figure 4.10 Coverage diagram of the STAR 2000 with the existing and authorised wind turbines (blue dots) including the newly planned wind turbines at Chastrès-Walcourt (yellow dots) for a target at 2000 ft AGL.

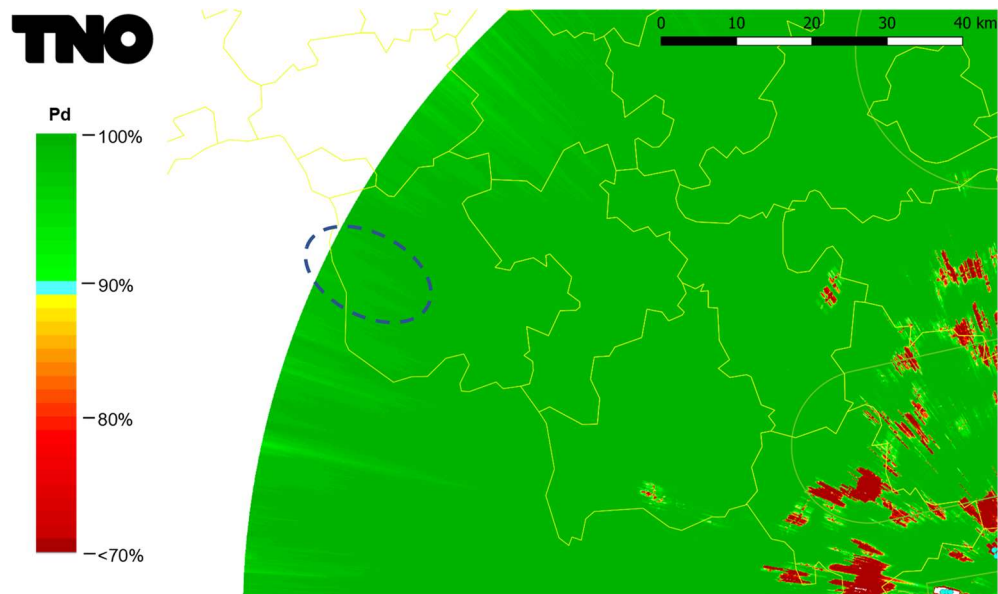


Figure 4.11 The maximum detection range with all existing and authorised wind turbines at 2000 ft AGL. The area where the loss of detection range may occur, is indicated within the dotted ellipse.

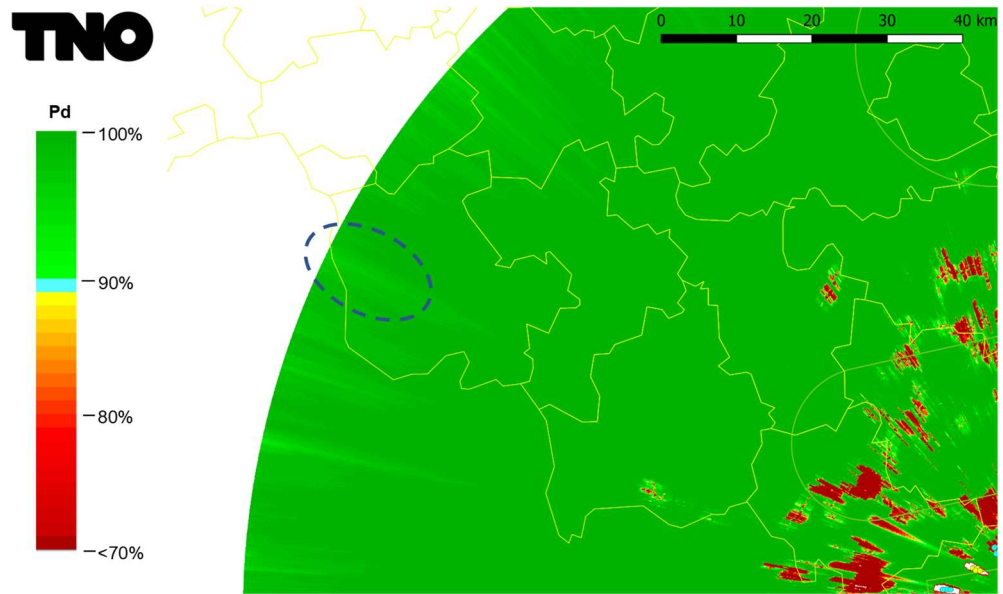


Figure 4.12 The maximum detection range with all existing and authorised wind turbines, including the newly planned wind turbines at 2000 ft AGL. The area where the loss of detection range occurs, is indicated within the dotted ellipse. At this height the maximum detection range is limited by the instrumented range.

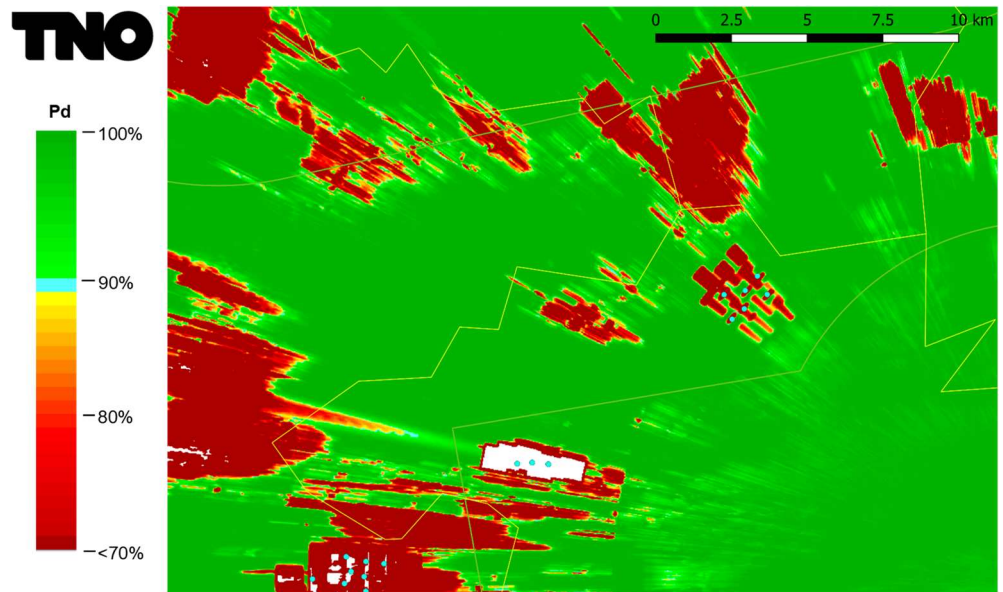


Figure 4.13 Coverage diagram of the STAR 2000 above the positions of all existing and authorised wind turbine for a target at 2000 ft AGL. The desensitization overhead effect within the CFAR window is clearly visible.

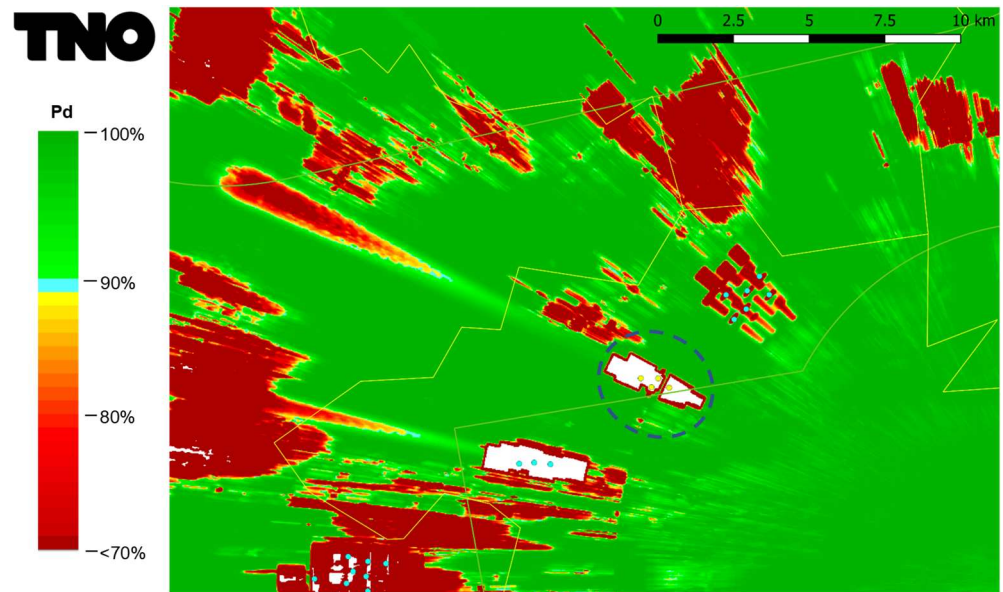


Figure 4.14 Coverage diagram of the STAR 2000 above the positions of all existing and authorised wind turbine, including the newly planned wind turbines at Chastrès-Walcourt (yellow dots). The desensitisation overhead caused by the CFAR is visible within the dotted ellipse. The loss of detection some km down range from the wind turbines is caused by time sidelobes of the compressed pulse.

4.1.3 Coverage diagrams STAR 2000 for a target at 4000 ft AGL

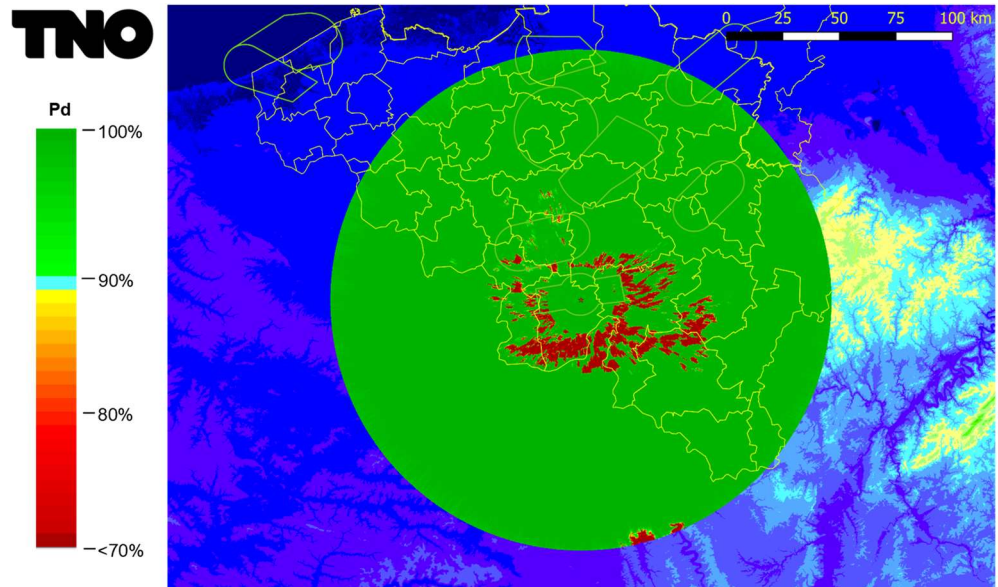


Figure 4.15 Coverage diagram of the STAR 2000 without any wind turbines (baseline) for a target at 4000 ft AGL. The land clutter return is now only visible from a range of 8 NM or 14.8 km, *i.e.*, the switching distance between high and low receive beam.

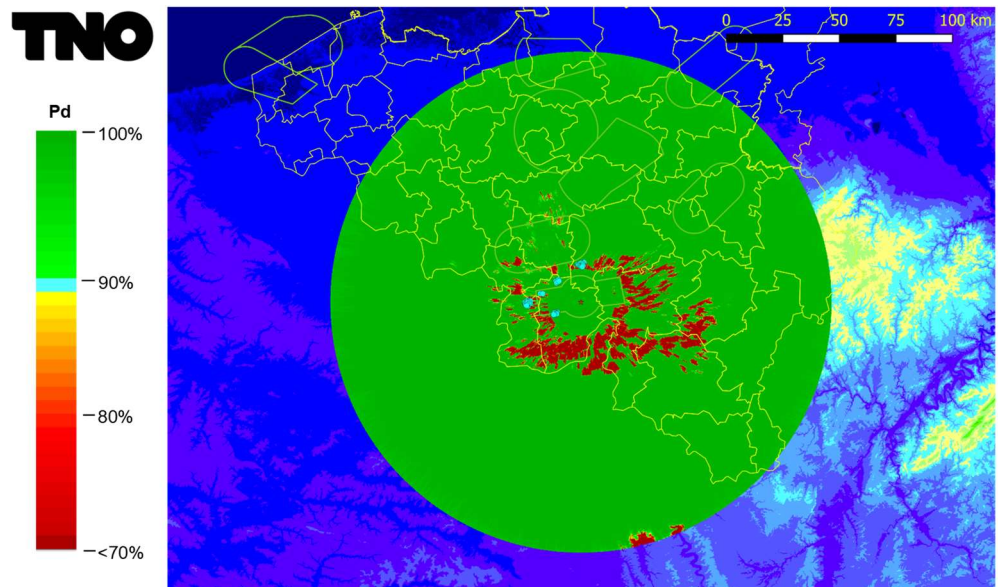


Figure 4.16 Coverage diagram of the STAR 2000 with the existing and authorised wind turbines (blue dots) within a circle with a radius of 20 km around the newly planned wind turbines at Chastres-Walcourt for a target at 4000 ft AGL.

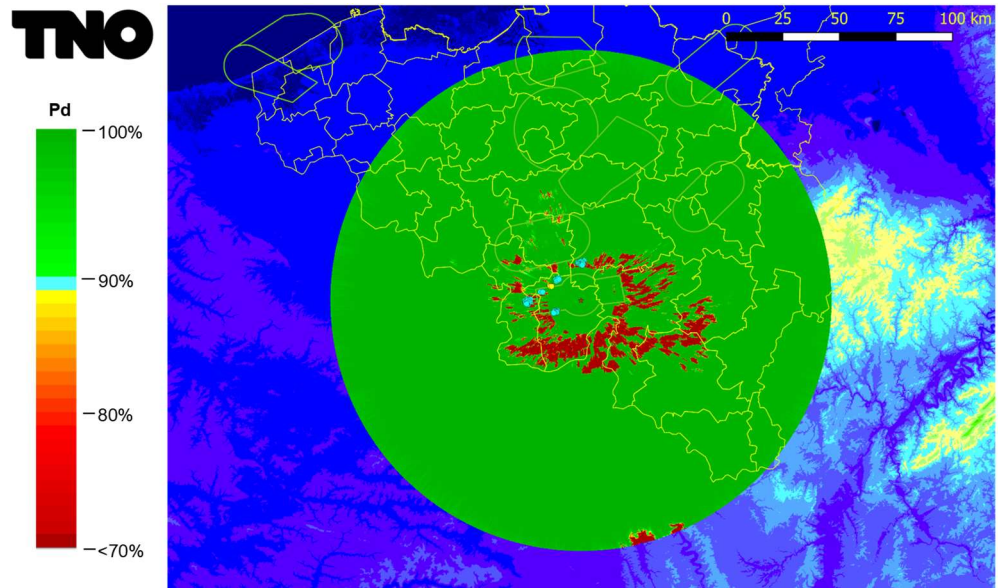


Figure 4.17 Coverage diagram of the STAR 2000 with the existing and authorised wind turbines (blue dots) including the newly planned wind turbines at Chastrès-Walcourt (yellow dots) for a target at 4000 ft AGL.

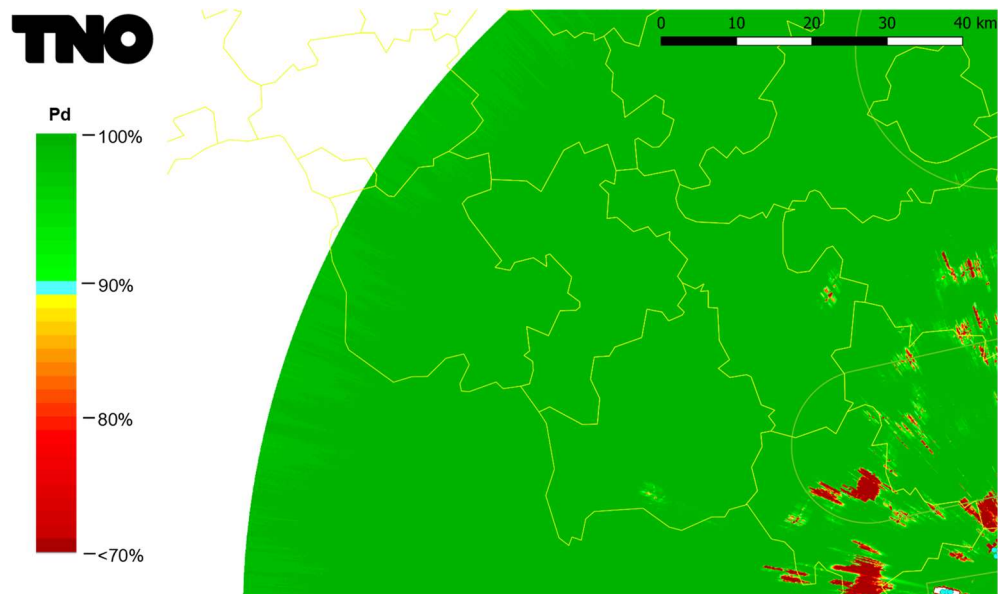


Figure 4.18 The maximum detection range with all existing and authorised wind turbines at 4000 ft AGL.

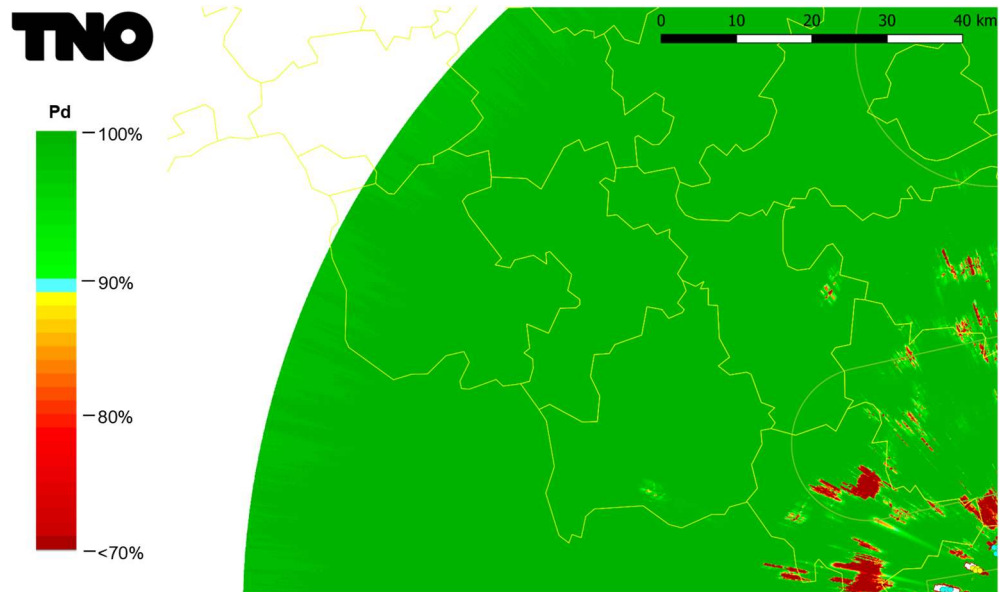


Figure 4.19 The maximum detection range with all existing and authorised wind turbines, including the newly planned wind turbines at 4000 ft AGL. The maximum range is only determined by the instrumented range of the radar.

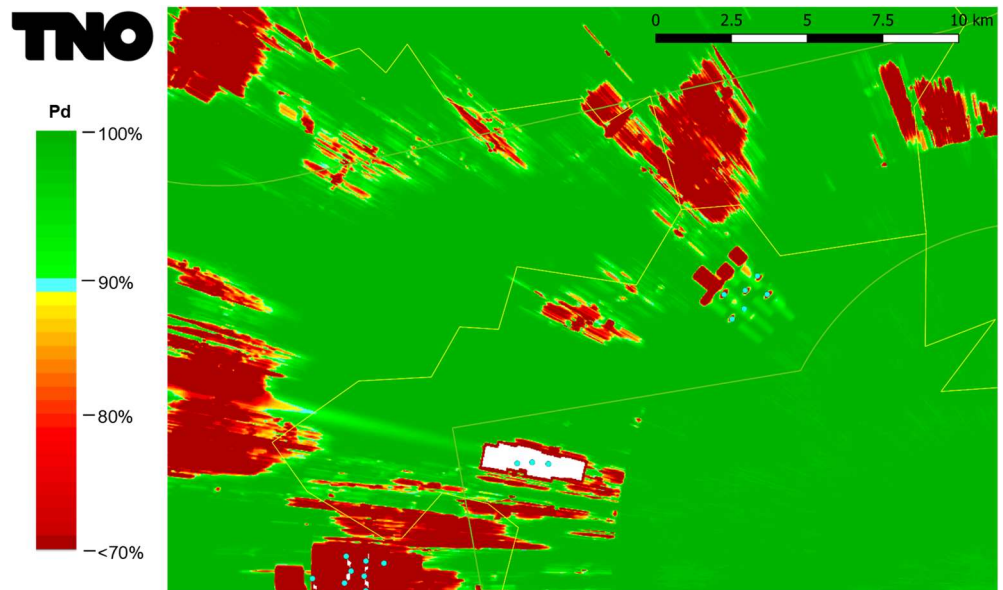


Figure 4.20 Coverage diagram of the STAR 2000 above the positions of all existing and authorised wind turbine for a target at 4000 ft AGL.

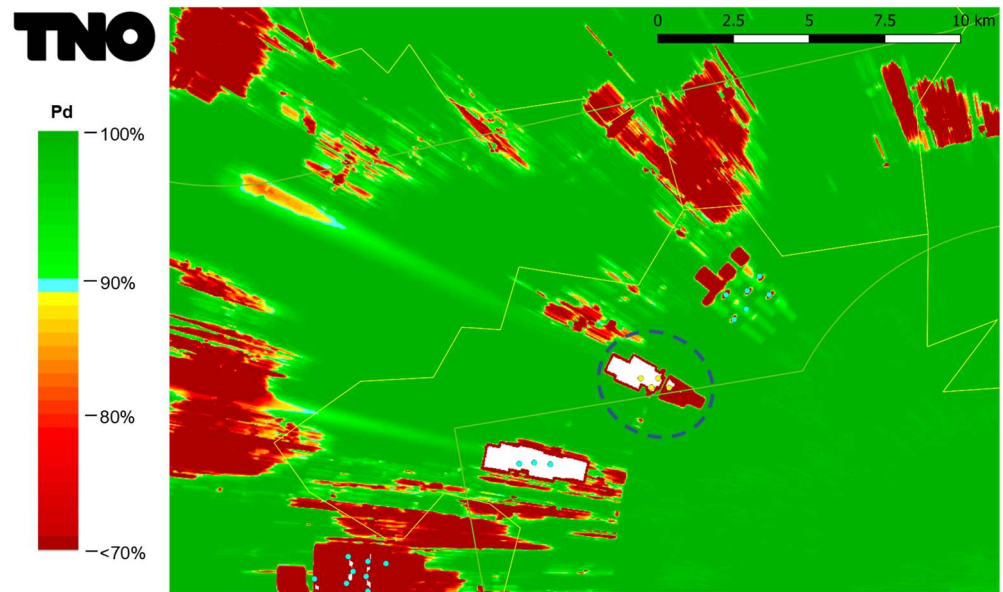


Figure 4.21 Coverage diagram of the STAR 2000 above the positions of all existing and authorised wind turbine, including the newly planned wind turbines at Chastrès-Walcourt (yellow dots). The desensitisation overhead caused by the CFAR is visible within the dotted ellipse. The loss of detection some km down range from the wind turbines is caused by time sidelobes of the compressed pulse.

4.1.4 Coverage diagrams STAR 2000 for a target at 10000 ft AGL

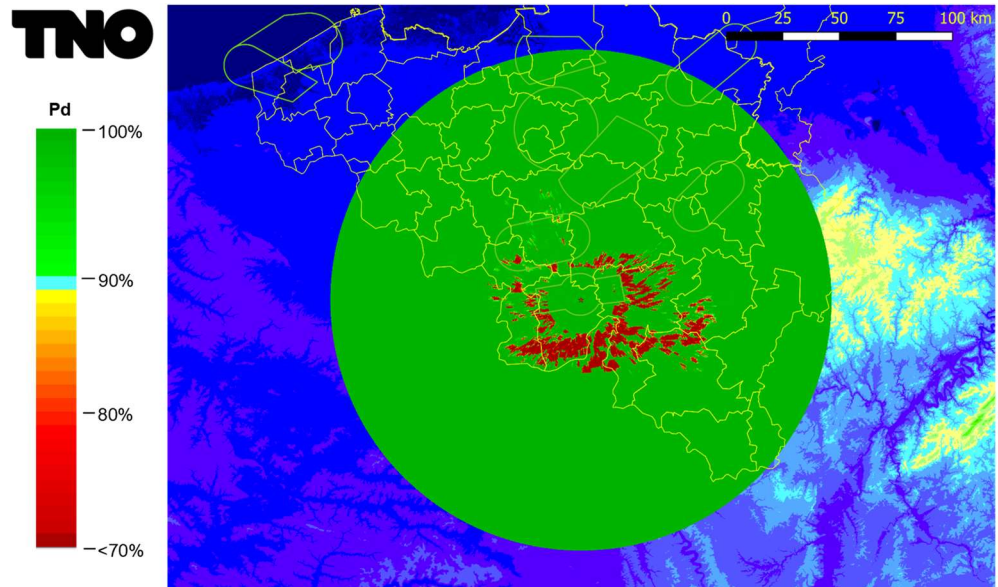


Figure 4.22 Coverage diagram of the STAR 2000 without any wind turbines (baseline) for a target at 10000 ft AGL. The land clutter return is now only visible from a range of 8 NM or 14.8 km, *i.e.*, the switching distance between high and low receive beam.

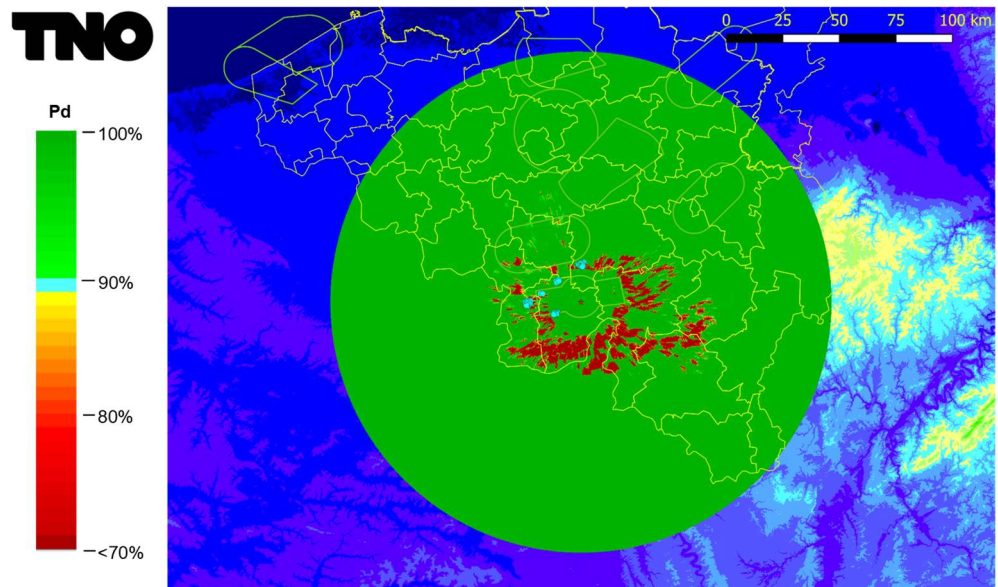


Figure 4.23 Coverage diagram of the of the STAR 2000 with the existing and authorised wind turbines (blue dots) within a circle with a radius of 20 km around the newly planned wind turbines at Chastres-Walcourt for a target at 10000 ft AGL.

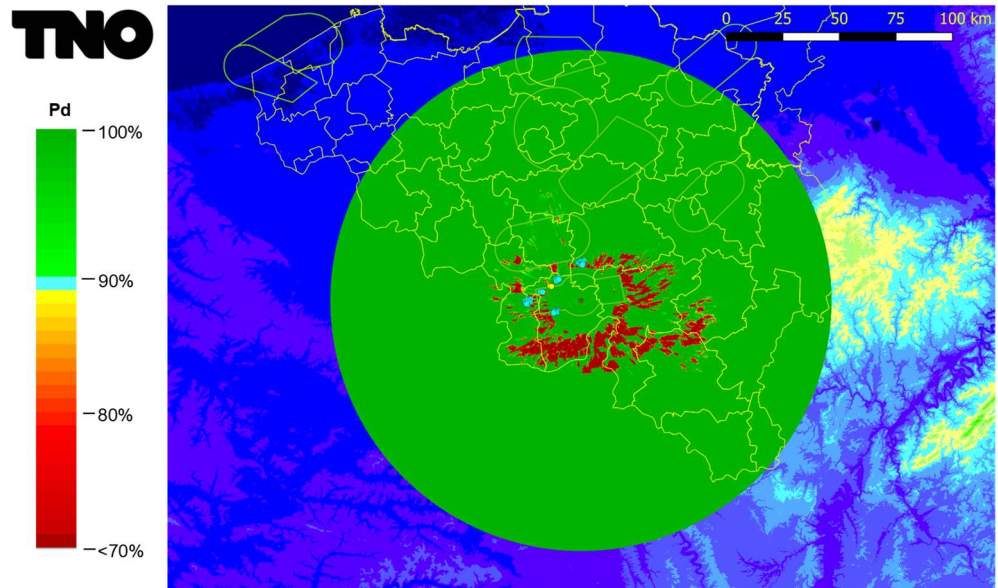


Figure 4.24 Coverage diagram of the of the STAR 2000 with the existing and authorised wind turbines (blue dots) including the newly planned wind turbines at Chastrès-Walcourt (yellow dots) for a target at 10000 ft AGL.

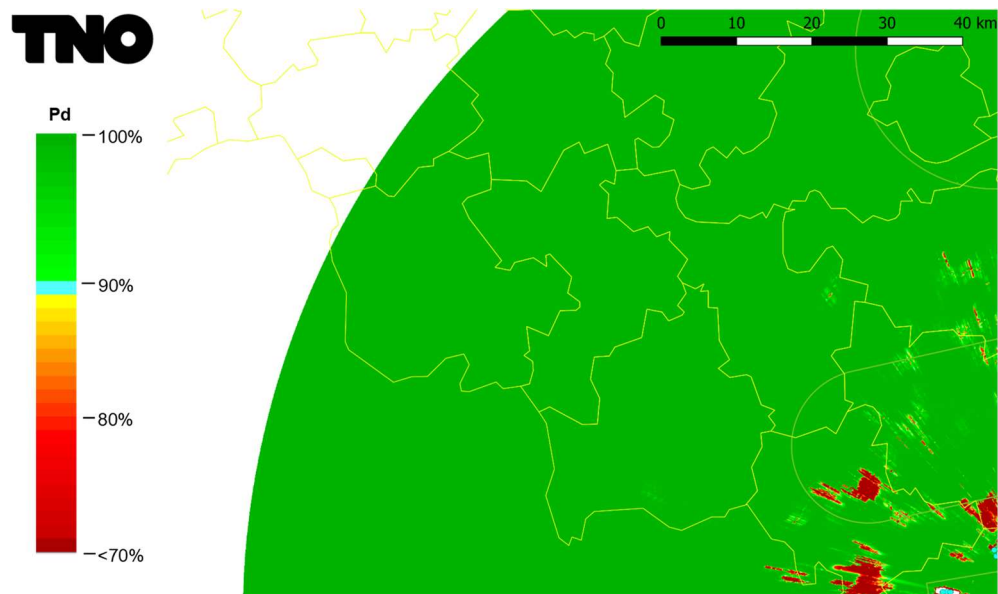


Figure 4.25 The maximum detection range with all existing and authorised wind turbines at 10000 ft AGL.

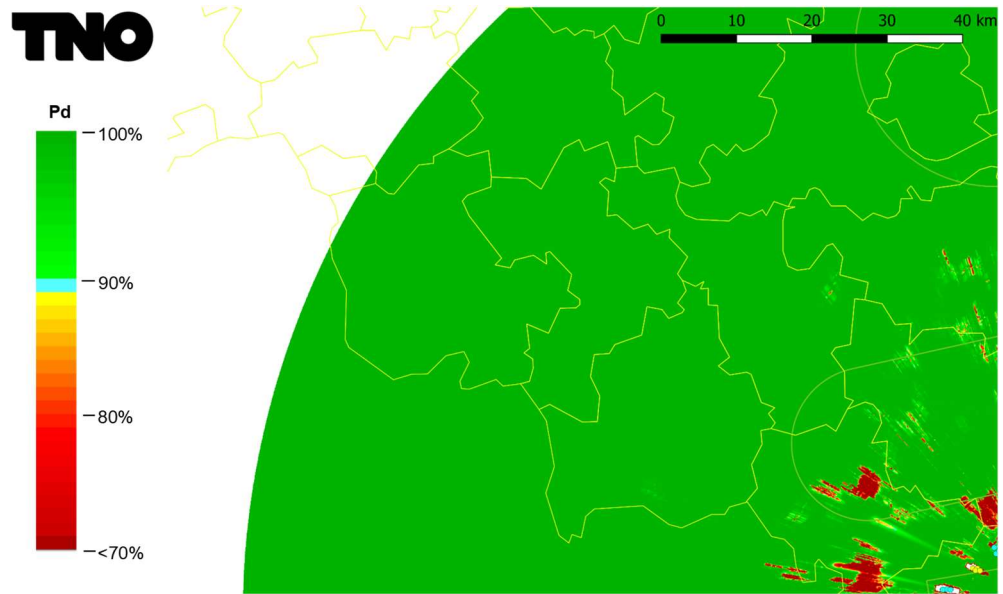


Figure 4.26 Coverage diagram of the STAR 2000 above the positions of all existing and authorised wind turbine, including the newly planned wind turbines at 10000 ft AGL. At this height the maximum detection range is limited by the instrumented range.

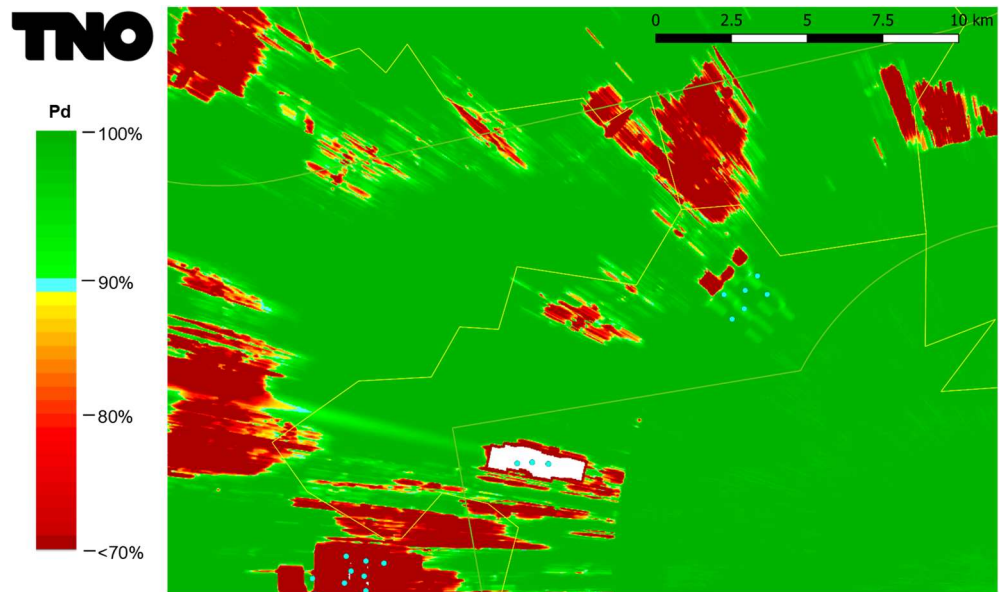


Figure 4.27 Coverage diagram of the STAR 2000 above the positions of all existing and authorised wind turbine for a target at 10000 ft AGL.

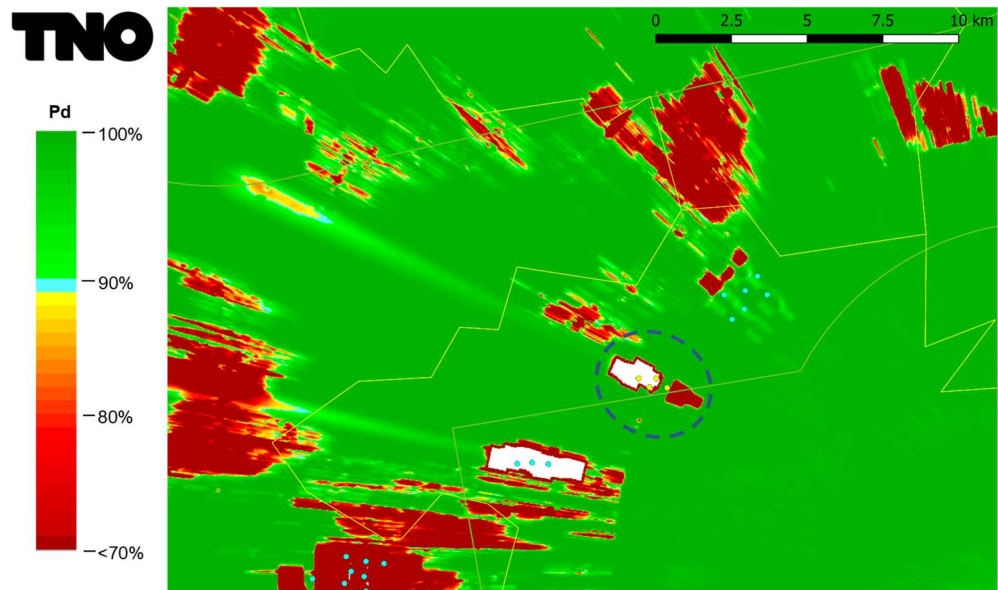


Figure 4.28 Coverage diagram of the STAR 2000 as shown in Figure 4.27 but including the newly planned wind turbines at Chastrès-Walcourt (yellow dots). The desensitisation overhead caused by the CFAR is visible within the dotted ellipse.

## 4.2 Observations and remarks

In the previous section volumes with reduced detection capability due to wind turbines have been shown. The different phenomena that cause this effect are described in the following subsections.

### 4.2.1 *Shadow effect*

As explained in more detail in section 2.3 the presence of a wind turbine will cause a loss in maximum detection range, in the sector behind the wind turbines. This effect, in fact, is visible up to the calculated target heights up to 2000 ft AGL. The maximum loss measures from 1.5 km to maximum 4.0 km in a narrow sector behind the newly planned wind turbines at Chastrès-Walcourt at 1000 ft AGL. See Figure 4.29 for the situation with the existing and authorised wind turbines and Figure 4.30 including the newly planned wind turbines. From altitudes of 4000 ft AGL and higher, the maximum detection range is limited by the instrumented range of 60 NM (111 km) of the radar.

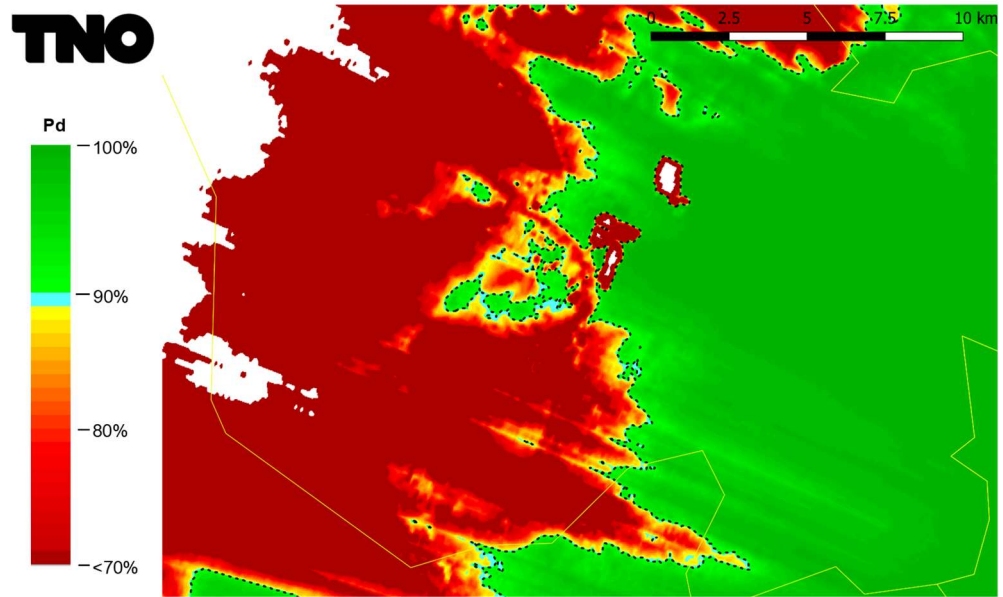


Figure 4.29 The maximum detection range of the radar with the existing and authorised wind turbines at 1000 ft AGL. The dotted line corresponds to a detection probability of 90%.

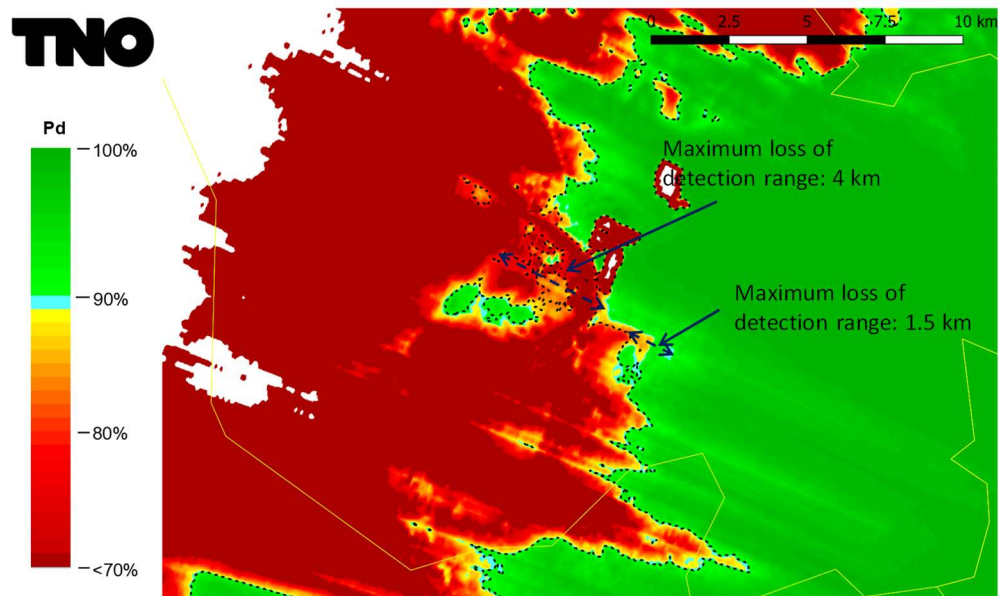


Figure 4.30 Loss of detection range due to the shadow effect of the wind turbine at 1000 ft AGL. The dotted line corresponds to a detection probability of 90% without the newly planned wind turbines. The maximum loss ranges from 1.5 km to maximum 4 km in a sector behind the newly planned wind turbines.

#### 4.2.2 *Desensitisation overhead*

As explained in more detail in section 2.4 the presence of a wind turbine will cause loss of detection above the wind turbine or in its direct neighbourhood caused by the so-called CFAR processing of the radar. The loss of detection above the newly planned wind turbines is smaller than the current wind turbines in the direct neighbourhood. Especially for the wind turbines that are located at a distance slightly larger than the switching range (in this case 8 NM typically) from high to low beam. The newly planned wind turbines are located at this range. The received wind turbine clutter power is obviously not related to the aircraft altitude, as illustrated in Figure 2.6 of section 2.3. However, as low-altitude aircraft are observed with less antenna gain, the effect is more pronounced for low flying targets.

### 4.3 STAR 2000 Wind Farm Filter

Thales has installed the so-called Wind Farm Filter in the STAR-2000 at Florennes. that improve the CFAR performance at a wind turbine position. See also section 2.5. Figure 4.31 to Figure 4.38 show the radar detection probability diagrams above the wind farm for a target height from 1000 to 10000 ft AGL without and with the WFF enhancement. As can be observed, the WFF improves the performance. The reduction of the detection probability is now limited to only directly above a wind turbine.

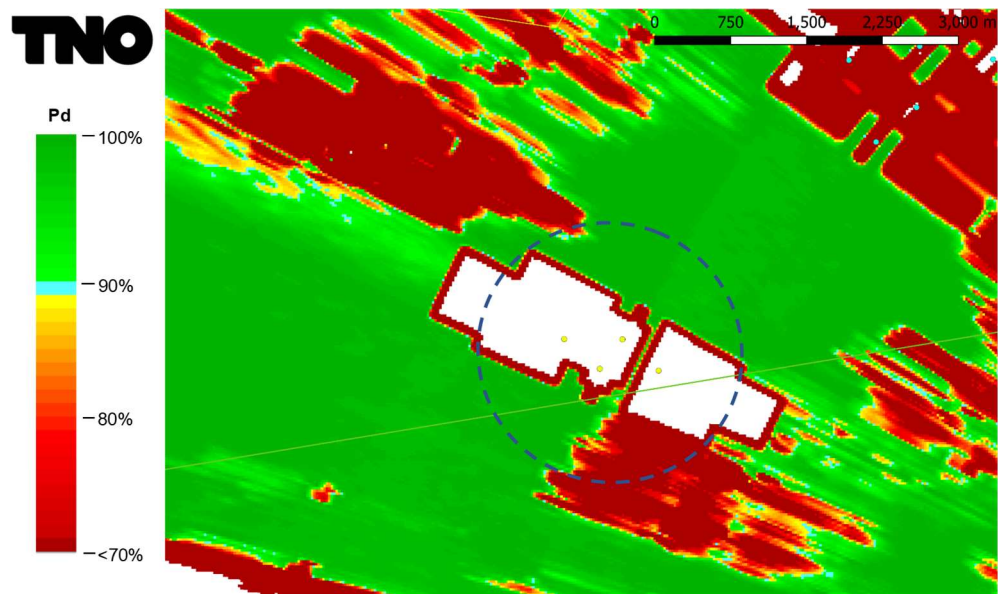


Figure 4.31 Coverage diagram of the standard STAR 2000, excluding the Wind Farm Filter enhanced processing, zoomed in at the planned position of the new wind turbines for a target at 1000 ft AGL.

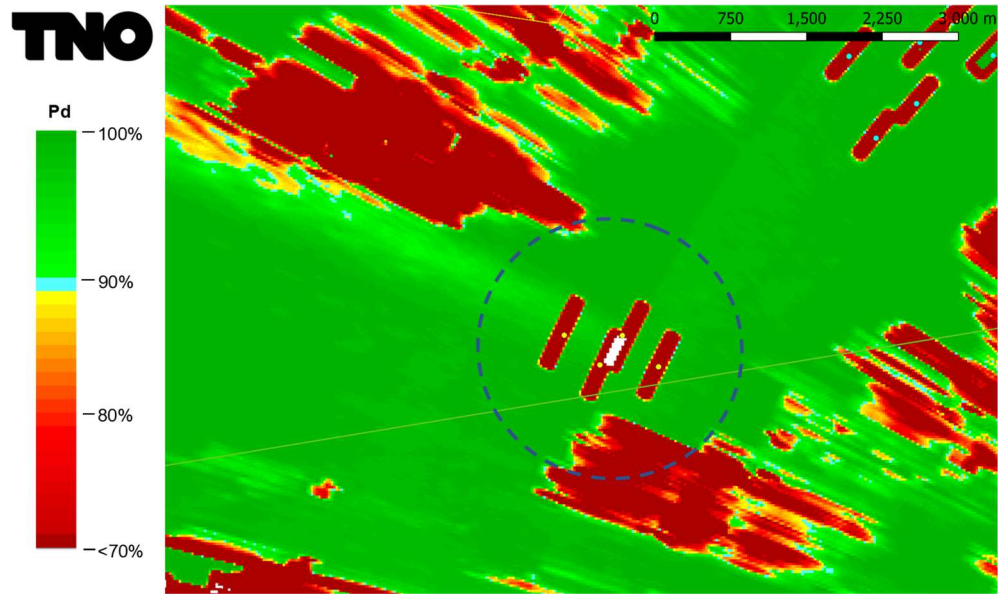


Figure 4.32 Coverage diagram of the STAR 2000 including the Wind Farm Filter enhanced processing, zoomed in at the planned position of the new wind turbines for a target at 1000 ft AGL.

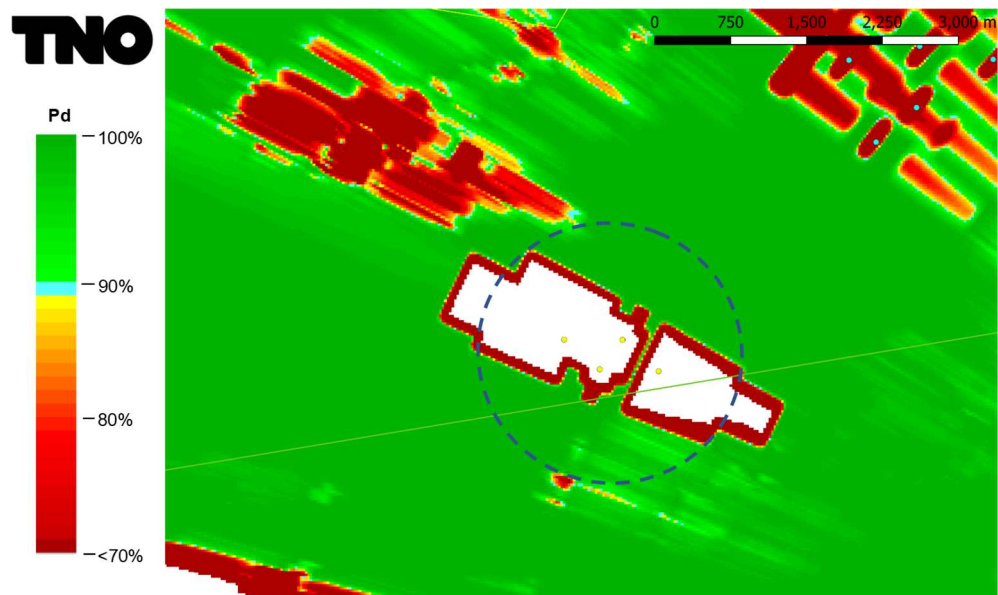


Figure 4.33 Coverage diagram of the standard STAR 2000, excluding the Wind Farm Filter enhanced processing, zoomed in at the planned position of the new wind turbines for a target at 2000 ft AGL.

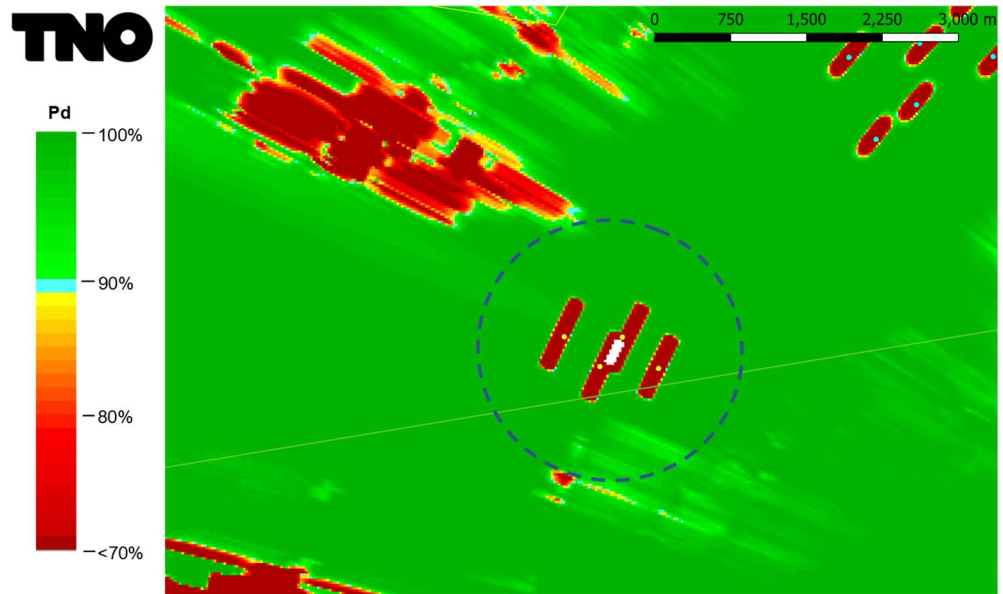


Figure 4.34 Coverage diagram of the STAR 2000 including the Wind Farm Filter enhanced processing, zoomed in at the planned position of the new wind turbines for a target at 2000 ft AGL.

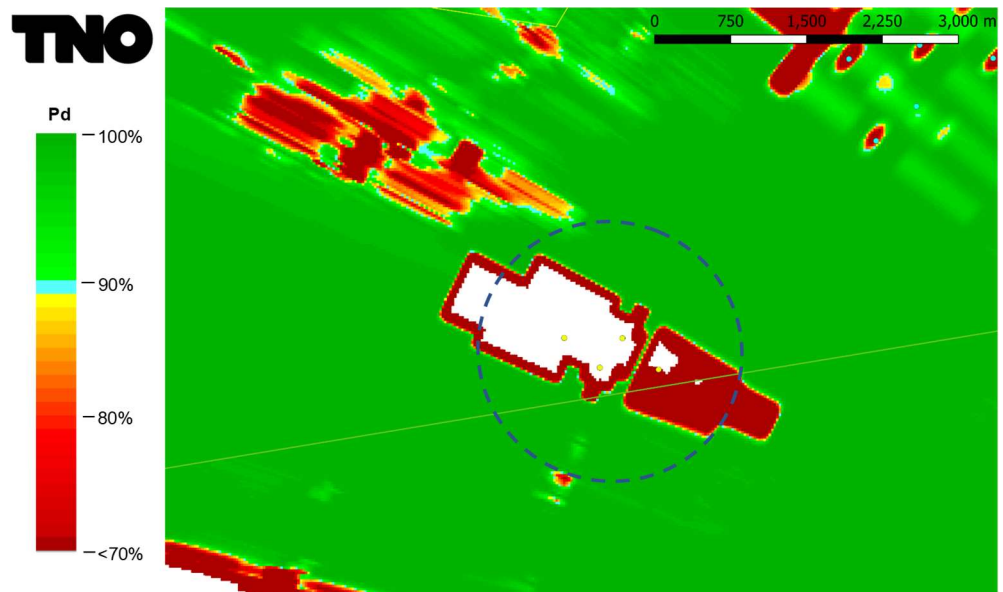


Figure 4.35 Coverage diagram of the standard STAR 2000, excluding the Wind Farm Filter enhanced processing, zoomed in at the planned position of the new wind turbines for a target at 4000 ft AGL.

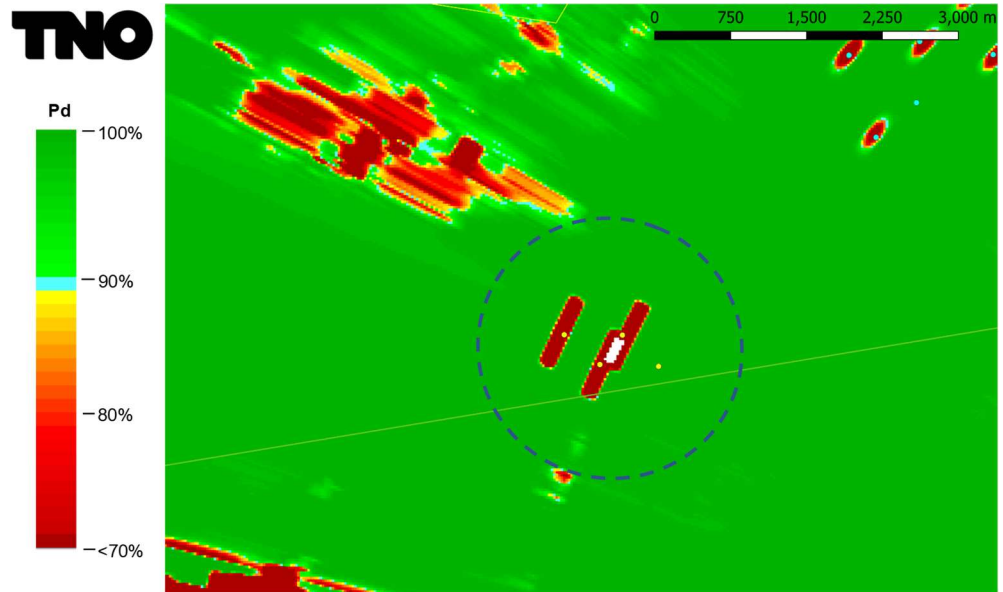


Figure 4.36 Coverage diagram of the STAR 2000 including the Wind Farm Filter enhanced processing, zoomed in at the planned position of the new wind turbines for a target at 4000 ft AGL.

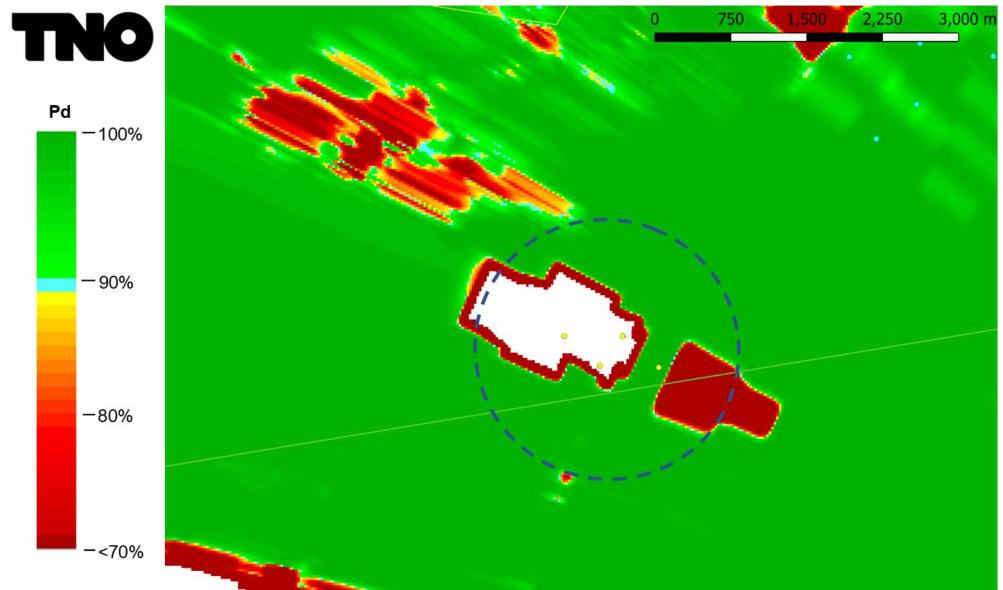


Figure 4.37 Coverage diagram of the standard STAR 2000, excluding the Wind Farm Filter enhanced processing, zoomed in at the planned position of the new wind turbines for a target at 10000 ft AGL.

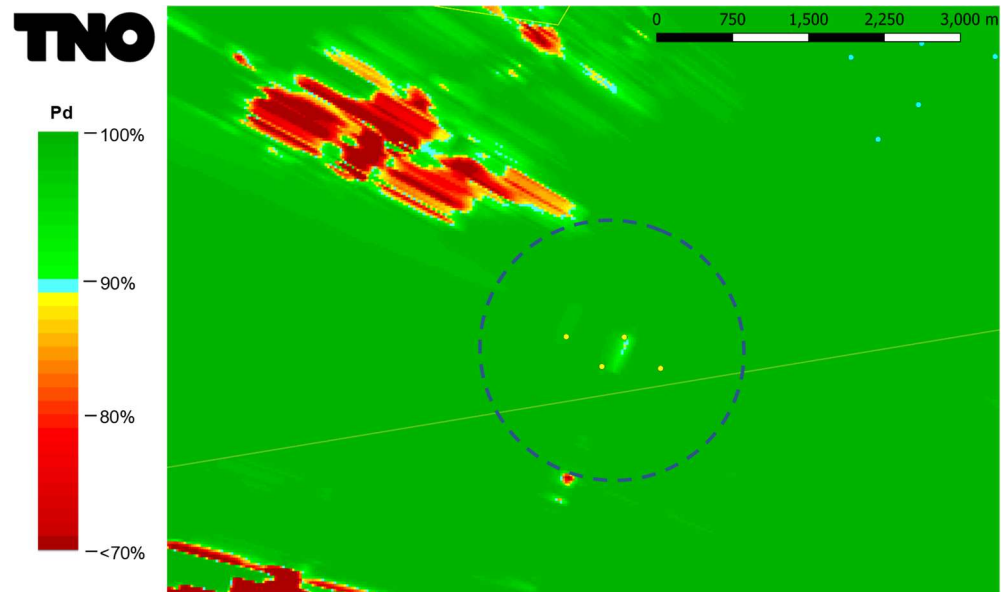


Figure 4.38 Coverage diagram of the standard STAR 2000, including the Wind Farm Filter enhanced processing, zoomed in at the planned position of the new wind turbines for a target at 10000 ft AGL.

#### 4.4 Parallel beam processing

Another potential mitigation is parallel processing of both the high and low beam. In the current STAR 2000 version at Florennes, the radar is equipped with a single receiver. From 0 to typically 8 NM the echoes received via the high beam are used, and for 8 NM to the maximum instrumented range from the low beam. In case of parallel processing both beams have a dedicated receiver, and target detection is performed at both receiver outputs in parallel. The potential improvements are shown in Figure 4.39. The high beam receives less interference from the wind turbines at longer distances, improving detection capability for targets flying at higher altitudes. At smaller distance the improvements are less pronounced. The wind turbine at Chastrès-Walcourt are located at a distance between 7.7 and 8.3 NM. This means that the improved performance for higher flying aircraft is limited. This parallel process technique is believed to be offered as part the STAR NG (Next Generation) programme, but this has not been confirmed by Thales France.

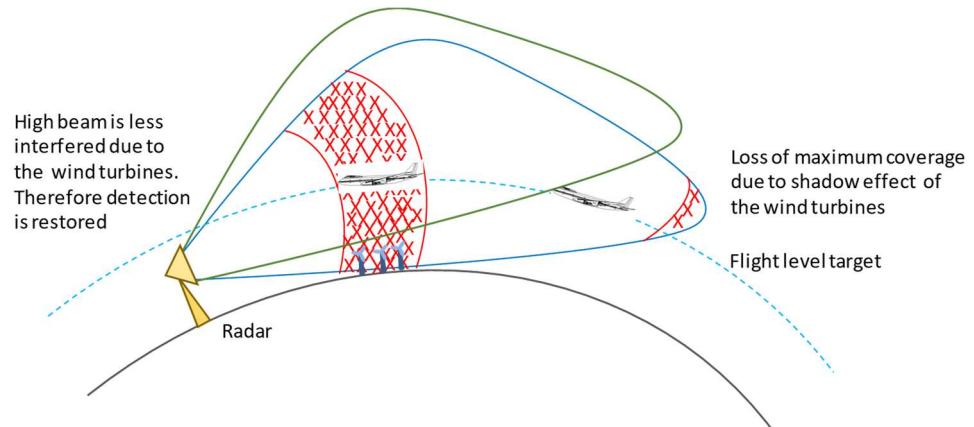


Figure 4.39 Parallel processing of both the high and low beam. The high beam receives less interference from the wind turbines at longer distances, improving detection capability for targets flying at higher altitudes.

#### 4.5 Track continuity

Due to wind turbines interference, loss of detection may occur above a wind farm. In normal situation, when the target is already tracked by the target tracking process, loss of detection during a single antenna scan should not be an issue, the target tracker should be able to cope with this.

PERSEUS calculates the single scan detection probability. In order to translate these results to firm track probability, a spatial averaging is applied to the single scan detection probability results. A spatially averaged detection probability is derived by averaging detection probabilities within a circle with radius 500 m. This specific radius is based on the typical minimum speed of air targets and on the revisiting (scan) time of the antenna, 4 s in this case. Figure 4.40 shows the outcome of spatial averaging for a target height of 1000, 2000, 4000 and 10000 ft AGL, for the standard STAR 2000 and Figure 4.41 for the STAR 2000 including the WFF enhancement. Without the WFF enhancement, the spatially averaged detection probability is low above the wind farm which means that the likelihood of track updates above the wind farm is low even at higher altitudes. Therefore, the probability of track-loss above the wind farm at lower target heights will increase if the target stays over the windfarm for a prolonged time. In this case the number of missed observations (plots) can be high enough for the tracker to declare a track being lost. When the STAR 2000 is equipped with the WFF enhancement which is the case for the SATR 2000 at Florennes, the probability that a track will go lost does not occur, unless the aircraft is flying at 4000 ft AGL lower.

Please note that a combined system is installed at Florennes. Plots from both the PSR and the MSSR are used by the tracking process. An MSSR is typically less affected by a wind farm than a PSR. For targets that travel over the wind farm and that carry a functioning transponder, track degradation will therefore be limited.

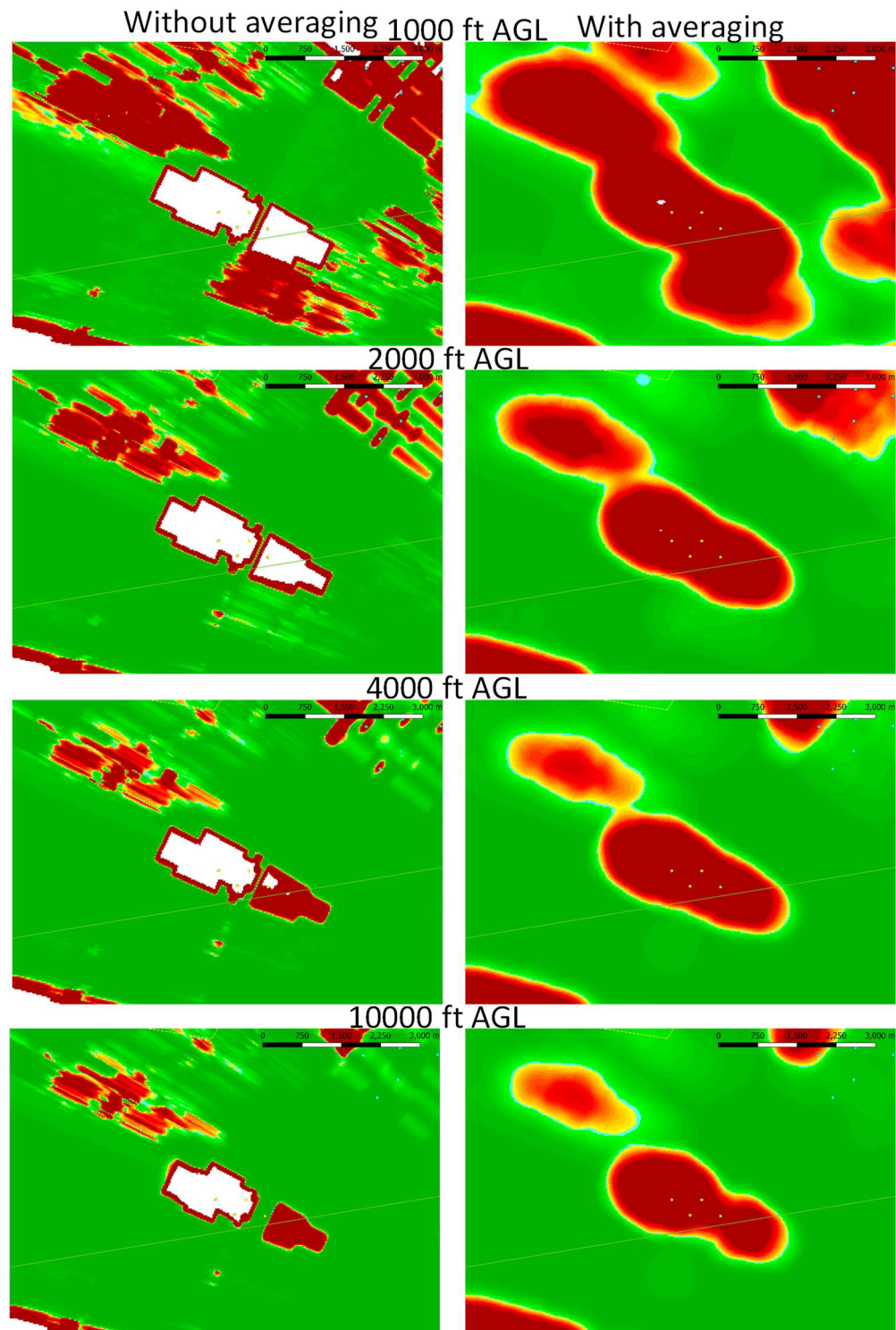


Figure 4.40 The radar detection probability for the standard STAR 2000 for single scan (left) and after spatial averaging with a radius of 500 m.

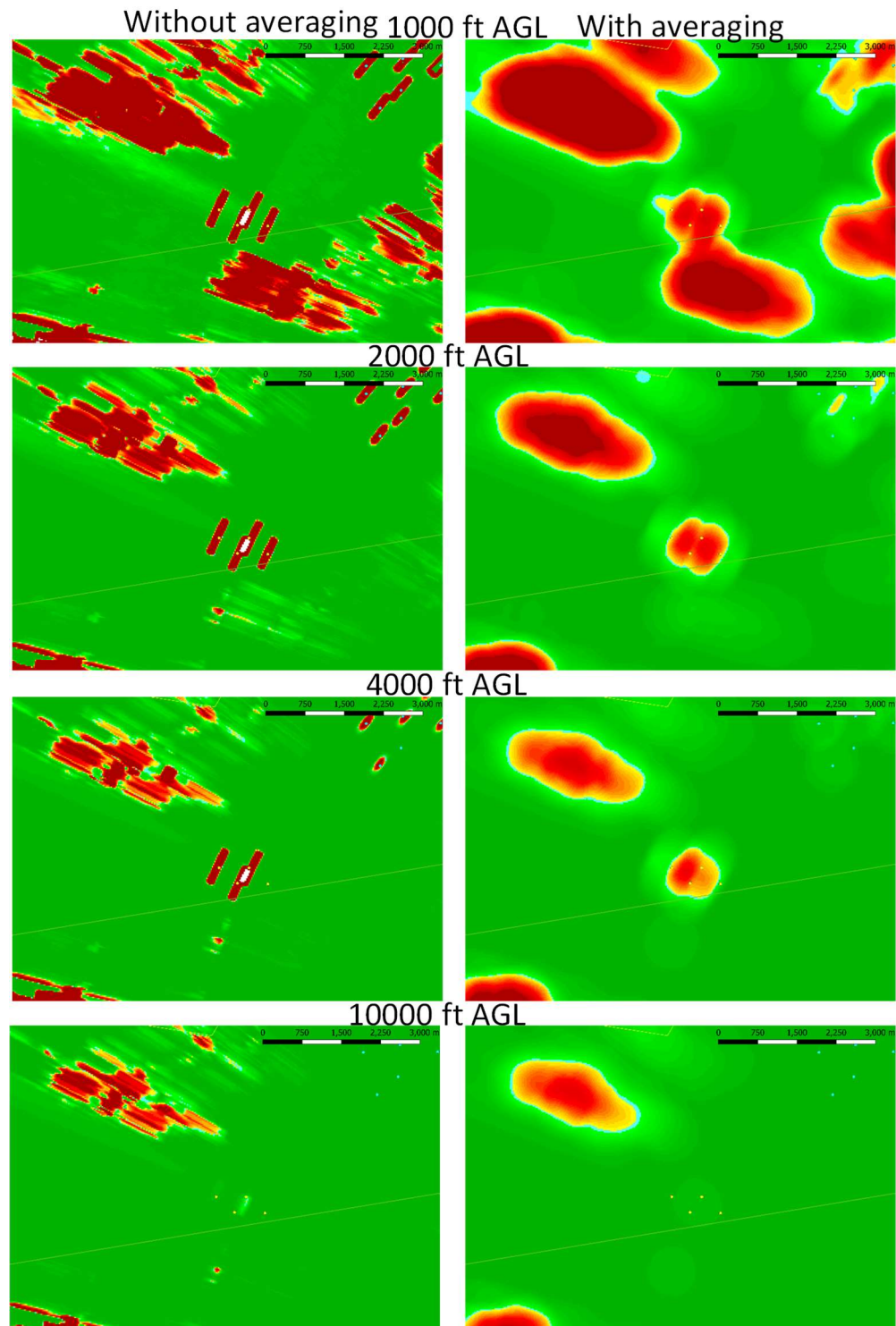


Figure 4.41 The radar detection probability for the STAR 2000, including the WFF enhancement, for single scan (left) and after spatial averaging with a radius of 500 m.

#### 4.6 Wind turbine plots, wind turbine tracks, track seduction

If a PSR can 'see' a wind turbine, or a part of it, (PSR-only) plots may be generated from the wind turbine. Possible consequences of wind turbine plots are the following:

1. A wind turbine plot may be associated with the track of a true target. This phenomenon is referred to as track seduction. As a result, the track of the target may 'break.'
2. A track may originate from a wind turbine contact. In case of a wind farm, tracks that meander from turbine to turbine may arise.
3. A substantial number of contacts that is fed to the tracker during a relatively short time-frame might affect the tracker's ability to handle all incoming plots.

As a mitigation measure the PSR could be equipped with a facility to remove PSR-only-plots that arise within a certain region: range azimuth gating (RAG). Thus, wind turbine plots can, in principle, be removed and they cannot give rise to tracks. At the downside, a plot of a transponder-less target that is above a wind turbine (or farm) at the moment that it is being seen by the radar will be removed as well, which can lead to poor track continuity.

Another facility, that could also be present in the processing of the radar, is track initiation inhibit (TII). This feature forbids the initiation of tracks from plots that are generated within an area specified by the operator. TII eliminates wind turbine tracks but does not eliminate track seduction. Whether this feature is present within the STAR 2000 processing has to be confirmed by Thales.

#### 4.7 False target reports and processing overload

Modern surveillance radars are equipped with multiple mechanism to obtain detections of flying targets only. To suppress reflections at non-moving objects, adaptive cluttermaps are maintained, potentially for each Doppler filter. Non-moving structures, such as the wind turbine mast and the nacelle will therefore not give rise to false (non-target) plots. A flying target will be detected if its response (echo) also passes the so-called CFAR (constant false alarm rate) circuitry. Radar manufacturers have responded to the detection of wind turbine blade flashes, by adapting the logic of the CFAR process. Rather than the CAGO (cell averaging greatest of) logic, ordered statistics (OS) logic is nowadays often applied, since this processing is better capable to detect aircraft when a wind turbine blade flash occurs.

The maximum rotation speed of a wind turbine is assumed to be 30 RPM. Each rotation produces six Doppler flashes, three negative and three positive, when one of the three blades is pointing up- or downwards. This results in a worst case flash frequency of 3 Hz. Given a blade flash frequency of 3 Hz, the 3 dB azimuth beamwidth of 1.4° and the antenna rotation rate of 15 rotation per minute, 0.19 blade flashes per scan are expected from the four additional wind turbines of the windfarm at Chastrès-Walcourt for the PSR Florennes. A worst case assumption, which neglects several wind turbine mitigating features of these radars described above, is that these flashes will result in PSR-only plots. Since modern surveillance radars are capable to process several hundred plots per second, the extra plots are considered as being insignificant. Processing overload is therefore not expected.

## 5 Detailed Engineering Assessment of the MSSR at Florennes

In this section we determine the effect the presence of the wind turbines can have on the performance of the MSSR at Florennes. In order to do this, we first carry out the so-called line-of-sight (LoS) analysis for the MSSR at Florennes. This analysis will give insight into the visibility of the wind farm as seen from the MSSR position.

The analysis takes into account both the curvature of the earth as well as the shape of the terrain. Radio waves do not follow straight lines, but tend to curve along the surface of the earth to some extent as the refractivity index of the air varies with altitude. These refraction effects are generally taken into account by multiplying the radius of the earth by a so-called  $k$ -factor. A common value for the  $k$ -factor is 1.33, which has been used in all results. By using the  $k$ -factor, we can treat the radio waves as if travelling along straight lines instead of curved lines.

In addition to the LoS analysis we also calculate the off-boresight error (OBE) the wind farm causes on the bearing measurements of the secondary radar at Florennes.

### 5.1 Digital Elevation Model

In order to do the line-of-sight analysis, a digital elevation model (DEM) is required. We use the same DEM as used for the primary radar Detailed Engineering Assessment described earlier in this report. As mentioned earlier, the terrain altitude data in the DEM is taken from the Shuttle Radar Topography Mission (SRTM) database. In Figure 5.1 an overview of the terrain altitude is shown. As can be observed, the terrain is hilly. The radar location is shown, as well as the locations of the planned wind turbines. Giving the geometry of the existing and planned wind turbines we have concluded that there are no existing or authorized wind turbines that are in close distance or in the same sector as the newly planned wind turbines that may influence the results. The turbine numbers, corresponding with the numbers in Table 3.1 are also shown.

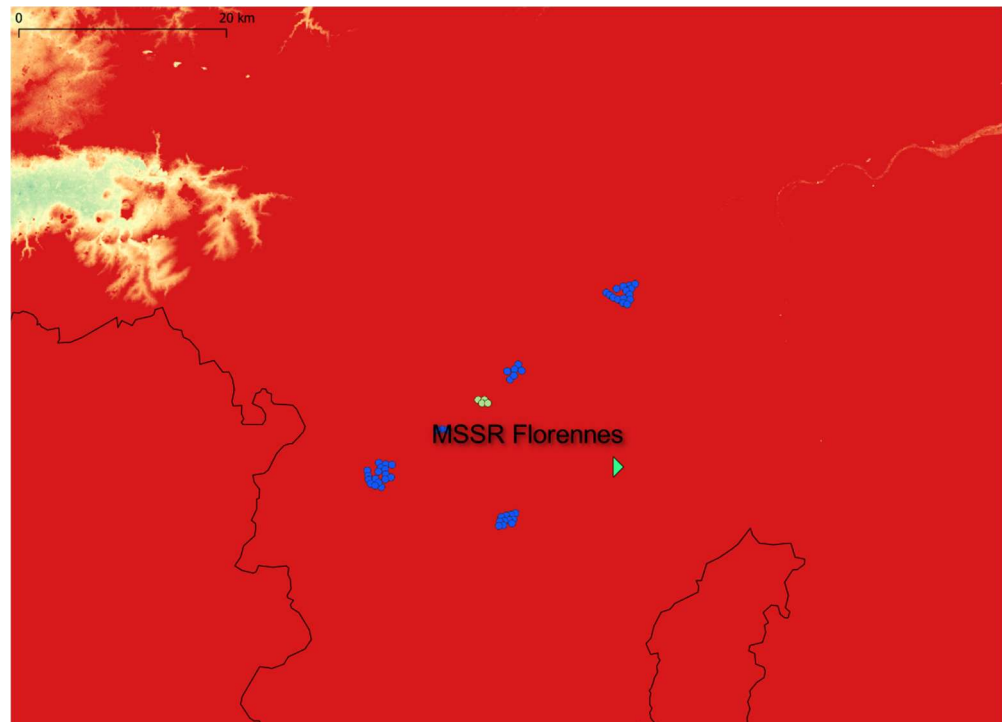


Figure 5.1 Overview of the terrain altitude. The location of the secondary radar is shown, as well as the locations of all existing and authorized wind turbines (blue dots) within a circle of 20 km around the newly planned wind turbines (green dots). The data in this image is taken from the SRTM database and has a resolution of approximately 25 m.

## 5.2 Radar Horizon Florennes

In this section we show the extent of the wind farm in azimuth and elevation for the MSSR. These results reveal if the wind farm has impact on the radar horizon. A wind turbine influences the radar horizon when the elevation angle to the tip height of the wind turbine is larger than the elevation angle to all other objects at the same azimuth angle, extending all the way up to the instrumented range of the secondary surveillance radar (assumed to be up to 256 NM). Given the elevation angle to the tip height, aircraft at different altitudes are influenced at different ranges as shown in Figure 5.2 below.

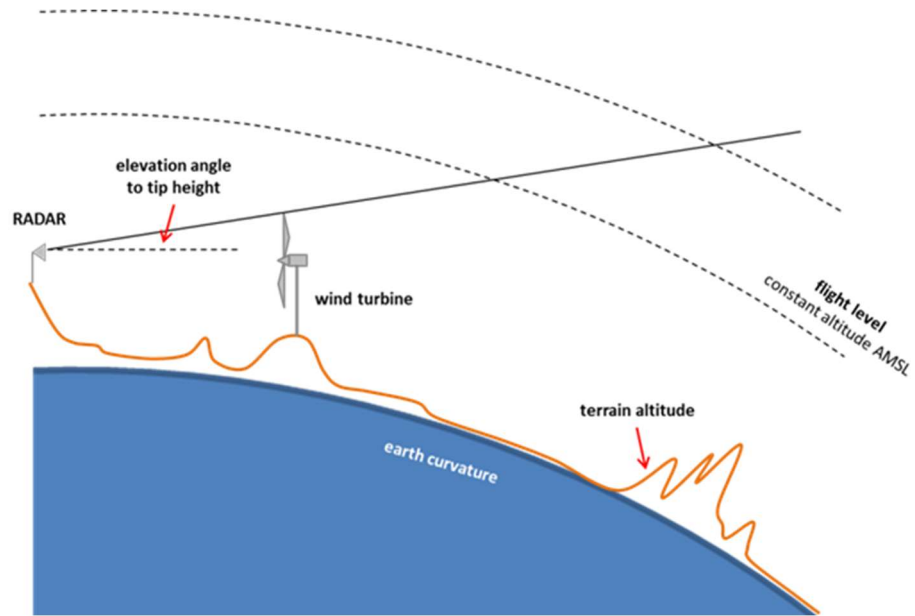


Figure 5.2 Overview of the overall line-of-sight geometry at fixed azimuth. The elevation angle to the tip height of the wind turbine is indicated by a grey line. MSSR replies of aircraft above this line are not influenced by the wind turbine. Aircraft replies below the line may be influenced by the wind turbine.

In the next figure we show azimuth-elevation plots of the surrounding terrain (the radar horizon) including the wind farm. An orange (new) or green (existing and authorised) line indicates the wind turbine up to the tip height. The horizontal red lines indicate the blades of the wind turbine at hub height. Note that the scaling of the horizontal and vertical axes in these figures is different. This means that the wind turbines appear high and narrow. The width of the blades in the horizontal direction (azimuth) is in fact the actual width of the wind turbine as seen from the radar.

As can be seen in Figure 5.3 the radar has line-of-sight to the planned wind turbines. The new turbines are planned within approximately  $6^\circ$  in azimuth in North-West direction, from  $292^\circ$  to  $298^\circ$ . There are no existing or authorized wind turbines with the 20 km circle around the newly planned wind turbines, that in the neighborhood or in the same sector.

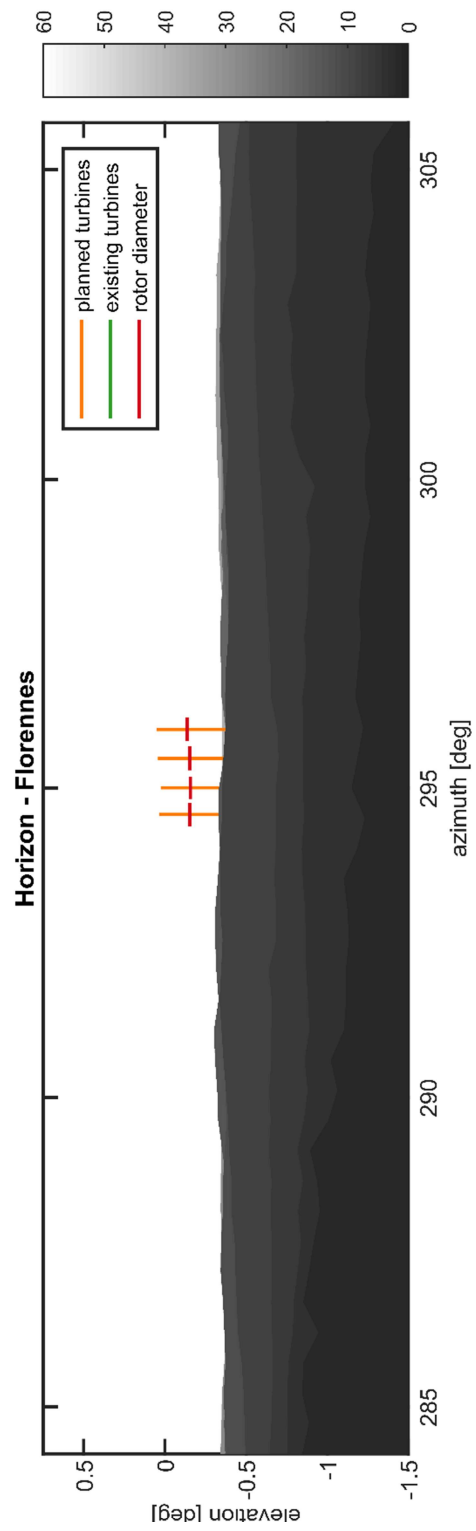


Figure 5.3 Radar horizon in the direction of the wind turbines as seen from the MSSR. There are no existing or authorized wind turbines in the neighborhood.

### 5.3 Line-of-sight to Individual Wind Turbines

Next, we take a look at the line-of-sight to the individual wind turbines as seen from the MSSR. From these figures we can draw conclusions on target ranges and altitudes at which the wind turbine potentially interferes with MSSR operations.

The red line in each figure represents 0 m AMSL. The black line above the red line shows the terrain altitude along the azimuth line towards the wind turbine. The radar is indicated by a red triangle on the left of each figure. The wind turbine is drawn at its particular range in each figure. The first Fresnel zone towards the tip and hub heights of the wind turbine are drawn as dashed red and blue ellipsoids respectively.

A dashed black line passes through the point on the ground with the largest elevation angle as seen from the radar antenna. This is the point that determines the radar horizon in absence of the wind turbine. Furthermore, a red and orange zone are drawn. When orange and red zones are visible, the radar horizon is diminished by the wind turbine. The red zone indicates the reduction of the radar horizon due to the blades of the wind turbine. The orange zone indicates the reduction of the radar horizon by the mast of the wind turbine. In each figure, flight levels at 3000 ft, 5000 ft and 10000 ft are shown as well.

Note that in the red and orange areas the radar is not completely 'blind'. The red and orange colors merely indicate where impact of the wind turbines on the radar performance could occur. In these regions the signal from an SSR transponder towards the antenna at Florennes passes a wind turbine. This means that the wave front of the signal transmitted by the transponder will be disturbed by the wind turbine. This does not necessarily mean that the impact on the position estimation of the target by the MSSR is significantly influenced. The error in the position estimation due to wind turbines placed in the signal path is further investigated in Section 5.5.

Figure 5.4 to Figure 5.7 show the line-of-sight as seen from the Florennes MSSR towards the planned wind turbines New-WT1 to 4.

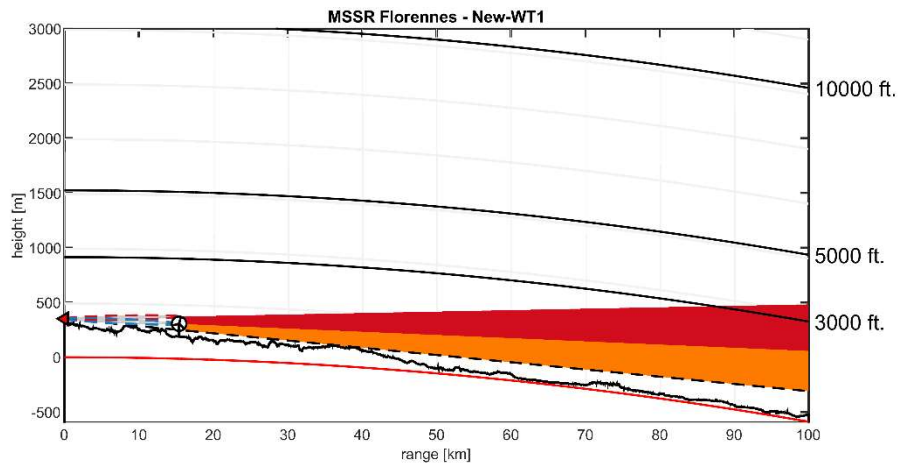


Figure 5.4 Line-of-sight towards planned turbine New-WT1 as seen from the MSSR. The radar has line-of-sight towards the wind turbine. At a range of 100 km, at the azimuth angle towards the wind turbine, a target below 3515 ft might be obscured by the wind turbine. Without the wind turbine this value would be approximately 914 ft. Targets above 3515 ft remain uninfluenced.

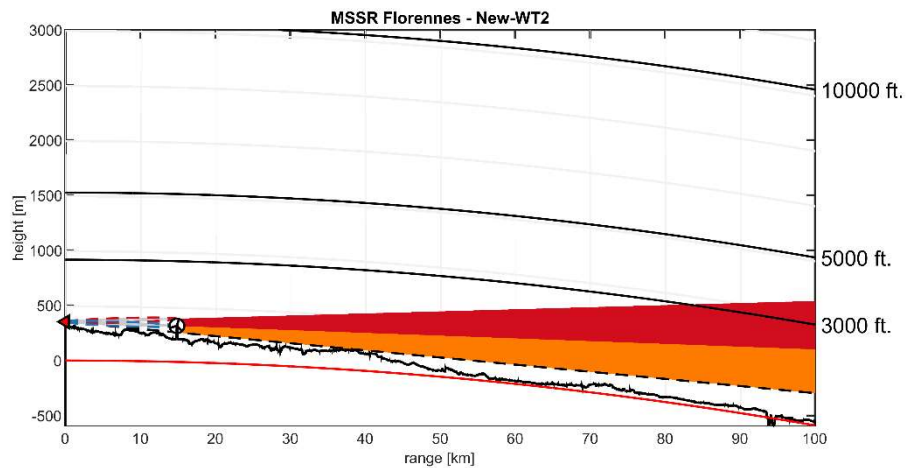


Figure 5.5 Line-of-sight towards planned turbine New-WT2 as seen from the MSSR. The radar has line-of-sight towards the wind turbine. At a range of 100 km, at the azimuth angle towards the wind turbine, a target below 3705 ft might be obscured by the wind turbine. Without the wind turbine this value would be approximately 959 ft. Targets above 3705 ft remain uninfluenced.

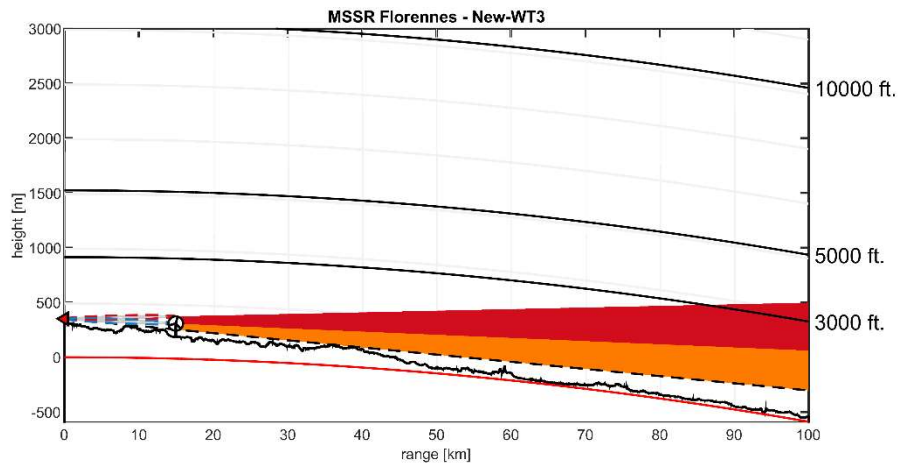


Figure 5.6 Line-of-sight towards planned turbine New-WT3 as seen from the MSSR. The radar has line-of-sight towards the wind turbine. At a range of 100 km, at the azimuth angle towards the wind turbine, a target below 3567 ft might be obscured by the wind turbine. Without the wind turbine this value would be approximately 936 ft. Targets above 3567 ft remain uninfluenced.

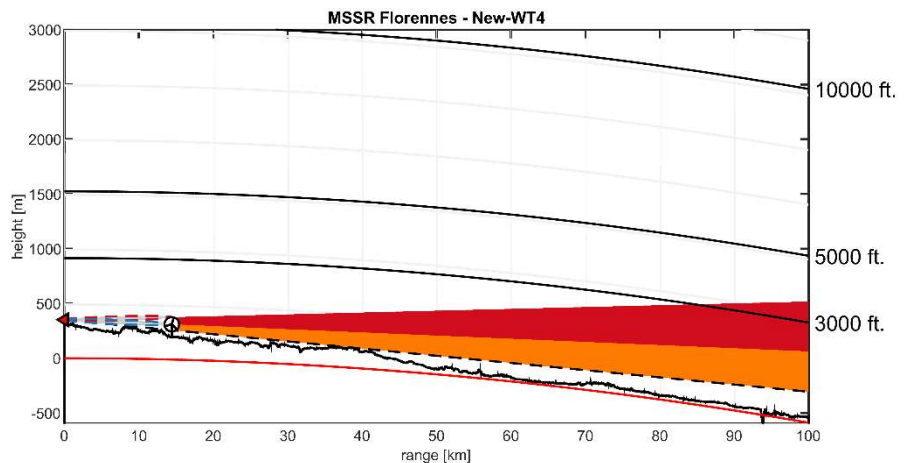


Figure 5.7 Line-of-sight towards planned turbine New-WT4 as seen from the MSSR. The radar has line-of-sight towards the wind turbine. At a range of 100 km, at the azimuth angle towards the wind turbine, a target below 3628 ft might be obscured by the wind turbine. Without the wind turbine this value would be approximately 928 ft. Targets above 3628 ft remain uninfluenced.

## 5.4 Line-of-sight Coverage

The results in the previous sections give insight to which extent the wind farm influences the secondary surveillance radar system at Florennes. In this section we show the locations of the affected areas in the line-of-sight coverage diagrams. Coverage diagrams are shown for targets at altitudes of 3000, 5000 and 10000 ft. A coverage diagram shows whether the performance of the secondary radar can be influenced by the target at a given altitude.

Note that a wind turbine in the line-of-sight path will affect visibility, but not in all cases will it cause the target to be invisible. Radio waves diffract around an

obstacle, limiting the shadow zone directly behind an obstacle. This principle is explained for the PSR in section 2.3 and illustrated in Figure 2.5, but is applicable for the MSSR as well.

The affected azimuth sector of a single wind turbine is taken as 5° on both sides of the wind turbine, 10° in total. As discussed in Section 2.6 in more detail, outside this 5° sector the impact of the wind turbine on the bearing determination will be smaller than the MSSR bearing accuracy.

For each target height two cases are considered: the coverage when there are no turbines present and the coverage for the case the planned turbines are considered. By comparing these figures the effects of the planned turbines on the line-of-sight coverage can be determined.

The line-of-sight coverage diagrams for the co-mounted MSSR at target heights of 3000 ft, 5000 ft and 10000 ft are shown in Figure 5.8 up to Figure 5.10. Areas affected by the mast up to the hub height of the wind turbines are shown in orange. Areas affected from hub height up to the tip height are shown in red.

In the figures it can be observed that the planned wind turbines result in a zone of coverage loss at an azimuth range of approximately 294.6° and 496.0° as seen from the radar.

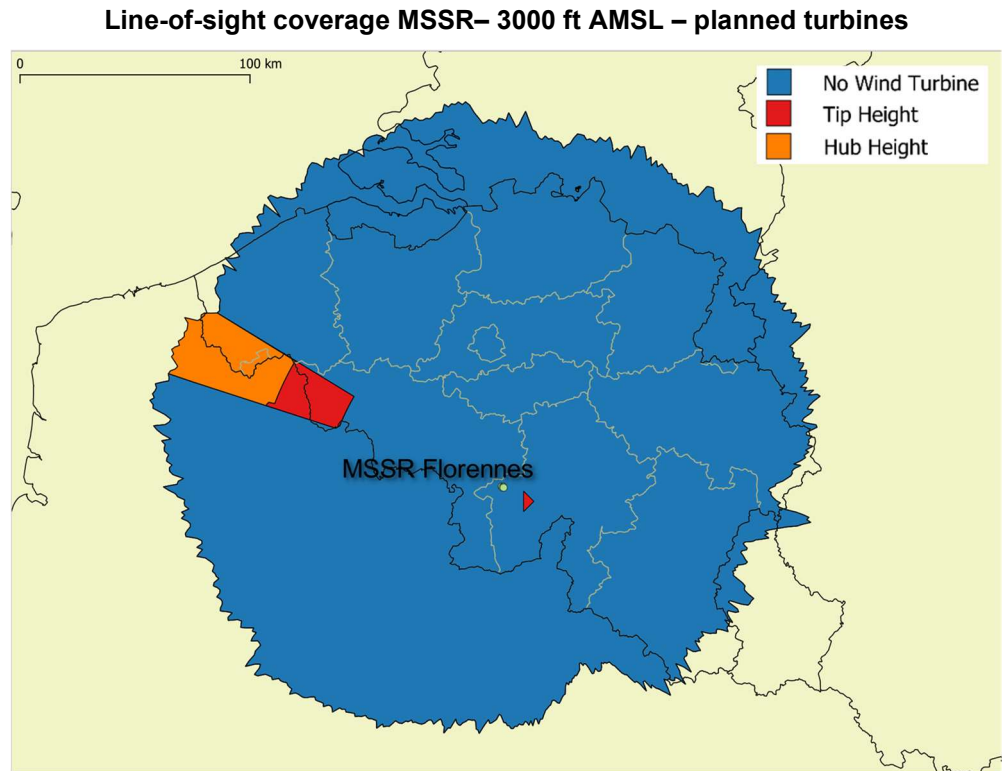


Figure 5.8 Line-of-sight coverage diagram for a target at 3000 ft AMSL as seen from the MSSR. Only the four newly planned turbines are taken into account.

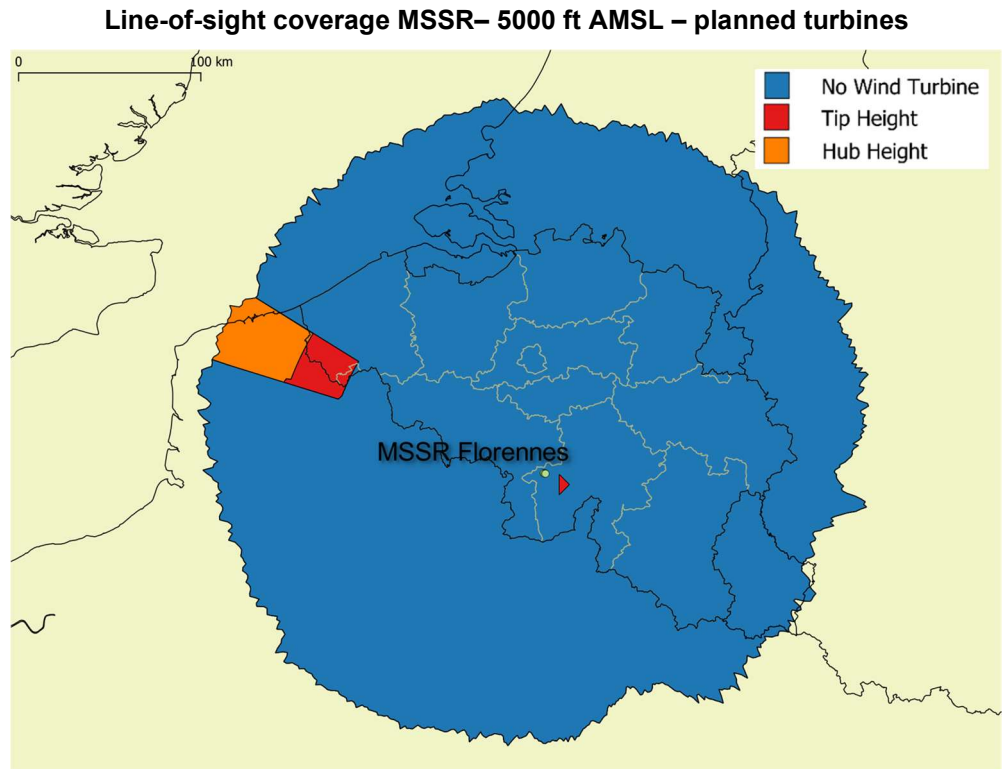


Figure 5.9 Line-of-sight coverage diagram for a target at 5000 ft AMSL as seen from the MSSR. Only the four newly planned turbines are taken into account.

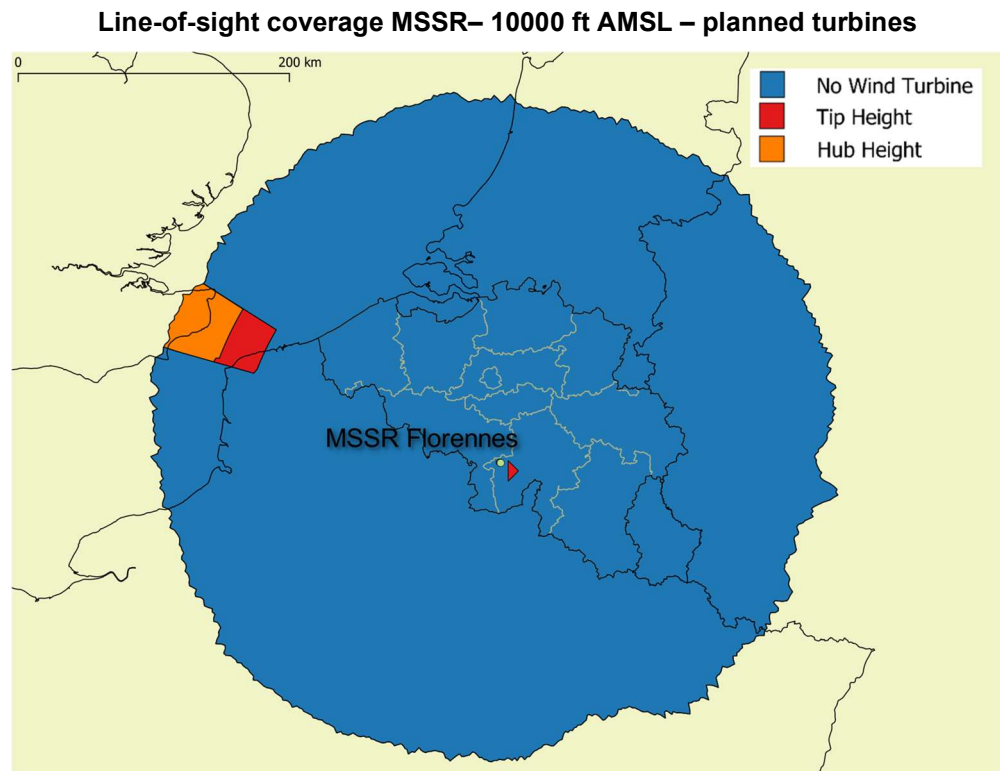


Figure 5.10 Line-of-sight coverage diagram for a target at 10000 ft AMSL as seen from MSSR. Only the four newly planned turbines are taken into account.

## 5.5 Results of the OBE calculations

As stated in section 2.6, the presence of an obstacle (like a mountain, building or wind turbine) between the MSSR antenna and the target can cause an error in the estimation of the bearing to the target. In this section, the extent of this bearing error is calculated using a model developed by TNO, in which the method described section 2.6 has been implemented.

In this section, the OBE calculations are presented for the co-mounted MSSR at Florennes. For the orange and red areas, shown in the many figures in Section 5.4, OBE calculations were carried out. The OBE in the case of the planned wind turbines is determined, which can be compared to the baseline case where the error is introduced by the accuracy of the MSSR and the four closest existing wind turbines. The OBE for each area is presented in two different figures for the planned wind turbines, resulting in a total of four figures.

Note that the OBE calculations are valid for all flight levels shown in the LoS coverage diagrams in the previous section. We only need to do one calculation for all red areas and one for all orange areas.

### 5.5.1 Florennes MSSR – Orange Area

In Figure 5.11, the OBE for the MSSR as a function of azimuth for the orange area in the previous results is presented similar to Figure 2.15, i.e. the area where the errors originate from the mast and the nacelle. As can be seen, the OBE fluctuates quite rapidly with azimuth angle. It therefore makes sense to look at the envelope of the graphs. Also, only the absolute value of the error is interesting. In Figure 5.12

we therefore present the same graphs in a slightly different manner. In these figures, the absolute OBE is grouped per azimuth sector of 1°. For each sector the value of the 50<sup>th</sup>, 90<sup>th</sup> and 100<sup>th</sup> percentile are shown in red, orange and grey, respectively. The standard deviation of the OBE is shown as a black dotted line.

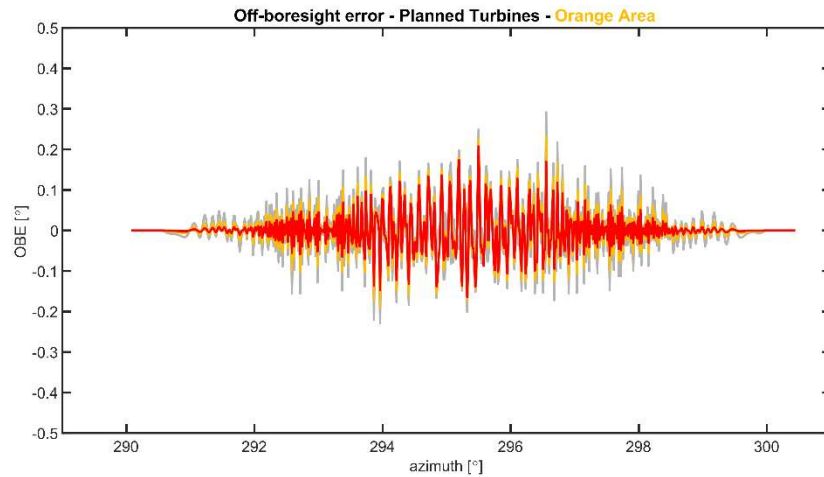


Figure 5.11 The off-boresight error as a function of azimuth for the MSSR, the planned turbines and nearest existing turbines, in the orange areas of the figures shown in Section 5.4, i.e. the area where the errors originate from the mast and nacelle. The maximum absolute error in the orange areas is 0.29°. The azimuth sector influenced by the wind farms ranges from approximately 290.6° to 299.7° as seen from the MSSR.

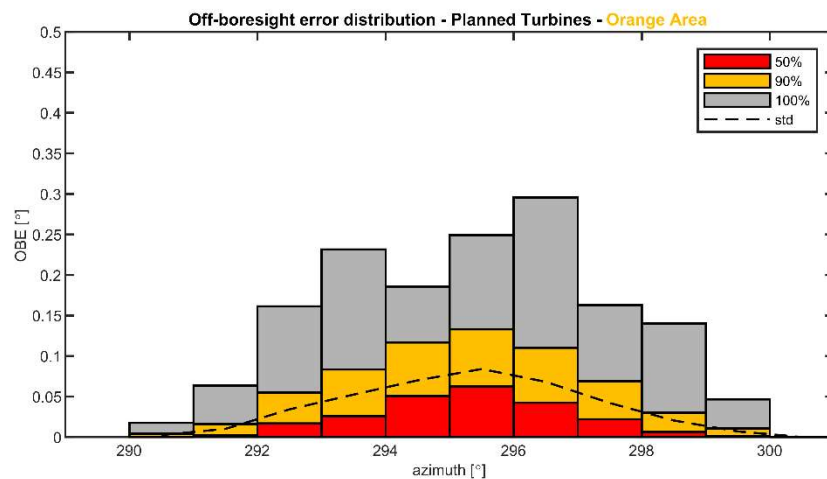


Figure 5.12 The cumulative distribution of the absolute off-boresight error per azimuth sector of 1.0° when the planned and nearest existing turbines are considered. For each azimuth sector the values at the 50<sup>th</sup>, 90<sup>th</sup> and 100<sup>th</sup> percentile are shown, as well as the standard deviation (1  $\sigma$ ) corresponding to a percentile of 68%, assuming a normal distribution of the errors. The maximum OBE in the orange area of 0.29° occurs at an azimuth of 296° - 297°. However, as the 90th percentile indicates, in 90% of the cases,

the OBE in this sector will be less than  $0.11^\circ$ . In 50% of the cases the OBE in this sector is less than  $0.04^\circ$ .

### 5.5.2 Florennes MSSR – Red Area

In Figure 5.13, the OBE for the MSSR as a function of azimuth in red areas is presented, *i.e.*, the area where the errors originate from the blade standing in the upright direction. In Figure 5.14 the absolute OBE is grouped per azimuth sector of  $1^\circ$ .

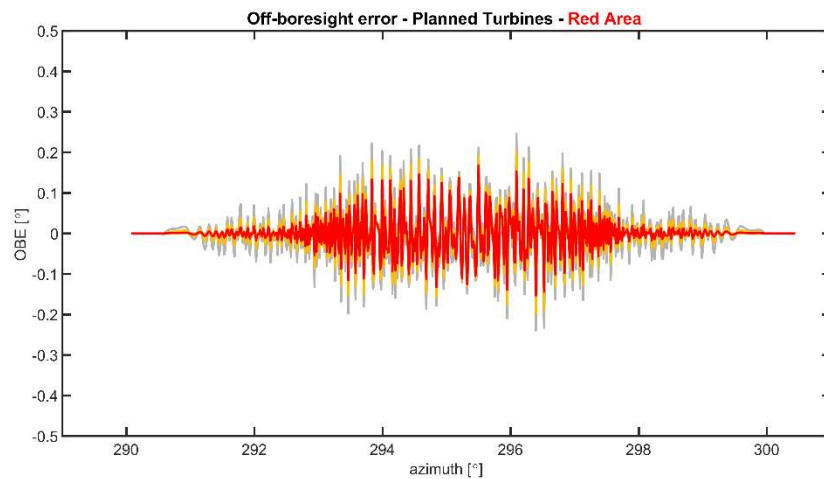


Figure 5.13 The off-boresight error as a function of azimuth for the MSSR, the planned turbines and nearest existing turbines, in the red areas of the figures shown in Section 5.4, *i.e.* the area where the errors originate from the mast and nacelle. The maximum absolute error in the red areas is  $0.25^\circ$ . The azimuth sector influenced by the wind farm ranges from approximately  $290.5^\circ$  to  $299.9^\circ$  as seen from the MSSR.

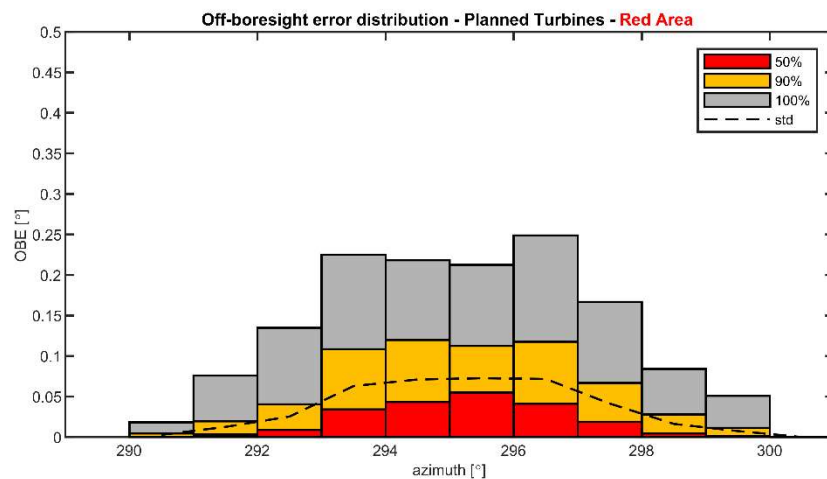


Figure 5.14 The cumulative distribution of the absolute off-boresight error per azimuth sector of  $1.0^\circ$  when the planned and nearest existing turbines are considered. The maximum OBE in the red area of  $0.25^\circ$  occurs at an azimuth of  $296^\circ$  -  $297^\circ$ . However, as the 90th percentile indicates, in 90% of the cases, the OBE in this sector will be less than  $0.12^\circ$ . In 50% of the cases the OBE in this sector is less than  $0.04^\circ$ .

### 5.5.3 Summary of OBE Results

The results of the previous sections are summarized in Table 5.1. The 50<sup>th</sup> and 90<sup>th</sup> percentile, maximum error and standard deviation in the azimuth sectors with the largest maximum OBE are provided for all cases. The maximum error in the orange region measures 0.29°. The maximum error in the red regions measures 0.25° due to the four newly planned wind turbines.

Table 5.1 OBE statistics of the MSSR in the azimuth sector with the largest OBE error.

	50 %	90 %	100 %	$\sigma$	Azimuth Sector (°)
Orange					
Planned	0.04	0.11	0.29	0.07	296 - 297
Red					
Planned	0.04	0.12	0.25	0.07	296 - 297

### 5.5.4 Interpretation of the results

As discussed, there exist many different geometries between the target, obstacle and MSSR antenna. This means that the OBE can be different for two targets at the same azimuth at different moments. We will explain this statistical effect with an example: Looking back at Figure 5.12 the maximum error of the MSSR in the orange area occurs in the azimuth sector from 296° to 297°. In this sector the maximum “grey value”, corresponding to the 100<sup>th</sup> percentile, is 0.25°. The maximum “orange value”, the 90<sup>th</sup> percentile, is 0.12° and the maximum “red value”, 50<sup>th</sup> percentile, is 0.04°. This means that in 100% of the cases, in this specific azimuth sector, the OBE will be smaller than 0.25°, in 90% of the cases it will be smaller than 0.12° and in 50% of the cases it will be smaller than 0.04°. An error between 0.12° and 0.29° will occur in 10% of the cases. For each azimuth sector, the standard deviation is shown as well. For a normal distribution, the standard deviation corresponds to the 68<sup>th</sup> percentile. Here, the error data is not normally distributed. The standard deviation lies between the 50<sup>th</sup> and 90<sup>th</sup> percentile, nonetheless.

Comparing the affected azimuth sector from Figure 5.12 to the horizon shown in Figure 5.3, we see that the azimuth sector with the OBE (290.5° to 299.9° exceeds the sector with the turbines, roughly from 294.6° and 496.0°. We see that the OBE extends up to approximately 4° to the left of the wind farm and to the right overlaps with the OBE due to the existing turbines. Outside this 4° the OBE will not completely disappear, but it will be much smaller than the overall accuracy of the MSSR of 0.05° rms. Outside the 4° the bearing error will therefore be dominated by other error sources than the wind farm. Note that in Section 5.4 a margin of 5° was assumed. Looking at the results of the OBE, this is indeed a reasonable assumption.

To put the errors in perspective, we can express the OBE in an error in cross-range at a certain distance. By cross-range, we mean the direction perpendicular to the viewing direction of the MSSR. We have done this for the three values mentioned above, *i.e.*, 50, 90, 95 and 100% percentile and for distances from the MSSR of 50, 100, 200, 222 and 278 km. The largest values of the OBE statistics when all turbines were taken into account were used. The values are shown below in Table 5.2. As can be seen in the table, an OBE of 0.07° corresponds to an error in cross-range of 122 m at a distance of 100 km.

Table 5.2 Bearing errors converted into cross-range error in meters for various distances from the MSSR.

OBE [°]	Percentile [%]	Azimuth sector [°]	Cross-range error in [m]				
			Range to target				
			50 km 27 NM	100 km 54 NM	200 km 108 NM	222 km 120 NM	278 KM 150 NM
0.04	50	296 - 297	35	70	140	155	194
0.11	90	296 - 297	96	192	384	426	534
0.29	100	296 - 297	253	506	1012	1124	1407

### 5.5.5 *Plot error versus track error*

Finally, we discuss the influence of the off-boresight errors presented in this chapter on the information presented to the operator.

The errors calculated here represent the bearing error on a single reply of the transponder. A worst-case assumption is that the measurement error of a single reply is also the measurement error of the plot. In case a plot is derived from multiple replies per dwell, which is generally the case, the measurement error of the plot will be less than the measurement error of a single reply. A tracker processes plot messages and presents track updates of targets on a computer screen to the operator. In general, the error in a plot is also not the same as the error in a track update. Especially when a target does not maneuver, positional errors in plots will be 'smoothed' by the track algorithm.

## 6 Simple Engineering Analysis

Using the information given in Chapter 2, we have carried out a line-of-sight analysis. In Figure 3.1 we show the terrain profile in the area containing the wind turbines and radars. The lines in the figure connect the radar to outermost newly planned wind turbines. By studying the terrain profile along this line for each wind turbine, we can determine whether the radar in Bertem, Saint-Hubert, Liège and Zaventem will have line-of-sight to the windfarm.

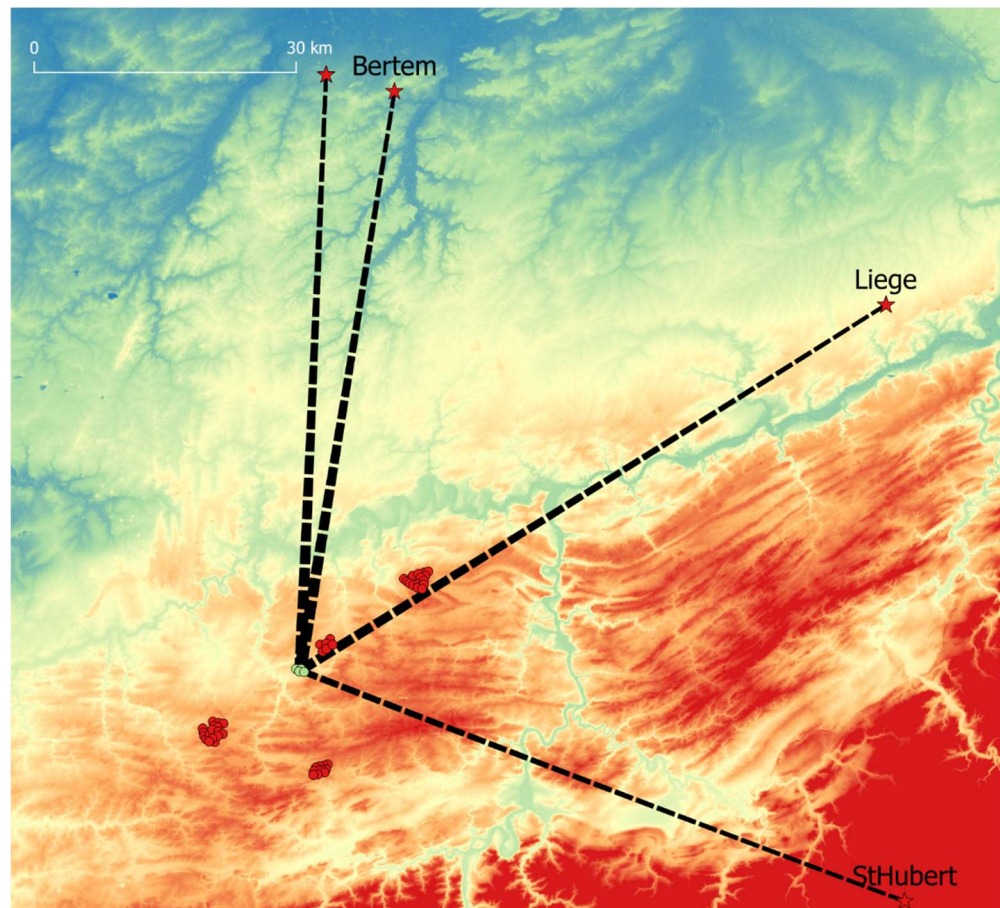


Figure 6.1 The altitude of the terrain between the involved radars and the newly planned wind turbine taken from the SRTM database. The line-of-sight analysis is performed by studying the terrain profile on the line connecting the radar and each wind turbine.

So-called ‘standard propagation’ is assumed when determining the line-of-sight. This is modelled by multiplying the earth radius by a factor of  $4/3$  (the “k-factor”).

In the figures on the next pages, the red ellipses show the first Fresnel zone from the radar antenna to the tip height of the wind turbine and the blue ellipses show the first Fresnel zones from the radar antenna to the hub height of the wind turbines. These ellipses are referred to as the  $\frac{1}{4} \lambda$  Fresnel zone, where  $\lambda$  refers to the radar wavelength. Signals travelling between the terminals within the blue and red ellipses are at most  $90^\circ$  out of phase with respect to the signal that takes the

shortest path. The black lines show the profile of the ground level between the radar and wind turbine as derived from the SRTM database<sup>1</sup>.

## 6.1 Line of Sight Analysis PSR Bertem

### 6.1.1 Newly Planned Turbines

Figure 6.2 to Figure 6.5 show line-of-sight diagrams between the location of the radar system and the newly planned wind turbine locations. The horizontal range is range over ground in kilometres calculated using Vincenty's formulae. The turbines are located approximately 67 km from the PSR at Bertem.

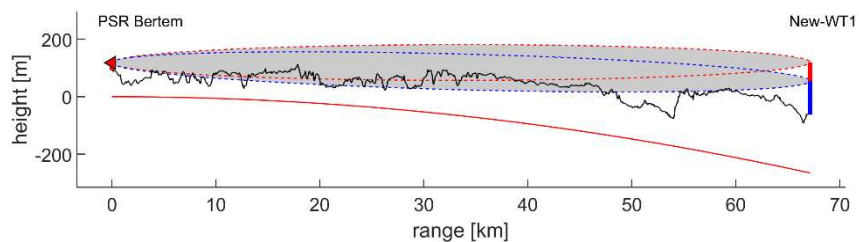


Figure 6.2 Line-of-sight between the PSR of Bertem and New-WT1. The distance from the radar to the wind turbine measures 67.1 km.

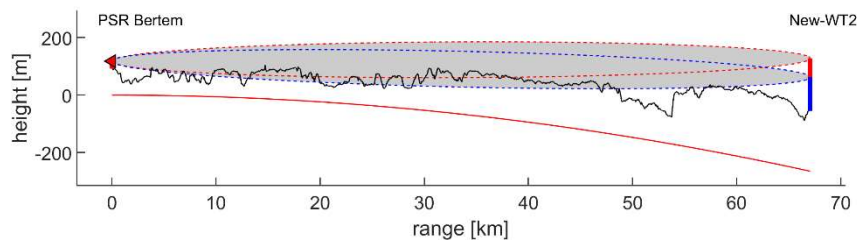


Figure 6.3 Line-of-sight between the PSR of Bertem and New-WT2. The distance from the radar to the wind turbine measures 67.4 km.

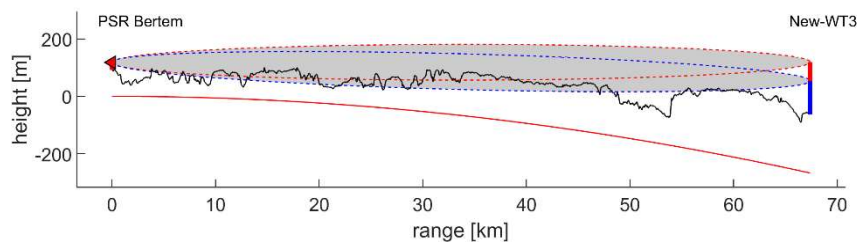


Figure 6.4 Line-of-sight between the PSR of Bertem and New-WT3. The distance from the radar to the wind turbine measures 67.4 km.

<sup>1</sup> For the line-of-sight analysis the data from the Shuttle Radar Topography Mission (SRTM1) is used. This database contains terrain altitude information with respect to the EGM96 geoid. The database was determined by NASA using high-resolution radar carried on the Space Shuttle. The SRTM data has a resolution of 1 arcseconds, which corresponds to a horizontal resolution of about ~20 m at 51 degrees latitude.

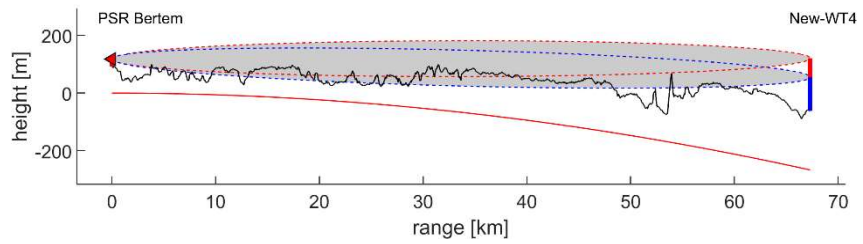


Figure 6.5 Line-of-sight between the PSR of Bertem and New-WT4. The distance from the radar to the wind turbine measures 67.3 km.

The Fresnel zones are only partly obstructed by the terrain profile, meaning that the radar antenna has line-of-sight to the newly planned wind turbines.

### 6.1.2 Existing and authorized turbines

Because the number of existing, authorized and pending turbines is large, not all line-of-sight figures for these turbines are presented. After investigation of the different line of sights to the PSR at Bertem it is determined that two windfarm are close in range or in azimuth. These are windfarm Walcourt (WT1-WT6) and windfarm Fontenelle (WT51-WT53). Figure 6.6 to Figure 6.8 show the corresponding line-of-sight plot for WT2 and WT3 and WT52 with are the closest in azimuth. As can be observed from the figures the Fresnel zones are not fully obstructed by the terrain profile, meaning that the radar antenna has line-of-sight to the wind turbines.

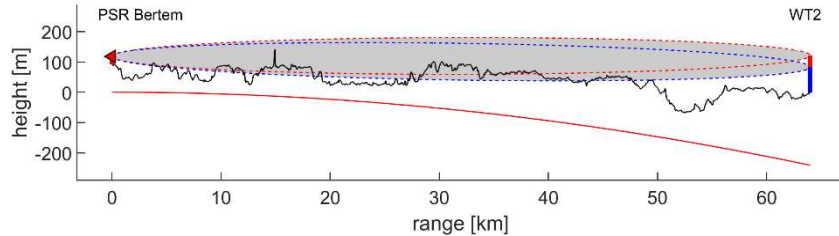


Figure 6.6 Line-of-sight between the PSR of Bertem and WT2. The distance from the radar to the wind turbine measures 64.0 km.

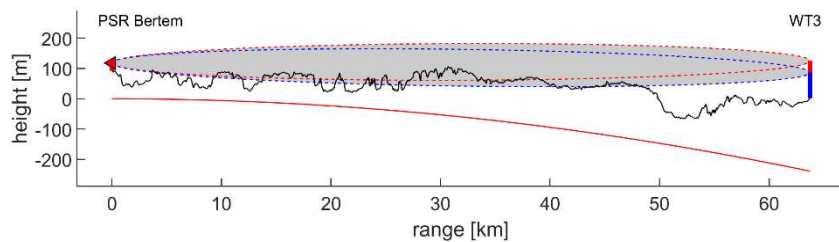


Figure 6.7 Line-of-sight between the PSR of Bertem and WT3. The distance from the radar to the wind turbine measures 70.5 km.

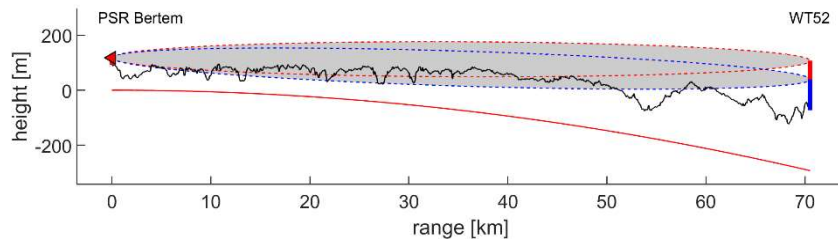


Figure 6.8 Line-of-sight between the PSR of Bertem and WT52. The distance from the radar to the wind turbine measures 61.0 km.

## 6.2 Line of Sight Analysis PSR Saint-Hubert

### 6.2.1 Newly Planned Turbines

Figure 6.9 to Figure 6.12 show line-of-sight diagrams between the location of the radar system and the newly planned wind turbine locations. The horizontal range is range over ground in kilometres calculated using Vincenty’s formulae. The turbines are located approximately 74 km from the PSR at Saint-Hubert.

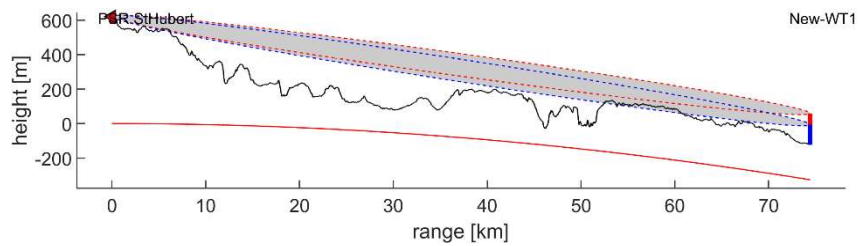


Figure 6.9 Line-of-sight between the PSR of Saint-Hubert and New-WT1. The distance from the radar to the wind turbine measures 74.4 km.

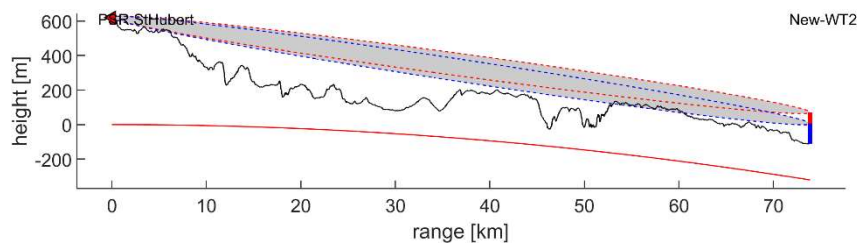


Figure 6.10 Line-of-sight between the PSR of Saint-Hubert and New-WT2. The distance from the radar to the wind turbine measures 73.9 km.

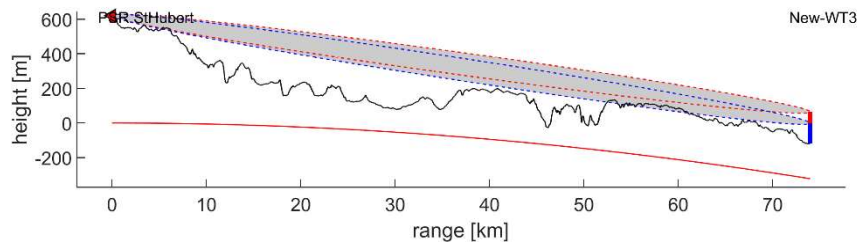


Figure 6.11 Line-of-sight between the PSR of Saint-Hubert and New-WT3. The distance from the radar to the wind turbine measures 74.0 km.

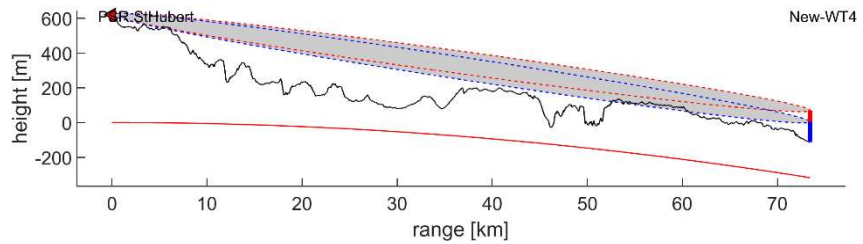


Figure 6.12 Line-of-sight between the PSR of Saint-Hubert and New-WT4. The distance from the radar to the wind turbine measures 73.4 km.

The Fresnel zones are only partly obstructed by the terrain profile, meaning that the radar antenna has line-of-sight to the newly planned wind turbines.

### 6.2.2 Existing and authorized turbines

Because the number of existing, authorized and pending turbines is large, not all line-of-sight figures for these turbines are presented. After investigation of the different line of sights to the PSR at Saint-Hubert it is determined that two windfarm are close in range or in azimuth. These are windfarm Walcourt (WT1-WT6) and windfarm Fontenelle (WT51-WT53). Figure 6.13 to Figure 6.15 show the corresponding line-of-sight plot for WT2 and WT3 and WT52 with are the closest in azimuth. As can be observed from the figures the Fresnel zones are not fully obstructed by the terrain profile, meaning that the radar antenna has line-of-sight to the wind turbines.

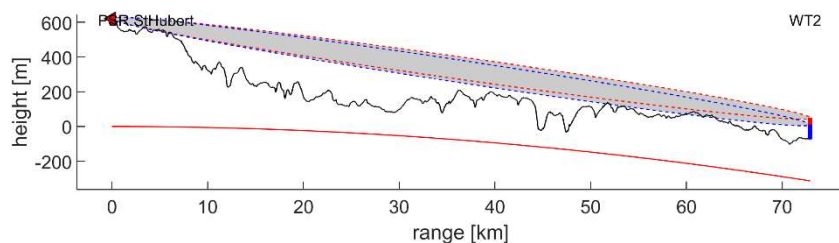


Figure 6.13 Line-of-sight between the PSR of Saint-Hubert and WT2. The distance from the radar to the wind turbine measures 72.9 km.

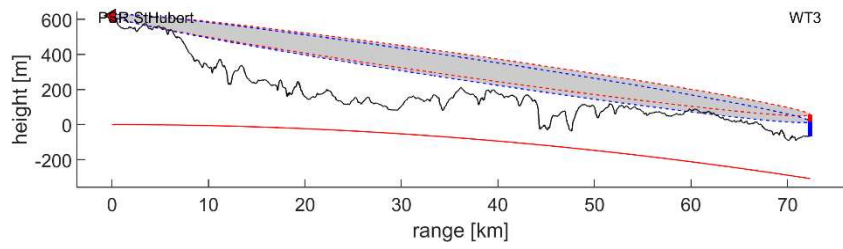


Figure 6.14 Line-of-sight between the PSR of Saint-Hubert and WT3. The distance from the radar to the wind turbine measures 72.3 km.

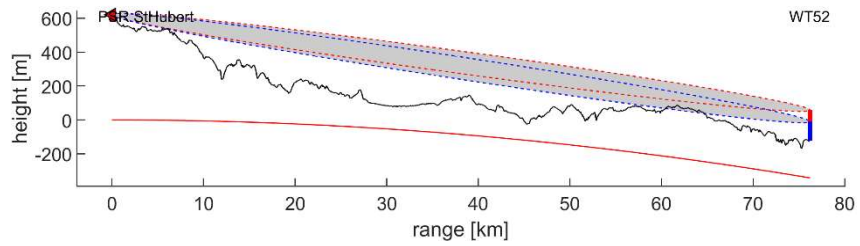


Figure 6.15 Line-of-sight between the PSR of Saint-Hubert and WT52. The distance from the radar to the wind turbine measures 76.3 km.

### 6.3 Line of Sight Analysis PSR Liège

#### 6.3.1 Newly Planned Turbines

Figure 6.16 to Figure 6.19 show line-of-sight diagrams between the location of the radar system and the newly planned wind turbine locations. The horizontal range is range over ground in kilometres calculated using Vincenty's formulae. The turbines are located approximately 79 km from the PSR at Liège.

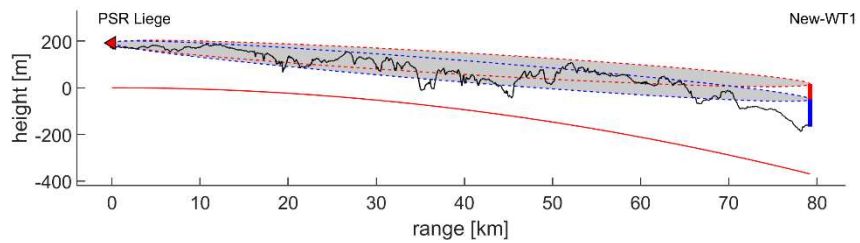


Figure 6.16 Line-of-sight between the PSR of Liège and New-WT1. The distance from the radar to the wind turbine measures 79.2 km.

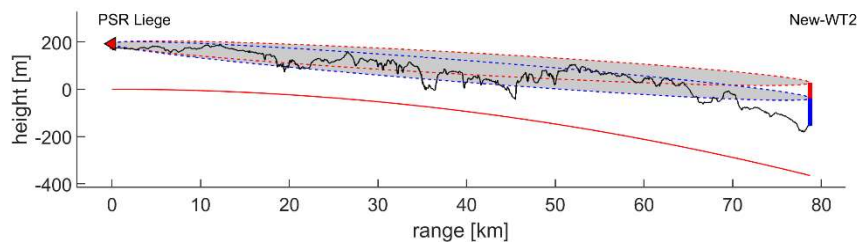


Figure 6.17 Line-of-sight between the PSR of Liège and New-WT2. The distance from the radar to the wind turbine measures 78.7 km.

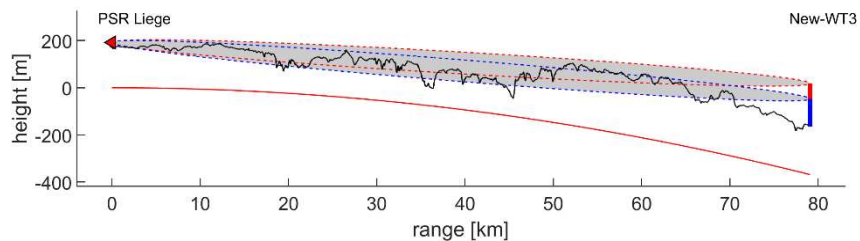


Figure 6.18 Line-of-sight between the PSR of Liège and New-WT3. The distance from the radar to the wind turbine measures 79.1 km.

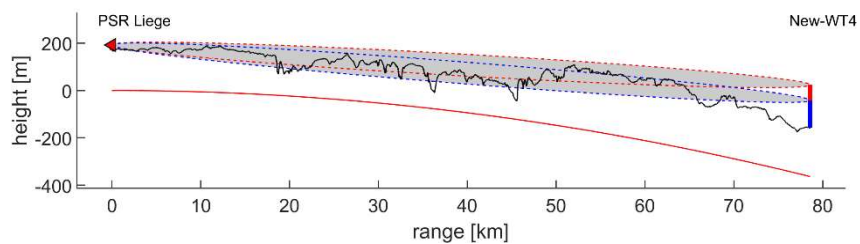


Figure 6.19 Line-of-sight between the PSR of Liège and New-WT4. The distance from the radar to the wind turbine measures 78.6 km.

The Fresnel zones are not fully obstructed by the terrain profile, meaning that the radar antenna has line-of-sight to the newly planned wind turbines.

### 6.3.2 Existing and authorized turbines

Because the number of existing, authorized and pending turbines is large, not all line-of-sight figures for these turbines are presented. After investigation of the different line of sights to the PSR at Saint-Hubert it is determined that two windfarm are close in range or in azimuth. These are windfarm Walcourt (WT1-WT6), windfarm Beaumont (Froidchapelle) (WT33-WT49) and windfarm Fontenelle (WT51-WT53). Figure 6.20 to Figure 6.24 show the corresponding line-of-sight plot for WT4 and WT5, WT33 and WT44 and WT50 with are the closest in azimuth. As can be observed from the figures the Fresnel zones are not fully obstructed by the terrain profile, meaning that the radar antenna has line-of-sight to the wind turbines. There are however two exception showed in Figure 6.22 and Figure 6.23, showing the line of sight of two wind turbines of windfarm Beaumont (Froidchapelle). The Fresnel zones are fully blocked meaning this windfarm will be invisible for the radar at Liège.

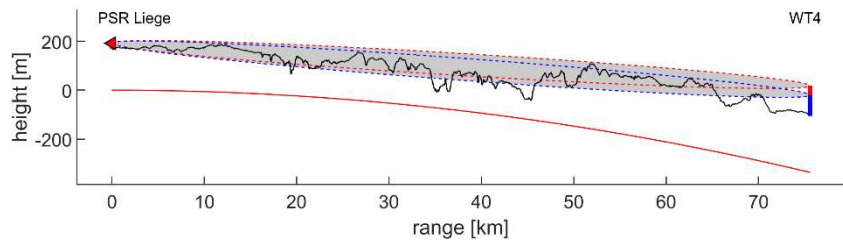


Figure 6.20 Line-of-sight between the PSR of Liège and WT4. The distance from the radar to the wind turbine measures 75.6 km.

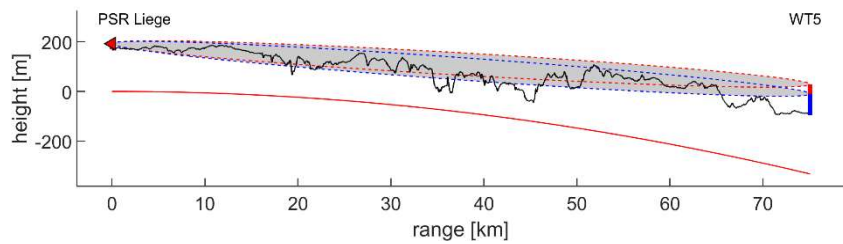


Figure 6.21 Line-of-sight between the PSR of Liège and WT5. The distance from the radar to the wind turbine measures 75.1 km.

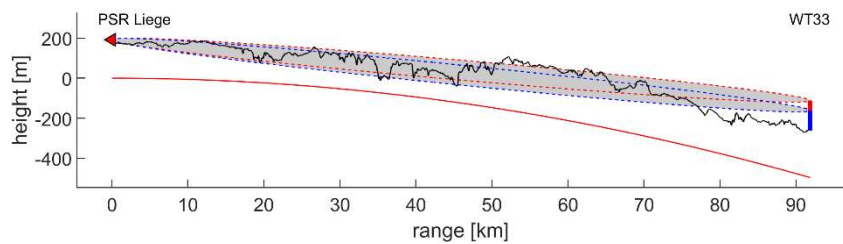


Figure 6.22 Line-of-sight between the PSR of Liège and WT33. The distance from the radar to the wind turbine measures 91.9 km. The Fresnel zones are fully blocked meaning this windfarm will be invisible for the radar at Liège.

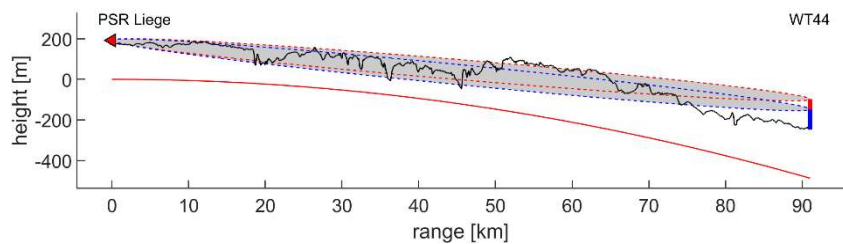


Figure 6.23 Line-of-sight between the PSR of Liège and WT44. The distance from the radar to the wind turbine measures 91.0 km. The Fresnel zones are fully blocked meaning this windfarm will be invisible for the radar at Liège.

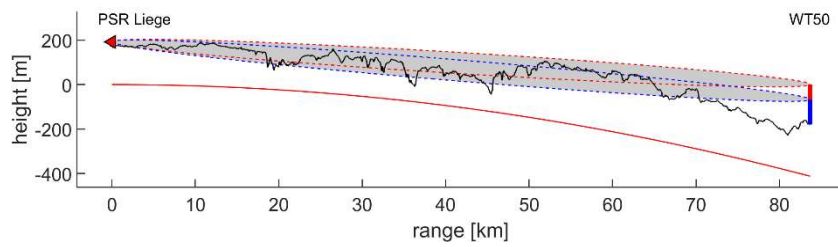


Figure 6.24 Line-of-sight between the PSR of Liège and WT50. The distance from the radar to the wind turbine measures 83.7 km.

## 6.4 Line of Sight Analysis PSR Zaventem

### 6.4.1 Newly Planned Turbines

Figure 6.25 to Figure 6.28 show line-of-sight diagrams between the location of the radar system and the newly planned wind turbine locations. The horizontal range is range over ground in kilometres calculated using Vincenty's formulae. The turbines are located approximately 68 km from the PSR at Zaventem.

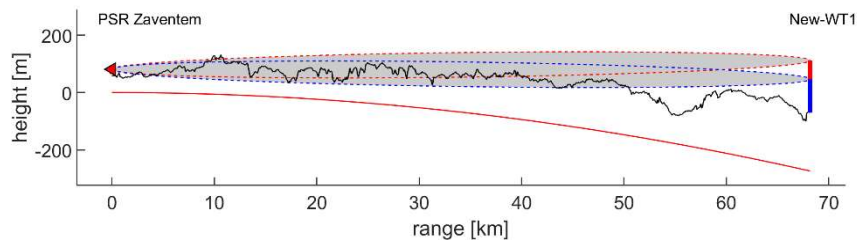


Figure 6.25 Line-of-sight between the PSR of Zaventem and New-WT1. The distance from the radar to the wind turbine measures 68.2 km.

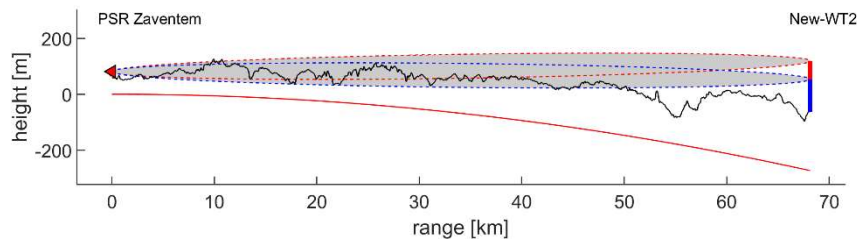


Figure 6.26 Line-of-sight between the PSR of Zaventem and New-WT2. The distance from the radar to the wind turbine measures 68.1 km.

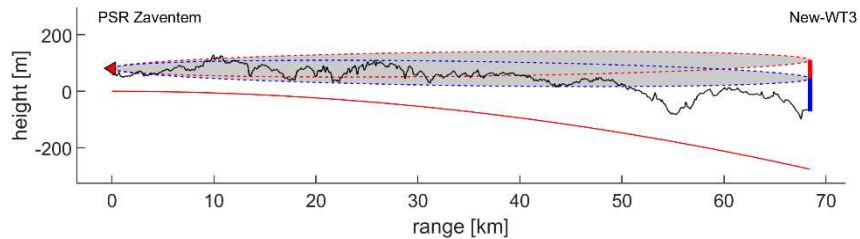


Figure 6.27 Line-of-sight between the PSR of Zaventem and New-WT3. The distance from the radar to the wind turbine measures 68.4 km.

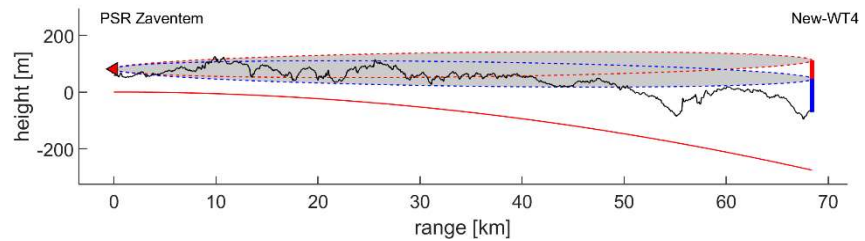


Figure 6.28 Line-of-sight between the PSR of Zaventem and New-WT4. The distance from the radar to the wind turbine measures 68.4 km.

The Fresnel zones are fully obstructed by the terrain profile, meaning that the radar has no line-of-sight to the planned wind turbine.

## 6.5 Eurocontrol Guidelines

As demonstrated in Section 6.1 to 6.4 there is line-of-sight between the newly planned wind turbines of the windfarm at Chastrès-Walcourt and the primary radar at Bertem, Saint Hubert and Liège and no line-of-sight at Zaventem. When there is line-of-sight the wind turbines can affect the radar in a number of ways. The EUROCONTROL guidelines [1] prescribe that in the case of a simple engineering assessment, the size of the following two regions must be determined:

1. The shadow region behind the wind turbine, caused by the attenuation due to the wind turbine being an obstacle for the electromagnetic field.
2. The volume located above and around the wind turbine in which the radar detection threshold, generally implemented with CFAR (Constant False Alarm Rate) logic, is affected.

Both regions are shown in Figure 6.29 below. This image was taken from [1], Section 4.3.1. In the next sections the sizes of the two regions are determined.

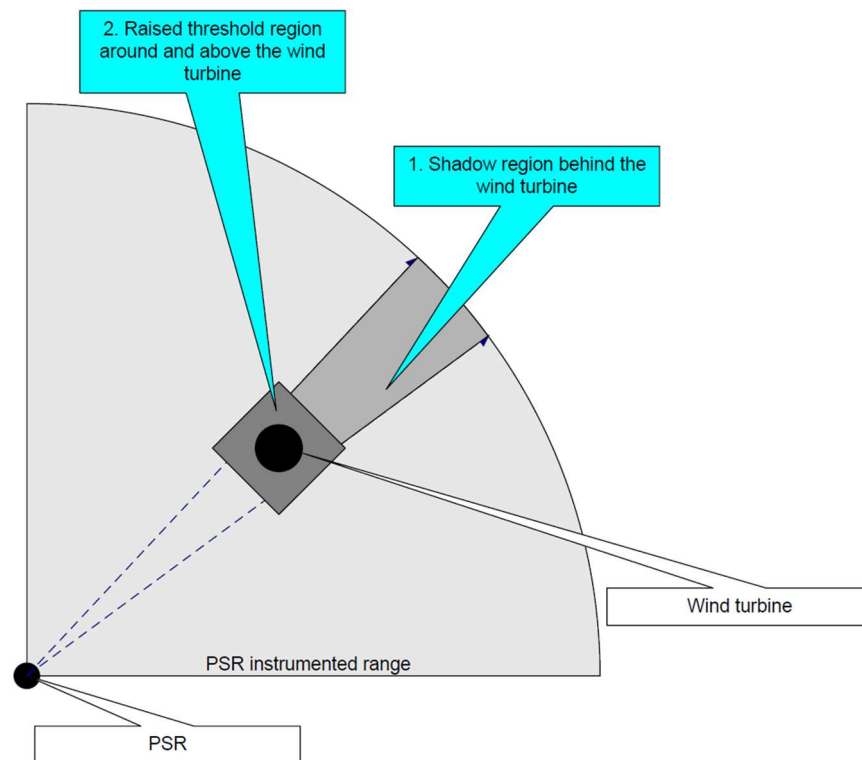


Figure 6.29 Schematic representation of the shadow region behind a wind turbine (1) and the raised threshold region around and above a wind turbine. Image taken from [1].

## 6.6 Region 1: Shadow region

In this section we determine the size of the shadow regions behind the wind turbine. In Figure 6.30 the shape of the region is shown.

The shadow region extends all the way to the instrumented range of the radar. The length of the shadow region is therefore equal to the instrumented range minus the distance from the radar to the wind turbine.

The width of the shadow region is given by  $2\sqrt{(\lambda D)}$ , where  $\lambda$  is the radar wavelength and  $D$  the distance from the wind turbine. See also Annex A-3 in the EUROCONTROL guidelines [1]. The width is at its maximum at the instrumented range from the radar.

Finally, the height of the shadow region can be calculated according to Equation 1 in Annex A-2 in [1]. Note that this calculation takes the curvature of the earth into account by assuming a spherical earth with radius  $kR_e$ , where  $R_e$  is the earth radius and  $k$  is the standard propagation k-factor equal to  $4/3$ . The calculated height is relative to the EGM96 geoid, which is approximately equal to mean sea level and is accurate within several meters. The height of the shadow region is equal to the tip height at the location of the wind turbine and increases (not taking the ground level into account) to its maximum value at instrumented range from the radar.

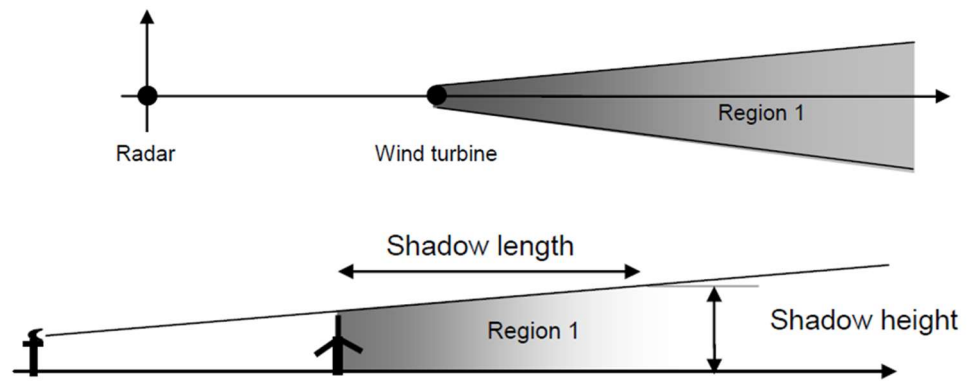


Figure 6.30 Shape of the shadow region. Image taken from Annex A-1 in [1].

#### 6.6.1 Shadow Locations PSR Bertem

The shadows of all turbines for PSR Bertem are shown in Figure 6.31 and Figure 6.32. The shadows of the existing and authorized turbines are indicated with black, the shadows of the new turbines are indicated with a red colour. It can be observed that the shadows of the planned turbines do not overlap with the shadows of the existing turbines.



Figure 6.31 The geographic locations of the shadow regions of only the new turbines as seen from the PSR in Bertem. The shadow regions (small red regions) extend from the wind turbine to the instrumented range (110 NM or 204 km) of the radar (indicated with a red circle).

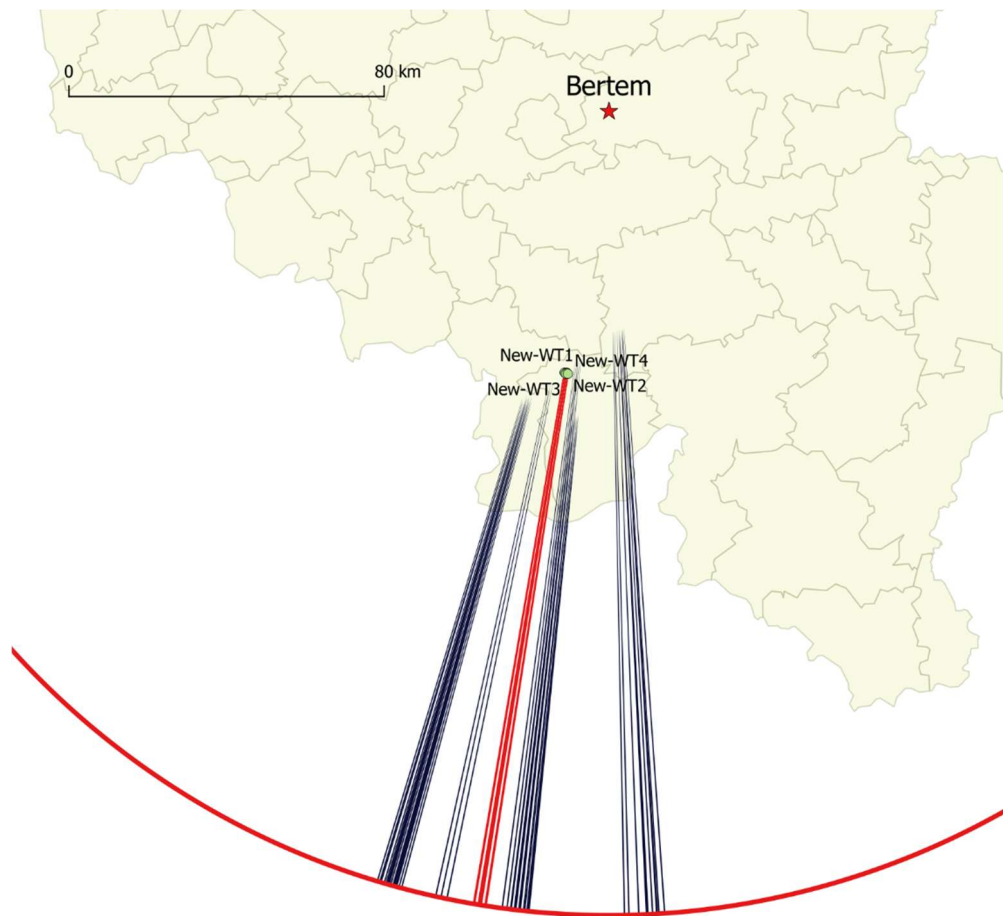


Figure 6.32 The geographic locations of the shadow regions of the new turbines as seen from the PSR in Bertem. The shadow regions of the planned (small red regions) and existing, authorized and pending turbines (small black regions) extend from the wind turbine to the instrumented range (110 NM or 204 km) of the radar (indicated with a red circle).

6.6.2 Shadow Dimensions PSR Bertem

Length, maximum width and maximum height of the shadow regions for the newly planned turbines are provided in Table 6.1.

Table 6.1 Dimensions of the shadow regions of the four planned wind turbines.

Nr.	ID	Tip Height [m]	Shadow PSR Bertem		
			Length [km]	Max. height w.r.t. sea level [km]	Max. Width [m]
53	New-WT1	182.5	136.81	2.574	355.249
54	New-WT2	182.5	136.91	2.597	355.379
55	New-WT3	182.5	136.59	2.571	354.963
56	New-WT4	182.5	136.67	2.576	355.067

### 6.6.3 Shadow Locations PSR Saint-Hubert

The shadows of all turbines for PSR Saint-Hubert are shown in Figure 6.33 and Figure 6.34. The shadows of the existing and authorized turbines are indicated with black, the shadows of the new turbines are indicated with a red colour. It can be observed that the shadows of the planned turbines do not overlap with the shadows of the existing turbines.

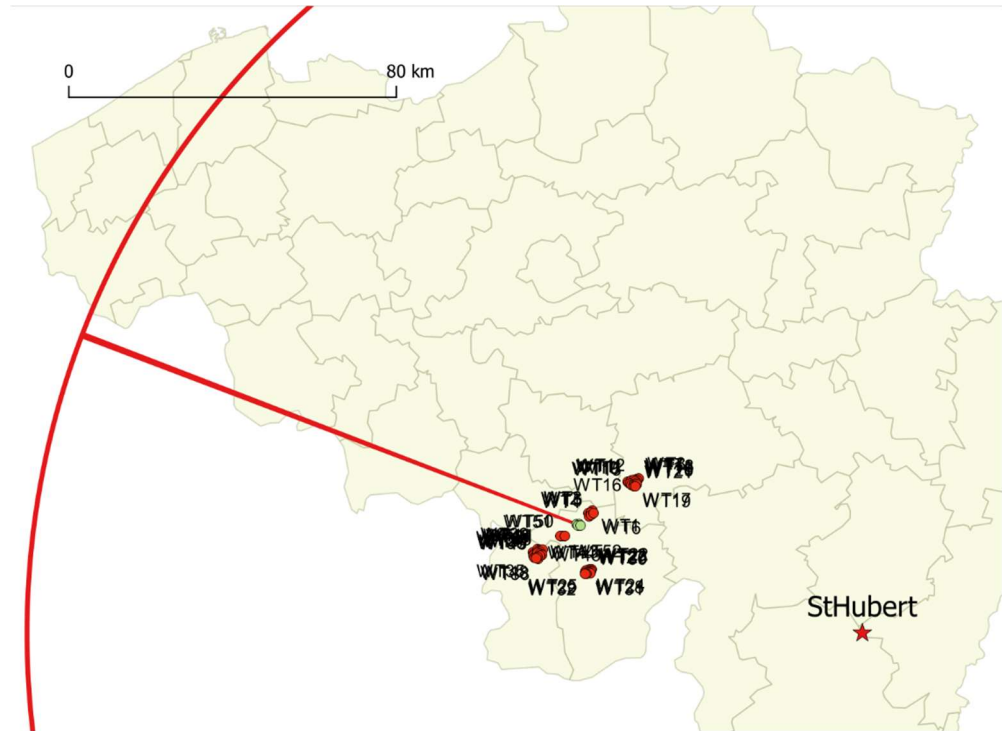


Figure 6.33 The geographic locations of the shadow regions of only the new turbines as seen from the PSR in Saint-Hubert. The shadow regions (small red regions) extend from the wind turbine to the instrumented range (110 NM or 204 km) of the radar (indicated with a red circle).

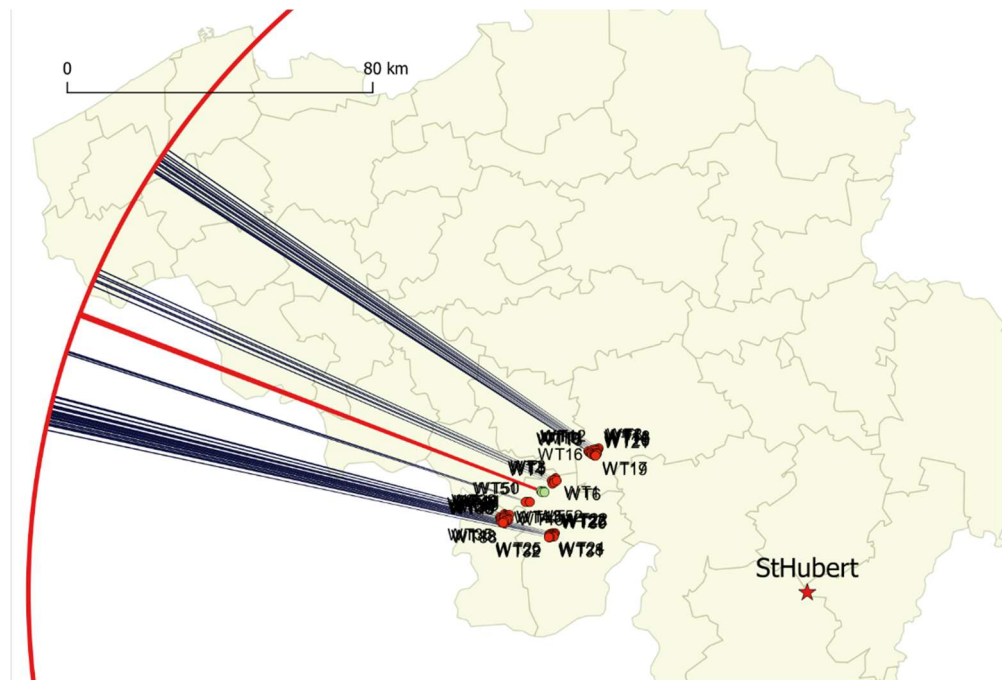


Figure 6.34 The geographic locations of the shadow regions of the new turbines as seen from the PSR in Saint-Hubert. The shadow regions of the planned (small red regions) and existing, authorized and pending turbines (small black regions) extend from the wind turbine to the instrumented range (110 NM or 204 km) of the radar (indicated with a red circle).

6.6.4 *Shadow Dimensions PSR Saint-Hubert*

Length, maximum width and maximum height of the shadow regions for the newly planned turbines are provided in Table 6.2.

Table 6.2 Dimensions of the shadow regions of the four planned wind turbines.

Nr.	ID	Tip Height [m]	Shadow PSR Bertem		
			Length [km]	Max. height w.r.t. sea level [km]	Max. Width [m]
61	New-WT1	150	129.38	1.531	345.468
62	New-WT2	150	129.91	1.552	346.175
63	New-WT3	150	129.81	1.535	346.042
64	New-WT4	150	130.36	1.540	346.774

6.6.5 *Shadow Locations PSR Liège*

The shadows of all turbines for PSR Liège are shown in Figure 6.35 and Figure 6.36. The shadows of the existing and authorized turbines are indicated with black, the shadows of the new turbines are indicated with a red colour. As demonstrated in section 6.3.2 there is no line of sight between the windfarm Beaumont (Froidchapelle) (WT33-WT49) and the radar at Liège. Therefore the shadowline for these turbines are not drawn.

In Figure 6.37 it can be observed that the shadows of the new turbines partly overlap with the shadows of the existing turbines.

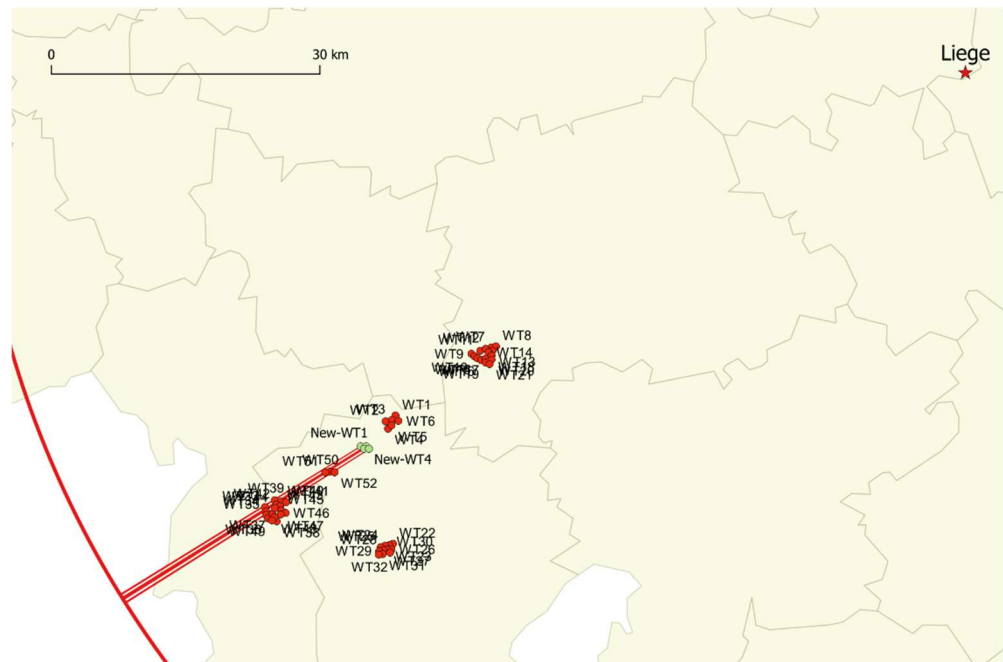


Figure 6.35 The geographic locations of the shadow regions of only the new turbines as seen from the PSR in Liège. The shadow regions (small red regions) extend from the wind turbine to the instrumented range (60 NM or 111 km) of the radar (indicated with a red circle).

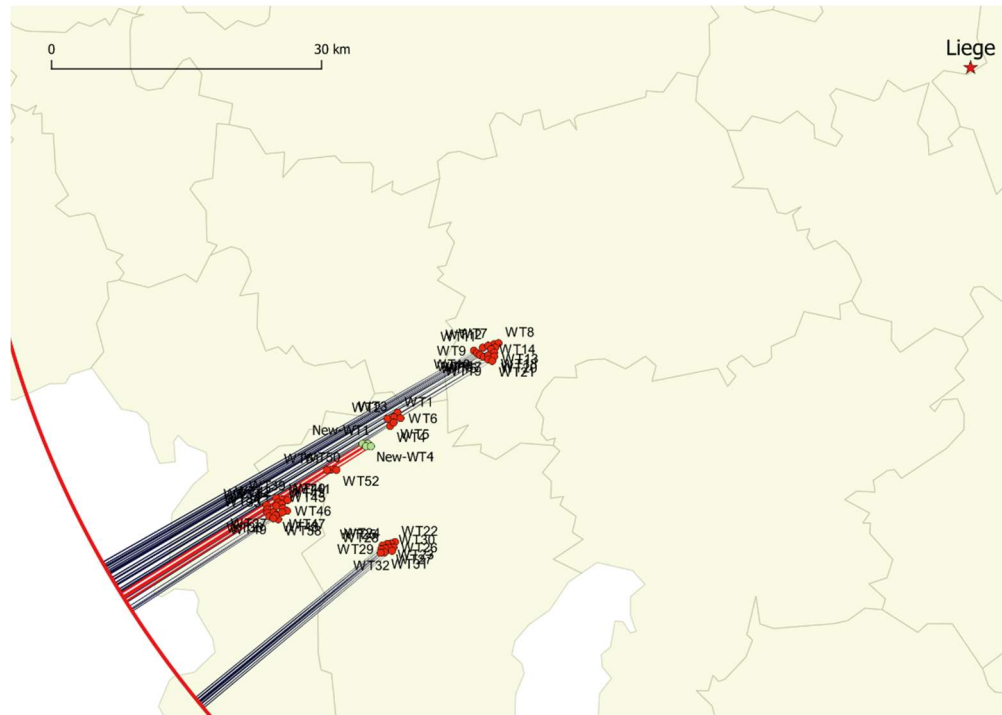


Figure 6.36 The geographic locations of the shadow regions of the new turbines as seen from the PSR in Liège. The shadow regions (small red regions) extend from the wind turbine to the instrumented range (60 NM or 111 km) of the radar (indicated with a red circle).

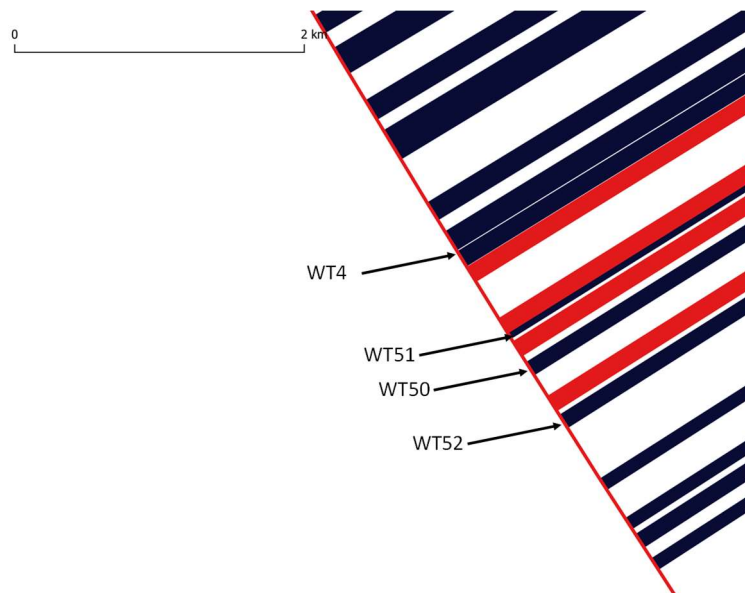


Figure 6.37 The geographic locations of the shadow regions close to the shadows of the new wind turbines at the instrumented range of the radar.

6.6.6 *Shadow Dimensions PSR Liège*

Length, maximum width and maximum height of the shadow regions for existing and authorised wind turbines are provided in Table 6.3 and for the newly planned turbines in Table 6.4.

Table 6.3 Dimensions of the shadow regions of the existing and authorised wind turbines to close or overlapping with the newly planned wind turbines.

Nr.	ID	Tip Height [m]	Shadow PSR Liège		
			Length [km]	Max. height w.r.t. sea level [km]	Max. Width [m]
4	WT4	123.5	35.23	0.660	123.387
50	WT50	180	27.13	0.662	108.278
51	WT51	180	26.69	0.648	107.396
52	WT52	180	27.56	0.649	109.132

Table 6.4 Dimensions of the shadow regions of the four planned wind turbines.

Nr.	ID	Tip Height [m]	Shadow PSR Liège		
			Length [km]	Max. height w.r.t. sea level [km]	Max. Width [m]
53	New-WT1	182.5	31.58	0.669	116.821
54	New-WT2	182.5	32.07	0.684	117.724
55	New-WT3	182.5	31.73	0.672	117.098
56	New-WT4	182.5	32.22	0.678	117.999

## 6.7 Region 2: Raised threshold regions

The second region of potential impact is the so-called raised threshold region. In this region the possibly large reflection of the wind turbine raises the detector threshold of the radar, lowering the probability of detection of a target.

The size of the region in range is dependent on the exact implementation of the CFAR detection logic in the radar. In general a radar threshold is determined using a number of range cells around the Cell Under Test (CUT).

### 6.7.1 Raised threshold regions PSR Bertem

In the case of AEG SRE-M5 PSR at Bertem (see Table 3.8) the number of range cells around the cell under test has been specified to be 32. In addition, the 4 closest range cells, the so-called guard cells, are neglected. Given the size of a range cell of 30 m, we calculate that a wind turbine can potentially influence the radar threshold from approximately 1080 m in front until 1080 m behind the wind turbine. The size in azimuth is dependent on the horizontal beam width of the radar. Given the beam width in Table 3.8, at a range of 25 km the size in azimuth is approximately 480 m.

The region in which the wind turbine influences the threshold has been calculated for 2 combinations of wind turbines and radars:

1. The existing and authorized turbines that are closest in range from the planned wind turbines.

2. All mentioned in 1. and the newly planned wind turbines.

The results are presented in Figure 6.38 and Figure 6.39. There is no overlap between the regions of the existing and newly planned wind turbines. The affected area due to the new wind turbines is 8.54 km<sup>2</sup> for PSR Bertem.

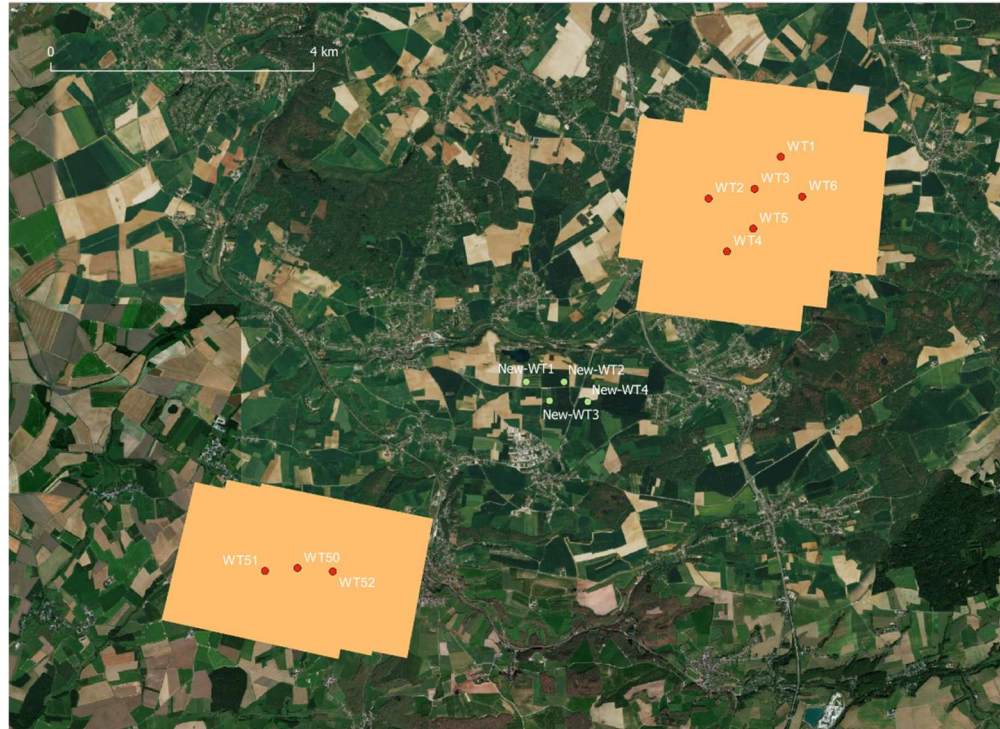


Figure 6.38 The raised threshold regions (indicated with the orange regions) for the existing and authorized turbines closest to the newly planned turbines for PSR Bertem.



Figure 6.39 The raised threshold regions (indicated with the orange regions) for the existing and authorized turbines and the newly planned turbines (green regions) for PSR Berthem.

#### 6.7.2 *Raised threshold regions PSR Saint-Hubert*

In the case of AEG SRE-M5 PSR at Saint-Hubert (see Table 3.9) the number of range cells around the cell under test has been specified to be 32. In addition, the 4 closest range cells, the so-called guard cells, are neglected. Given the size of a range cell of 30 m, we calculate that a wind turbine can potentially influence the radar threshold from approximately 1080 m in front until 1080 m behind the wind turbine. The size in azimuth is dependent on the horizontal beam width of the radar. Given the beam width in Table 3.9, at a range of 25 km the size in azimuth is approximately 480 m.

The region in which the wind turbine influences the threshold has been calculated for 2 combinations of wind turbines and radars:

1. The existing and authorized turbines that are closest in range from the planned wind turbines.
2. All mentioned in 1. and the newly planned wind turbines.

The results are presented in Figure 6.40 and Figure 6.43. There is overlap between the regions of the existing and newly planned wind turbines. The affected area due to the new wind turbines is 9.70 km<sup>2</sup> for PSR Saint-Hubert and overlaps with 0.03 km<sup>2</sup> affected area of the existing and authorized turbines.



Figure 6.40 The raised threshold regions (indicated with the orange regions) for the existing and authorized turbines closest to the newly planned turbines for PSR Saint-Hubert.



Figure 6.41 The raised threshold regions (indicated with the orange regions) for the existing and authorized turbines and the newly planned turbines (green regions) for PSR Saint-Hubert.

### 6.7.3 Raised threshold regions PSR Liège

In the case of PSR Liège (see Table 3.10) the number of range cells around the cell under test has been specified to be 8. In addition the 2 closest range cells, the so-called guard cells, are neglected. Given the size of a range cell of 116 m, we calculate that a wind turbine can potentially influence the radar threshold from approximately 1160 m in front until 1160 m behind the wind turbine. The size in azimuth is dependent on the horizontal beam width of the radar. Given the beam width in Table 3.10, at a range of 25 km the size in azimuth is approximately 611 m.

The region in which the wind turbine influences the threshold has been calculated for 2 combinations of wind turbines and radars:

1. The existing and authorized turbines that are closest in range from the planned wind turbines.
2. All mentioned in 1. and the seventeen newly planned wind turbines.

The results are presented in Figure 6.42 and Figure 6.43. There is no overlap between the regions of the existing and newly planned wind turbines. The affected area due to the new wind turbines is 13.12 km<sup>2</sup> for PSR Liège.



Figure 6.42 The raised threshold regions (indicated with the orange regions) for the existing and authorized turbines closest to the newly planned turbines for PSR Liège.



Figure 6.43 The raised threshold regions (indicated with the orange regions) for the existing and authorized turbines and the newly planned turbines (green regions) for PSR Liège.

In case the STAR 2000 PSR at Liège would be equipped with the Wind Farm Filter (WFF) CFAR enhanced technique, the area of raised threshold would be reduced significantly, for the existing as well as for the newly planned wind turbines. The results are presented in Figure 6.44 and Figure 6.45. The affected area due to the new wind turbines measures 3.01 km<sup>2</sup> for PSR Liège, including the WFF enhancement.



Figure 6.44 The raised threshold regions (indicated with the orange regions) for the existing and authorized turbines closest to the newly planned turbines for PSR Liège including the WFF CFAR enhancement.



Figure 6.45 The raised threshold regions (indicated with the orange regions) for the existing and authorized turbines and the newly planned turbines (green regions) for PSR Liège including the WFF CFAR enhancement.

## 6.8 Remark

The pictures in the previous section should be interpreted with care, for two reasons. Firstly, the scattering properties of the moving and the non-moving parts of the wind turbines are not being considered. With respect to the non-moving parts: since wind turbine masts are often shaped like truncated cones, wind turbine mast backscatter is not being sensed by the radar, as illustrated in Figure 6.46, given the distance to the wind farm.

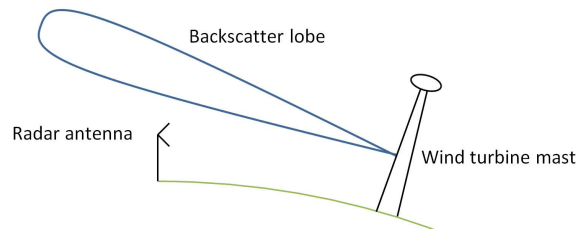


Figure 6.46 Due to the earth curvature as well as the tapering of the wind turbine mast diameter, wind turbine mast backscatter, which is confined in the backscatter lobe, may not be received by the radar.

## 6.9 False target reports and processing overload

Modern surveillance radars are equipped with multiple mechanism to obtain detections of flying targets only. To suppress reflections at non-moving objects, adaptive cluttermaps are maintained, potentially within each Doppler filter. Non-moving structures, such as the wind turbine mast and the nacelle will therefore not give rise to false (non-target) plots. A flying target will be detected if its response (echo) also passes the so-called CFAR (constant false alarm rate) circuitry. Radar manufacturers have responded to the detection of wind turbine blade flashes, by adapting the logic of the CFAR process. Rather than the CAGO (cell averaging greatest of) logic, ordered statistics (OS) logic is nowadays often applied, since this processing is better capable to detect aircraft when a wind turbine blade flash occurs. Note that the Belgium Airforce has indicated that all four involved radars are equipped with CAGO CFAR circuitry (rather than OS or like circuitry).

The Saint-Hubert radar have been equipped with a modern Next Generation Signal Processor (NGSP) receiver from Intersoft-Electronics. Therefore the radar benefits from the Vertical Clutter Canceller or VCC technology. With this technology the radar is capable of adapting the elevation antenna pattern on receive, range dependent. Thus, wind turbine backscatter can be 'nulled', which improves the detection capability of the radar above wind turbines.

The maximum rotation speed of a wind turbine is assumed to be 30 rpm. Each rotation produces six Doppler flashes, three negative and three positive, when one of the three blades is pointing up- or downwards. This results in a worst case flash frequency of 3 Hz per wind turbine. Given this blade flash frequency of 3 Hz, seventeen additional wind turbines, the azimuth beamwidth and the antenna rotation rate, 0.44 blade flashes per scan are expected from the entire windfarm for the PSR Bertem and Saint-Hubert. For the PSR at Liège, due it's slightly wider azimuth beamwidth but higher scan speed, the figure will be 0.19 blade flashes per scan. For the PSR at Zaventem, there is no line-of-sight, and can therefore not be

effected by the newly planned wind turbines. In all cases a worst case assumption, which neglects the several anti-wind turbine features of these radars described above, is that these flashes will result in PSR-only plots. Since modern surveillance radars are capable to process several hundred plots per second, the extra plots are considered as being insignificant. Processing overload is therefore not expected.

## 7 Conclusions

### 7.1 DEA primary surveillance radar Florennes

With respect to the primary radar the following aspects have been considered:

- Desensitization overhead, *i.e.*, the reduction of the detection probability of a 2 m<sup>2</sup> target at 1000, 2000, 4000, 10,000 ft AGL directly above the wind farm.
- The reduction of the maximum detection range for a 2 m<sup>2</sup> target due to shadowing effects behind the wind farm.
- Thales France, the manufacturer of the STAR 2000, offers a Wind Farm Filter (WFF) CFAR processing enhancement to the radar. The expected performance improvement when the STAR 2000 is equipped with the WFF has been discussed in this document.

#### 7.1.1 *Conclusions regarding desensitization overhead*

Using the PERSEUS model, a number of detection probability diagrams have been calculated giving the radar coverage around the airfield. The coverage diagrams have been made for four different scenarios:

- (1) the current STAR 2000 radar system without any wind turbines;
- (2) the current STAR 2000 radar system with the existing and the already authorised wind turbines;
- (3) the current STAR 2000 radar system with the existing, authorised and the newly planned wind farm.
- (4) the STAR 2000 radar system including the WFF enhancement with the existing, authorised and newly planned wind farm.

Comparing (1) and (2) we see that the performance of the STAR 2000 radar system directly overhead the wind farm will be reduced significantly by the wind turbines. In addition an area extending 2 km in front and 2 km behind the wind farm the probability of detection is significantly reduced. Comparing (2) and (3) we see that the detection capability around the newly planned wind turbines is reduced as well.

Thales France, the manufacturer of the STAR 2000, offers a Wind Farm Filter (WFF) enhancement to the radar for its STAR 2000. By comparing (3) and (4) we see the significant improvement directly overhead all wind turbines caused by the WFF enhancement. The area of reduced detection probability is now limited to directly above the wind turbine positions.

Apart from the radar's detection capability an investigation has been performed with respect to the track behaviour of the radar above the wind farm. The results show that there is a high probability that a PSR-only track will break over the wind turbines. When the WFF enhancement is present however, the probability that a track will go lost is only applicable for targets at an altitude lower than 4000 ft AGL. The system at Florennes is, however, a combined system (PSR + MSSR) and the MSSR is notably less affected by the wind farm. The radar system uses both sensors to maintain track. It is judged to be unlikely that combined and MSSR-only tracks of aircraft that travel over the wind farm will break at lower altitudes. In addition to the desensitization due to the CFAR the loss of detection is observed due to the time sidelobes as well.

### 7.1.2 *Conclusions regarding the shadowing effect*

The impact of shadowing effects behind the wind farm depends on the elevation of the surroundings. The maximum loss of detection range at 2000 ft AGL varies between 1.5 km and 4 km in a sector behind the newly planned wind turbines of windfarm at 1000 ft AGL. At higher altitudes than 2000 ft AGL, the maximum detection range is limited by the instrumented range of 60 NM (111 km) of the radar.

## 7.2 **DEA Secondary surveillance radar Florennes**

For the MSSR, there are no existing wind turbines in direct vicinity or in the same sector as the planned wind turbines. The newly planned turbines have an effect on the MSSR in the azimuth sector of  $9.4^\circ$ , from  $290.5^\circ$  to  $299.9^\circ$ . The regions where the turbines have an effect on the radar depend on target height and are displayed in Section 5.4. For the MSSR the maximum absolute off-boresight error that could occur due to the planned turbines measures  $0.29^\circ$  at an azimuth sector between  $296^\circ$  and  $297^\circ$ . This maximum error could occur at lower target height, the so-called orange area, where the boresight measurement is interfered by the mast and nacelle. At higher target height, the so-called red area, where the boresight measurement is interfered by only the blade standing in the upright position, the absolute off-boresight error equals  $0.25^\circ$ . The  $1\sigma$  standard deviation values for these two situations measures  $0.07^\circ$  for the orange area and  $0.07^\circ$  for the red area.

## 7.3 **SEA primary surveillance radars Bertem, Saint Hubert, Liège and Zaventem**

In accordance with EUROCONTROL's description of a simple engineering assessment for primary radar systems, three subjects have been analysed: line-of-sight, the volumes of the regions that are impacted, and the occurrence of false target reports.

It is concluded that the new wind turbines are not significantly obstructed by altitude level of the terrain between the radar installation and the wind turbine, with an exception for the PSR at Zaventem. There is no line-of-sight between this radar and the newly planned wind turbines. The size of the volume in which radar degradation occurs has been specified in Section 6.6 and 6.7 of the document. The newly planned wind turbines will create a volume where the PSR at Bertem can potentially be desensitised of  $8.54\text{ km}^2$  at a distance of approximately 68 km from the radar. For the PSR at Saint-Hubert the potential desensitised area measures  $9.70\text{ km}^2$  at a distance of approximately 74 km from the radar of which  $0.03\text{ km}^2$  overlaps with existing wind turbines. For the PSR at Liège the potential desensitised area measures  $13.12\text{ km}^2$  at a distance of approximately 79 km from the radar. In case the STAR 2000 PSR at Liège would be equipped with the WFF enhancement the potential desensitised area would be reduced to  $3.01\text{ km}^2$ .

Due to the cluttermap processing, it is not expected that static structures of the wind turbines will raise alarms. The probability that an alarm will be induced as a consequence of a wind turbine blade flash has been elaborated in Section 6.9. The increase of the plot rate due to this phenomenon is expected to be negligible.

#### **7.4 Changes to the wind turbine configuration**

As stated in Section 3.1 the absence of the three wind turbines at Fontenelle and the two additional wind turbines at Walcourt Florennes Gerpinnes do not have an influence on the outcomes of the studies mentioned above.

## 8 List of abbreviations

ACP	Azimuth Change Pulse
AGL	Above Ground Level
ASR	Airfield Surveillance Radar
CAGO	Cell Averaging Greatest Of
CFAR	Constant False Alarm Rate
CTR	Controlled Traffic Region
CUT	Cell Under Test
EGM96	Earth Gravitational Model 1996
MSSR	Monopulse Secondary Surveillance Radar
NASA	National Aeronautics and Space Administration
OBE	Off-sight Bearing Error
PSR	Primary Surveillance
RPM	Rounds Per Minute
SSR	Secondary Surveillance Radar
SRTM	Shuttle Radar Topography Mission
TNO	Netherlands Organisation for Applied Scientific Research
VCC	Vertical Clutter Cancellation
WC	Worst-case
WFF	Wind Farm Filter
WGS84	World Geodetic System 1984

## 9 References

- [1] EUROCONTROL guidelines on How to Assess the Potential Impact of Wind Turbines on Surveillance Sensors, Edition 1.2, September 2014, Ref. nr EUROCONTROL-GUID-0130.
- [2] Non-disclosure Agreement (NDA) between Thales France, Skeyes en TNO.
- [3] A. Theil, L.J. van Ewijk, Radar Performance Degradation due to the Presence of Wind Turbines, IEEE Radar Conference 2007.
- [4] A. Theil, M.W. Schouten, A. de Jong, Radar and Wind Turbines; A Guide to Acceptance Criteria, IEEE Radar Conference 2010.
- [5] B.M. Kent, K.C. Hill, A. Buterbaugh, G. Zelinski, R. Hawley, L. Cravens, Tri-Van, C. Vogel, T. Coveyou, Dynamic Radar Cross Section and Radar Doppler Measurements of Commercial General Electric Windmill Power Turbines Part 1: Predicted and Measured Radar Signatures, IEEE Antennas and Propagation Magazine, Vol. 50, No. 2, April 2008.
- [6] G.J. Poupart, Wind Farm Impact on Radar Aviation Interest – Final Report, QinetiQ report FES W/14/00614/00/REP, September 2003.
- [7] Signal Science Limited, [<http://www.signalscience.com/TERPEM.htm>].
- [8] Fred E. Nathanson, Radar Design Principles, JmcGraw-Hill Book Company, 1969.
- [9] Christopher C. Lin and J. Patrick Reilly, A Site-Specific Model of Radar Terrain Backscatter and Shadowing, Johns Hopkins APL Technical Digest, Volume 18, Number 3, 1997.
- [10] Recommendation ITU-R P.527-5(08/2019) Electrical characteristics of the surface of the Earth.
- [11] L. Vinagre and K. Woodbridge, “Secondary Surveillance Radar Monopulse Target Azimuth Error Estimation due to Obstacle Shadowing”, The Record of the 1999 IEEE Radar Conference, 1999.
- [12] E-mail J. Thielen from Skeyes, 9-10-2018, Locatie en hoogte radar van Florennes.